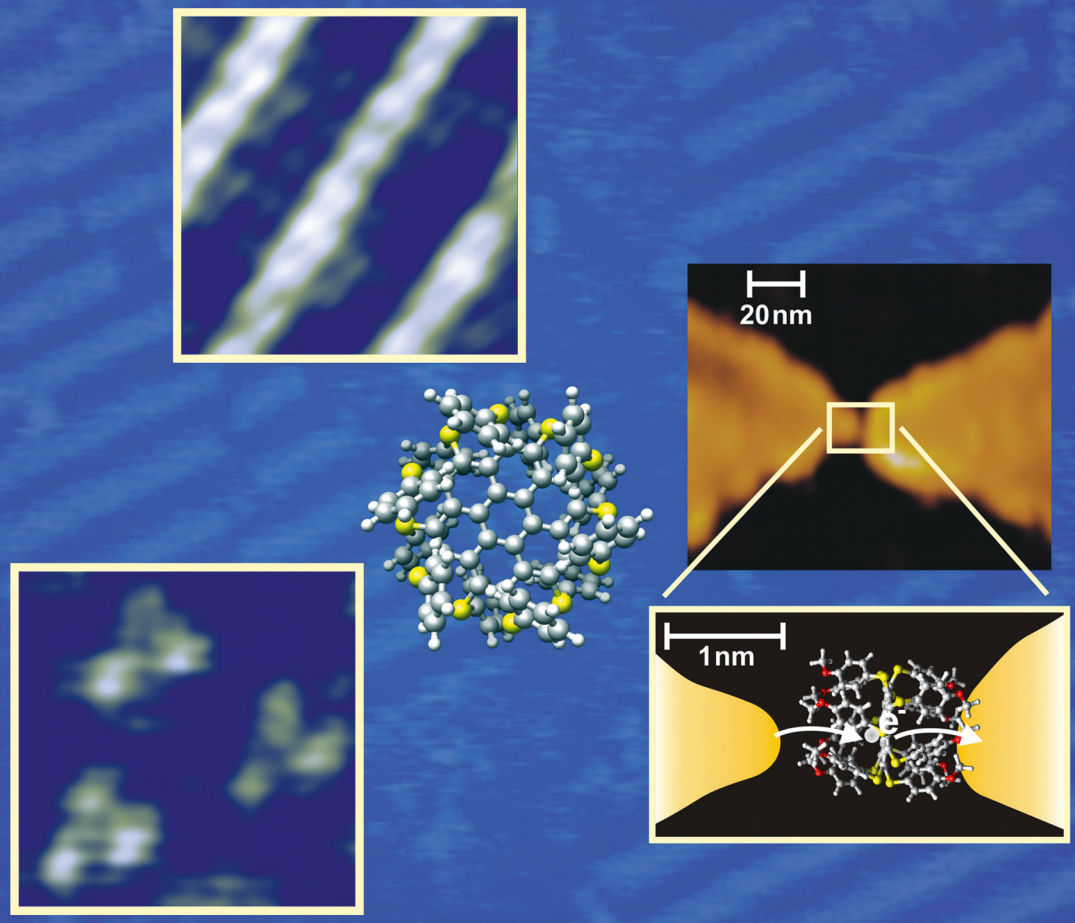

Substituted Coronenes for Molecular Electronics: From Supramolecular Structures to Single Molecules

Peter Kowalzik

Mitglied der Helmholtz-Gemeinschaft

JÜLICH
FORSCHUNGSZENTRUM

Schriften des Forschungszentrums Jülich
Reihe Information / Information Band / Volume 16

Forschungszentrum Jülich GmbH
Institute of Solid State Research (IFF)

Substituted Coronenes for Molecular Electronics: From Supramolecular Structures to Single Molecules

Peter Kowalzik

Schriften des Forschungszentrums Jülich
Reihe Information / Information Band / Volume 16

ISSN 1866-1777 ISBN 978-3-89336-679-8

Bibliographic information published by the Deutsche Nationalbibliothek.
The Deutsche Nationalbibliothek lists this publication in the Deutsche Nationalbibliografie; detailed bibliographic data are available in the Internet at http://dnb.d-nb.de.

Publisher and Distributor:	Forschungszentrum Jülich GmbH Zentralbibliothek 52425 Jülich Phone +49 (0) 24 61 61-53 68 · Fax +49 (0) 24 61 61-61 03 e-mail: zb-publikation@fz-juelich.de Internet: http://www.fz-juelich.de/zb
Cover Design:	Grafische Medien, Forschungszentrum Jülich GmbH
Printer:	Grafische Medien, Forschungszentrum Jülich GmbH
Copyright:	Forschungszentrum Jülich 2010

Schriften des Forschungszentrums Jülich
Reihe Information / Information Band / Volume 16

D 82 (Diss., RWTH Aachen University, 2010)

ISSN 1866-1777
ISBN 978-3-89336-679-8

The complete volume ist freely available on the Internet on the Jülicher Open Access Server (JUWEL) at http://www.fz-juelich.de/zb/juwel

Abstract

The ongoing miniaturization of silicon integrated circuits makes the understanding of the electronic properties of nanoscale structures and the exploration of novel materials and device concepts more and more important. One promising approach to construct future electronic systems is the usage of organic molecules and utilizing their ability to self-assemble and/or taking advantage of the possibility to achieve various electronic functions just by modifying their chemical structures.

This thesis explores a highly conjugated molecular system, namely dodecakis(arylthio)-coronenes (DATCs), with a view to potential applications as molecular electronic building blocks. The techniques of scanning tunneling microscopy and spectroscopy are applied to characterize the structural and the electronic properties of monolayers of these molecules on metal surfaces.

Variations of the substituents allowed to specifically affect the self-assembly of the molecules. Supramolecular structures with different orientations of the molecules relative to the substrate and with different intermolecular interactions are obtained. The growth of highly ordered supramolecular chains is observed in the case of the basic molecular building block dodecakis(phenylthio)coronene (Cor-H) on Au(111) surfaces. The formation of delocalized electronic states along the chains suggests the potential of this system as a basis for novel organic materials with anisotropic charge transport properties.

Substituents with varying electron-accepting or electron-donating ability are used to modify Cor-H and enhance or prevent the molecular stacking. Assemblies of molecules with molecular quantum dot behavior can also be obtained in this way. The tailored functionalization allows a decoupling of the aromatic system of the molecules from the substrate states, which in turn leads to the occurrence of single electron tunneling effects. Different substitutions of the DATC system can thus be used to create desired electronic functions.

Furthermore, several fabrication routs for nanoscale electrode structures were worked out to “wire up” single molecules in a device-like configuration and to investigate their electrical properties. In particular, the technique of electron-beam lithography in conjunction with unconventional nanofabrication methods like electromigration were utilized to fabricate nanometer-spaced metal electrodes. Such nanopatterns additionally allowed to characterize the charge transport through embedded single molecules.

Kurzfassung

Die zunehmende Miniaturisierung von Silizium-basierten integrierten Schaltkreisen lässt das Verständnis der elektronischen Eigenschaften von nanoskalierten Strukturen und die Erkundung neuartiger Materialien und Bauelement-Konzepte immer wichtiger werden. Eine mögliche Ergänzung und/oder Alternative zur heutigen CMOS-Technologie besteht in der Verwendung organischer Moleküle. Insbesondere deren Fähigkeit zur Selbstorganisation und die Möglichkeit, spezifische elektronische Funktionen allein durch Variationen der chemischen Struktur zu erreichen, machen die Molekularelektronik zu einem vielversprechenden Ansatz, zukünftige elektronische Systeme herzustellen.

Die vorliegende Arbeit befasst sich mit hochkonjugierten organischen Molekülsystemen, bezeichnet als Dodecakis(arylthio)coronene (DATC), im Hinblick auf potentielle Anwendungen als molekularelektronische Grundbausteine. Vor allem wurden hierbei die Methoden der Rastertunnelmikroskopie und -spektroskopie verwendet, um strukturelle und elektronische Eigenschaften von Monolagen dieser Moleküle auf Metall-Oberflächen zu charakterisieren.

Durch Variation der Substituenten konnte auf die Selbstassemblierung der Moleküle gezielt Einfluss genommen werden. Auf diese Weise wurden supramolekulare Strukturen mit unterschiedlichen Orientierungen der Moleküle relativ zum Substrat und mit verschiedenen intermolekularen Wechselwirkungen erzeugt. Das Wachstum von hochgeordneten Reihenstrukturen dicht gepackter Moleküle wurde im Falle des molekularen Grundbaustein Dodecakis(phenylthio)coronen auf Au(111)-Substraten gefunden. Die Ausbildung von delokalisierten elektronischen Zuständen entlang der supramolekularen Reihen zeigten das Potential dieses Systems als Grundlage für neuartige organische Materialien mit anisotropen Ladungstransport-Eigenschaften.

Die Fähigkeit zu einer molekularen Stapelung unter Ausbildung von supramolekularen Drähten konnte durch Modifikation der Substituenten zum einen verstärkt werden, und zum anderen wurde es möglich, Strukturen von Molekülen mit quantenpunktartigen Eigenschaften zu assemblieren. Verschiedene Substitutionen des DATC-Systems können somit verwendet werden, um maßgeschneiderte elektronische Funktionen zu erreichen.

Des Weiteren wurden Verfahren zur Herstellung nanoskalierter Metallstrukturen ausgearbeitet, die es ermöglichen, einzelne Moleküle in einer bauelementnahen Konfiguration zu kontaktieren und deren Ladungstransport-Eigenschaften zu untersuchen. Elektrodenpaare mit Abständen im Bereich von wenigen Nanometern wurden hierbei mit Hilfe der Elektronenstrahllithografie und spezieller Nanofabrikationsverfahren wie der Elektromigration hergestellt.

Acknowledgements

This thesis would not have been possible without the support of many other people. I would like to thank all of them.

First of all, I would like to thank Prof. Dr. Rainer Waser for giving me the opportunity to work within his institute on such a fascinating topic.

I also thank Prof. Dr. Bert Voigtländer who kindly agreed to be the co-examiner.

I am greatly indebted to my supervisor Dr. Silvia Karthäuser for her tremendous scientific as well as personal support. Her enthusiasm, her guidance and her stimulating ideas for experiments and interpretations holds a great part for the successful completion of this work.

I want to thank my office colleagues Christina Lennartz, Marcel Manheller and Dr. Lars Müller-Meskamp for the excellent working atmosphere, for their support in learning new things about the experiments and for many helpful discussions.

For the great technical support regarding the experimental set-ups and processes I want to thank Hans Haselier, Holger John, Manfred Gebauer, Hermann Bierfeld, Marcel Gerst, René Borowski, Georg Pickartz and Jochen Friedrich.

I thank Dr. André van der Hart and Dr. Stefan Trellenkanp for their assistance and the operation of the electron-beam lithography tool.

I also want to express my gratitude to Prof. Dr. Stefan Blügel, Dr. Nicolae Atodiresei and Dr. Vasile Caciuc for the fruitful collaboration, the DFT simulations and many helpful discussions and explanations.

I thank Prof. Dr. Marc Gingras and Dr. Jean-Manuel Raimundo for synthesizing and providing the molecules for the experiments.

For the experimental support by fluorescence correlation spectroscopy measurements I want to thank Dr. Habil. Silke Rathgeber.

Furthermore, I want to thank all my friends and colleagues: Dr. Adam Busiakiewicz, Lars Steffens, Alexander Soltow, Christoph Große, Rohit Soni, Tobias Menke, Roland Rosezin, Christian Nauenheim, Matthias Meier, Dr. Serge Röhrig and everyone else at the institutes for their help and support.

Finally, I want to thank my wife and my son for their patience during the last years and for giving me motivation and happiness.

Contents

1 Introduction

1.1 The miniaturization of electronic devices

The invention of the transistor at the Bell Laboratories by W. Shockley, J. Bardeen, and W. Brattain in 1947 [1] and the development of planar integrated circuits [2] were the starting points for an explosive growth of the microelectronics industry. Improvements in performance, power, and cost of semiconductor devices are the key factors which pushed the scaling of the transistor feature sizes from 10 μm to below 30 nm [3] during the past 40 years. The number of components per chip has doubled roughly every two years. This trend, known as "Moore´s Law" [4,5], is still valid and the semiconductor industry expects that feature sizes will be shrinked to below 10 nm within the next decade. At these length scales quantum effects will start to play an increasingly important role and the scaling of the complementary metal-oxide-semiconductor (CMOS) technology will inevitably slow down and finally halt, at least in the traditional sense [6].

Present day research addresses the foreseen limits of silicon integrated circuits by searching for new materials and devices that can supplement and/or potentially replace the current CMOS technology. On the one hand, nonclassical CMOS designs with new channel materials or one-dimensional structures and, on the other hand, alternatives to CMOS, based on conceptually novel approaches, are investigated. One of the latter is the emerging field of *molecular electronics*. The idea of the molecular electronic approach can be dated back to a seminal work of A. Aviram and M. A. Ratner [7], predicting that a single molecule with a donor-bridge-acceptor structure should show a rectifying behavior when placed between two electrodes. This fascinating perspective that electronic functions might be incorporated within single molecular building blocks stimulated a remarkable theoretical and experimental activity, aimed to explore molecules as potential components in electronic devices.

1.2 Molecular scale electronics

1.2.1 Concepts and prospects

Several arguments speak for the usability of the molecular approach to construct future electronic devices. Here are some of the main possible advantages:

1. *Molecules are small.* If one molecule or a small array of molecules could be used to build a transistor, it would be possible to miniaturize electronic components to a few nanometers. Greater packing densities and higher functionality are possible.

2. *Reproducibility and chemical tunability.* The chemical structure of molecules is perfectly defined and can be synthesized with high reproducibility. Silicon has a quite limited set of improvable parameters, such as doping, straining or alloying. In contrast, molecules can be synthesized with an almost endless degree of variability. Precise modifications of the electronic structure are possible and specific functionalities can be incorporated.

3. *Bottom-up fabrication.* Until now, the miniaturization of electronic devices has been achieved by the *top-down* approach using lithographic techniques to chisel out micro- and nanostructures from something bigger. The costs of the required machinery in modern production factories exceed a billion dollars. The need for patterning a transistor by means of lithographic procedures may be bypassed by an *bottom-up* fabrication approach, using the ability of molecules to self-assemble into desired nanostructures.

Besides reasons regarding potential electronic applications, molecules have some attributes which make them to an interesting object of fundamental research, aimed to understand electron transport mechanisms at the nanoscale. Miniaturized electronic structures show new phenomena that are negligible in a macroscopic conductor. In recent years, the investigations of electron transport in nanoscale objects has been one of the most active fields in condensed matter physics and also attracted huge research efforts form various other disciplines of science. Some fundamentally new effects, occurring in nanoscale conductors, are:

1. The conventional ohmic scaling property of the conductance becomes invalid when the size of the conductor gets smaller than the mean free path of the charge

carriers. The electron transport is not anymore a classical diffusive process, but electrons may move ballistically through a very small conductor.

2. The small size of both molecules and other mesoscopic systems, such as semiconducting nanostructures, may represent a confining potential for electron movement, leading to charge transport with can be restricted to two-, one- or zero-dimensions.

3. The conductor might only have a discrete set of electronic levels that may or may not be available for electrons to flow through.

4. Not appreciated before the late 1980s was the existence of a upper limit to the conductance that a ballisitic conductor with a single electronic level can exhibit. Even for the most perfect contact to the conductor, the conductance can not exceed a fundamental constant, the so-called quantum of conductance $G_0 = 2e^2/h = 77.5\,\mu\text{S}$.

5. The injection of charge into a nanoscale conductor, especially onto a molecule, can result in significant interactions with other electrons and with nuclear motions. Electronic and geometrical rearrangements may have crucial consequences for the charge transport characteristics.

1.2.2 Contacting single molecules and molecular assemblies

Providing electrical contacts to nano-sized objects like single molecules is per se a challenge. To measure the conductance of a molecule, two electrodes, the source and the drain electrode, with a nanometer-sized separation are required. Even the most advanced lithographic techniques fail to reproducibly fabricate structures with dimensions of a few nanometers. Therefore, creative experimental techniques had to be developed before molecular scale transport investigations could be performed.
The first conductance measurements down to the single molecule level were possible after the advent of scanning probe microscopy (SPM) techniques such as scanning tunneling microscopy (STM) [8–11] and conductive probe atomic force microscopy (CP-AFM) [12, 13]. In this case, molecules are deposited on top of a conducting substrate that acts as one electrode and a metallic scanning probe tip is used as the other electrode. The great benefit of such scanning probe techniques is the possibility to perform

both nanoscale topographic imaging and electrical transport measurements and thus one can actually "see" the molecules on the substrate surface before measuring their transport characteristics. In this way, electrical properties can be correlated to specific topographical features.

In the recent past a variety of unconventional nanofabrication techniques, aimed to electrically address single molecules or small arrays of molecules, have been worked out. For instance, the so-called mechanically controllable break junction technique [14–16] has been used with great success to characterize charge transport through single molecules. Here, a continuous metallic wire is either lithographically fabricated or simply glued on top of a flexible substrate that is subsequently bent to extend the wire until it breaks, so that a nanometer-sized gap can be obtained.

The nanopore technique [17] was used to measure the current through molecular assemblies having the thickness of one monolayer. In this technique, a small hole (typically 30-60 nm diameter) is fabricated in a silicon nitride membrane and molecules, deposited within this hole, are sandwiched between a top and a bottom electrode for electrical measurements.

Furthermore, combinations of nanolithographical techniques, capable to fabricate structures in the range of a few ten nanometers, and additional innovative procedures, allowing to finally obtain pairs of electrodes with separations smaller than one nanometer, were used. One of these is the electrodeposition technique [18–20]. First, two electrodes with a relatively large separation ($> 10\,\mathrm{nm}$) are fabricated on an insulating substrate by electron beam lithography (EBL). Thereafter, a metal is deposited electrochemically on these predefined electrodes, leading to a decrease of the electrode separation down to the desired molecular scale.

Contrary, the electromigration technique [21, 22] starts with a continuous metallic electrode having a predefined constriction with a width of some ten nanometers. When a high current is passed through the constriction, the electromigration of atoms will lead to a breaking of the wire. Once the wire fails, the resistance of the junction rises strongly. Therefore, the electromigration process, induced by the previously large current density, stops when a small gap has formed.

1.3 Semiconducting organic materials

Although the field of molecular-scale electronics, based on a few or single molecules, is still in its early stages, the use of organic materials as active elements in bulk or thin film devices has already entered the (opto)electronic market [23]. For expample, light-emitting diodes [24,25], photovoltaic cells [26,27], and field-effect transistors [28,29] are already commercially available. All of these applications exploit the semiconducting properties of the organic material and their performance crucially depends on the efficiency of charge transport within the organic layer(s) [30]. The existence of delocalized molecular orbitals and sufficiently strong intermolecular interactions are the basis of all organic semiconductors. Two different material classes for organic (opto)electronic devices are currently investigated. Polymers, on the one hand, are generally considered to be better suited for mass production because they can be more easily processed. Oligomers, on the other hand, allow the preparation of very well ordered films of high purity, but the processing needs much effort. Both classes have already reached the market [28,31,32]. Which class will dominate future organic electronics is not yet clear. Future technological developments and further reductions in the size of the transistor channel will bring commercially relevant devices closer to the research field of molecular electronics utilizing the properties of single (conjugated) molecules or an array of single molecules. Intermolecular charge transport is then replaced by intramolecular transport. The intermediate field of research, which may be called supramolecular electronics [33, 34], employs well-defined supramolecular architectures of organic systems on the length scale between 5 and 100 nm.

The crucial factors governing the electrical properties of both organic electronic devices using bulk organic materials or thin films and prospective molecular devices in the nanometer range are closely related to each other. The properties of the interfaces between molecular elements, supporting substrates, connecting electrodes, and the degree of molecular order are one of the key issues for the further development and miniaturization of functional devices.

1.4 Outline of the thesis

A highly conjugated molecular system with very unique chemical and physical properties is investigated within this thesis. A polycyclic aromatic core is surrounded by twelve arylthio ligands. The molecules have a pronounced non-planar geometrical structure, but conjugation is not destroyed in this way. The experiments are focused on the STM technique to characterize monolayers of these molecules on conducting substrates. The method is used to correlate the electronic characteristics of the molecular layer with the structural properties by applying combined topographical and spectroscopic measurements. The charge transport through the molecules and the self-assembly properties are investigated in dependence on the used supporting substrates and the peripheral functionalizations of the molecular system.

This thesis is organized as follows:

- Chapter 2 gives a brief introduction into the fundamentals of molecular devices, in particular into the basics of charge transport mechanisms through organic molecules and the principles of molecular self-assembly processes on solid surfaces.
- Chapter 3 describes the main experimental tool used for the characterization of the molecular electronic properties, i. e. the technique of scanning tunneling microscopy (STM) and spectroscopy (STS).
- Chapter 4 introduces the investigated molecular system, the specific properties, and the solution based deposition technique, used to prepare monolayer films of these molecules
- In chapter 5 the properties of the used substrates, namely Au(111) thin films and graphite, are briefly described. Anomalies, occurring on the surface of graphite, are investigated in some detail.
- Chapter 6 shows the experimental results of the self-assembly of the basic molecular building block dodecakis(phenylthio)coronene (Cor-H) on graphite and Au(111).
- In chapter 7 it will be shown that the degree of molecular order has a great influence on the electronic properties, determined with STS. Resonant charge transport through mainly undisturbed molecular states are compared with characteristics of densely stacked molecules.

- Chapter 8 gives a detailed analysis of the measured structural and electronic characteristics by using calculations based on the density functional theory (DFT). The simulations are carried out in collaboration with the research group *Quanten-Theorie der Materialien* at the *Institut für Festkörperforschung*, *Forschungszentrum Jülich*.
- In chapter 9 the influence of additional functional groups, attached to the Cor-H molecule, is investigated.
- Chapter 10 describes experimental investigations besides the STM/STS technique. Fabrication procedures for nanometer-spaced metal electrodes and their usability for charge transport investigations through single molecules are presented.

2 Theoretical fundamentals of molecular devices

2.1 The single molecule junction

2.1.1 A qualitative picture

The basic setup of a single molecule junction is simple, even though the experimental realization is very demanding. Two metallic electrodes are in electrical contact with a molecule and connect it in this way to the outside world (Figure 2.1(a)). An external circuit allows to apply a bias voltage V and measure the resulting current I through the metal/molecule/metal junction. An accurate theoretical description has to view the entire structure as one electronic system and include perturbations of each component due to electronic interactions. However, a qualitative picture of the possible charge transfer mechanisms is obtained by starting with each component, i. e. the metal electrodes and the molecule, respectively, and bringing these components together.
The metals, on the one hand, have a high, in general uniform density of electronic states (DOS). These states are occupied by electrons according to the Fermi distribution function

$$f(E,\mu) = \frac{1}{e^{\frac{E-\mu}{k_B T}} + 1}, \tag{2.1}$$

with μ: electrochemical potential of the left or right electrode, k_B: Boltzman constant, E: energy, T: temperature.
The molecule, on the other hand, has a discrete set of energy levels with a highest occupied (HOMO) and a lowest unoccupied molecular orbital (LUMO). Under equilibrium ($V = 0$) the electrochemical potential is uniform across the junction ($\mu_l = \mu_r$) and will usually lie somewhere inside the HOMO-LUMO gap of the molecule (Figure 2.1(b)).

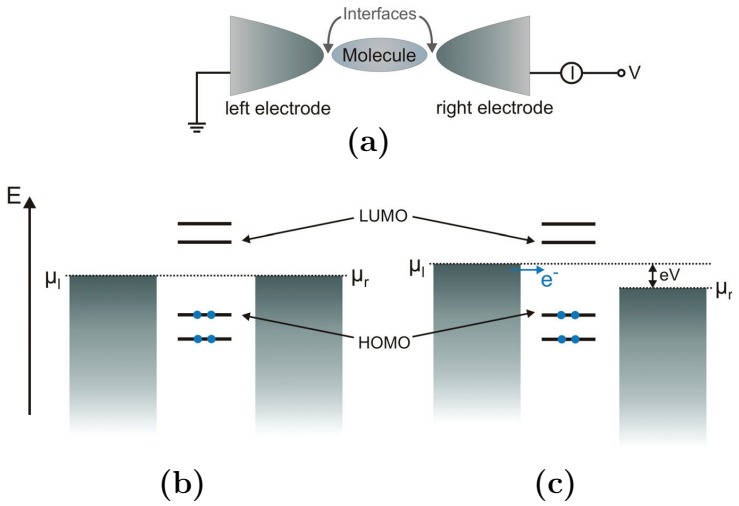

Figure 2.1: (a) Schematic illustration of a two-terminal single molecule device. (b) Sketch of the energy level diagram for $V = 0$ and (c) $V > 0$. μ_l and μ_r denote the electrochemical potentials of the left and right metallic electrode, respectively. The energy levels of the molecules are represented by discrete lines. HOMO: Highest occupied molecular orbital, LUMO: Lowest unoccupied molecular orbital.

If a voltage V is applied across the device the electrochemical potentials of the electrodes are shifted against each other by an amount $\mu_l - \mu_r = eV$ (Figure 2.1(c)). Within this bias voltage window electrons can be transmitted from the left to the right contact. The role of the molecule lying in between the electrodes is now strongly dependent on three important factors: (i) the location of the molecular states relative to the electrochemical potential of the electrodes, (ii) the shape of the molecular orbitals, and (iii) the kind and the strength of the electronic coupling of the molecule to the electrodes. All of these quantities may be tuned by synthetic molecular design. This idea is probably the main vision in molecular electronics. However, it is important to note that, besides the intrinsic properties of molecules, the nature of the electrode-molecule interface plays a significant, sometimes dominant, role for the interpretation of transport characteristics of molecular junctions [35].

2.1.2 Organic molecules and molecular orbitals

The wide degree of variability in the chemical structures of organic molecules enables to implement insulating or conducting properties and even distinct functionalities, like rectifying behaviour or bistability, may be realized [36]. The conductance of molecules is closely related to the degree of delocalized electronic states across the molecular structure. Molecular orbitals (MOs) are created by the overlap of the atomic orbitals of its constituents. This is illustrated in Figure 2.2(a) using the example of the ethene molecule (C_2H_4). A bonding σ-MO is formed when two sp^2 hybridized atomic orbitals overlap with electron density localized between two bonded nuclei. The overlap of the remaining p orbitals results in the formation of π-MOs with bonding regions located above and below a nodal plane.
Molecules with more than two adjacent p orbitals can form a conjugated system where the π electrons are shared by more than two atoms. With increasing size of such a delocalized π system the energy difference between the frontier molecular orbitals, i. e. between the HOMO and the LUMO, decreases. Both the degree of conjugation and the energies of these orbitals affect the molecular conduction properties. For instance, non-conjugated systems like alkanes show mainly insulating behaviour.
Aromatic hydrocarbons consist of a conjugated cyclic molecular structure. The most essential aromatic compound is benzene (C_6H_6). Each p orbital of the six sp^2 hybridized carbon atoms, forming a regular hexagon, overlaps equally well with both neighboring p orbitals, leading to the delocalization of π electrons over the entire ring (see Figure 2.2(b)). In Figure 2.2(c) the molecule coronene ($C_{24}H_{12}$) is depicted. It is the basic unit of the molecules studied within this thesis and belongs to the class of so-called polycyclic aromatic hydrocarbons (PAHs). They consist of fused aromatic rings, in which conjugation extends throughout the carbon skeleton.

2.1.3 Non-resonant transport

The energetic distance between the molecular states and the electrochemical potential of the electrodes (see Figure 2.1(b)) defines two basically different mechanisms of the charge transfer through the metal/molecule/metal junction. If no energy levels lie within the energy window which is spanned by the applied voltage, the molecule acts as an insulating barrier. In this case, electron transfer between the two electrodes is

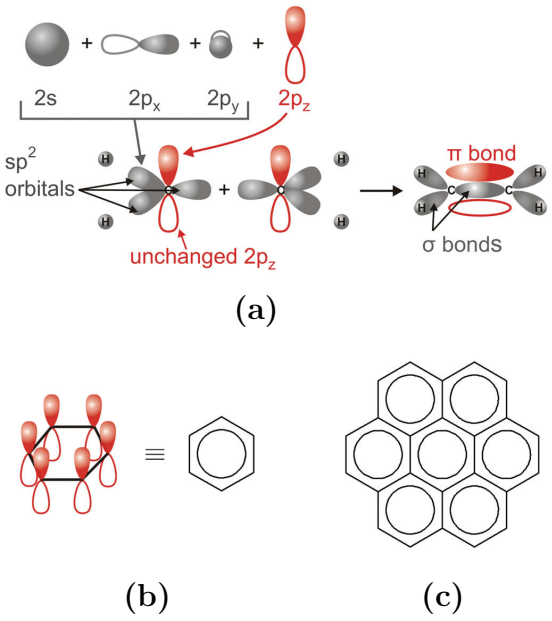

Figure 2.2: (a) Formation of sp^2 hybridized atomic orbitals of a carbon atom and a double bond in the case of the ethene molecule. (b) Schematic drawing and line notation of benzene, illustrating the six parallel p orbitals and the resulting delocalized π electron system. (c) Chemical structure of the coronene molecule.

a non-resonant tunneling process. In contrast, when molecular energy levels enter the transport window, electrons will transiently occupy these available states. Thus, the charge is transferred resonantly via the molecular states. This process may also be termed orbital mediated tunneling (OMT) [37].

The tunneling probability P_t of an electron through a classically impenetrable potential barrier has an exponential dependence on the the thickness d of this barrier

$$P_t \propto e^{-\beta d}. \tag{2.2}$$

Here, β is the characteristic decay constant of the tunnel junction and is basically dependent on the height of the barrier. The effect of a molecule sandwiched between the two metallic electrodes is to modify the potential barrier from a vacuum barrier to a barrier in which the effective barrier height is determined by the position of molecular

electronic states. In order that the non-resonant tunneling model holds, these states have to be sufficiently far away from the energy of the tunneling electrons.
A quantitative determination of the tunneling current is possible with the Simmons model [38,39], which has been very popular in the recent past to analyze experimental $I(V)$ characteristics of molecular junctions [40–42]. The Simmons model expresses the tunneling current through a barrier of height Φ_B in the regime $V < \Phi_B/e$ as

$$I = \frac{eA}{4\pi^2\hbar d^2}\left[\left(\Phi_B - \frac{eV}{2}\right)e^{-\frac{2\sqrt{2m}}{\hbar}\alpha\sqrt{\Phi_B-\frac{eV}{2}}d} - \left(\Phi_B + \frac{eV}{2}\right)e^{-\frac{2\sqrt{2m}}{\hbar}\alpha\sqrt{\Phi_B+\frac{eV}{2}}d}\right], \quad (2.3)$$

where m is the electron mass, A is the area over which current flows, and α is a unitless correction parameter that accounts for deviations from the original rectangular barrier model or for an effective mass of the tunneling electrons [43,44]. Equation (2.3) can be linearized for voltages $V << \Phi_B$:

$$I = VCe^{-\beta d}, \quad (2.4)$$

where the constant factor C and the decay parameter β are given by

$$C = \frac{\sqrt{2m\Phi_B}e^2\alpha A}{h^2 d},\ \beta = \frac{2\sqrt{2m\Phi_B}\alpha}{\hbar}. \quad (2.5)$$

The predicted exponential dependence of the tunneling resistance on the length of the molecular bridge has been observed in a number of experiments, especially in the case of alkanethiol-based molecules [45]. Here, decay constants in the range of $\beta = (10.0 \pm 1.5)\,\mathrm{nm}^{-1}$ and apparent barrier heights of $\Phi_B = (1.4 \pm 0.2)\,\mathrm{eV}$ were observed. In the case of a vacuum gap between two metals, the barrier height is determined by the metal work functions of typically 5 eV. The molecule therefore serves to lower the effective barrier height and thus enhances tunneling compared to the vacuum case.

2.1.4 Resonant transport

Elementary transport equations

In order to determine the $I(V)$ characteristics of a metal/molecule/metal junction in the resonant transport regime, it is useful to consider a single molecular level with an

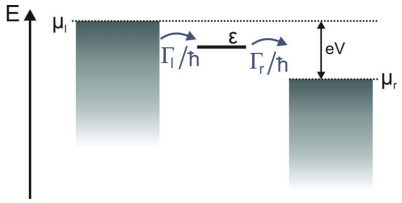

Figure 2.3: Resonant tunneling through a single molecular energy level with energy ϵ. $\Gamma_l/\hbar$ and $\Gamma_r/\hbar$ denote the rates at which electrons are injected into the level and escape from the level, respectively.

energy ϵ lying in between the electrochemical potentials of the two metal electrodes, as schematically depicted in Figure 2.3. If a positive voltage V is applied, then the left electrode injects electrons into the molecular level, while the right electrode pulls electrons out. The in- and out-flow of electrons can be described by a rate equation [46, 47]. The current flowing across the left junction is given by

$$I_l = \frac{e\Gamma_l}{\hbar}(f(\epsilon, \mu_l) - N) \tag{2.6}$$

and the current across the right junction by

$$I_r = \frac{e\Gamma_r}{\hbar}(N - f(\epsilon, \mu_r)). \tag{2.7}$$

The quantities $\Gamma_l/\hbar$ and $\Gamma_r/\hbar$ are the rates at which electrons are injected into the level and escape from the level, respectively. $\Gamma_{l,r}$ are termed coupling parameters. N denotes the actual number of electrons on the molecular level. Under steady state, the currents across the two junctions will be equal ($I_l = I_r$), giving an steady state occupation $N = \frac{\Gamma_l f(\epsilon,\mu_l)+\Gamma_r f(\epsilon,\mu_r)}{\Gamma_l+\Gamma_r}$. By substitution into Equation (2.6) or (2.7) one obtains the steady state current to be

$$I = \frac{e}{\hbar}\frac{\Gamma_l\Gamma_r}{\Gamma_l + \Gamma_r}\left[f(\epsilon, \mu_l) - f(\epsilon, \mu_r)\right]. \tag{2.8}$$

The strength of the coupling between the molecule and the electrodes determines the extend to which an initially discrete molecular level is spread in energy. In order to account for this, the discrete level ϵ has to be replaced by a density of states (DOS) function $D_\epsilon(E)$ whose integral over energy is equal to one. The electron transport

through molecules having more energy levels contributing to the current can be included within this model under the assumption that all levels conduct independently. Then the single-level DOS has to be replaced by the total DOS $D(E) = \sum_n D_{\epsilon_n}(E)$, where ϵ_n is the energy of the nth molecular level. The current I is obtained by an integral over energy:

$$I = \frac{e}{\hbar} \int_{-\infty}^{+\infty} \mathrm{d}E \, D(E) \frac{\Gamma_l \Gamma_r}{\Gamma_l + \Gamma_r} \left[f(E, \mu_l) - f(E, \mu_r) \right]. \tag{2.9}$$

The analysis of Equation (2.9) can be simplified by taking the zero-temperature limit, which is an appropriate approximation even for measurements at room temperature because the thermal energy $k_B T \sim 25\,\mathrm{meV}$ is usually much smaller than the applied bias voltage and the energy level broadening by the contacts. With $f(E, \mu_{l,r}) = 1$ for $E \leq \mu_{l,r}$ and $f(E, \mu_{l,r}) = 0$ for $E > \mu_{l,r}$ at $T = 0\,\mathrm{K}$, one can write

$$I = \frac{e}{\hbar} \int_{0}^{eV} \mathrm{d}E \, D(E) \frac{\Gamma_l \Gamma_r}{\Gamma_l + \Gamma_r}, \tag{2.10}$$

where the energy E is measured with respect to the electrochemical potential μ_r of the right contact.

Single electron effects

The charge transfer in the resonant transport regime is governed by two important aspects. The first is certainly the discrete quantum mechanical energy spectrum of a molecule. Secondly, an electron which is injected into the molecule will have strong Coulomb interactions with other electrons. In other words, the capacitance of a molecule is so small that a considerable charging energy has to be paid by an electron to hop onto the molecule.

Dependent on the relative magnitude of the molecule-electrode coupling $\Gamma = \Gamma_l + \Gamma_r$ and the single electron charging energy E_C, two different transport regimes are possible. If the coupling is weak ($\Gamma << E_C$), one can observe a sequential tunneling of integer charges to or from the molecule. In contrast, the electron number on the molecule is not anymore a well-defined observable when the coupling is strong ($\Gamma >> E_C$). In this case, the molecular energy levels are broadened significantly and moreover a mixing of molecular and metal states may occur. Much of the original electronic signal characteristic for the isolated molecule is lost in this way.

The weak coupling regime can be represented by a double-barrier tunnel junction, i. e. both electrodes are coupled resistively and capacitively to the molecule by a tunneling barrier. An approximate description for the energetics of the charge transport is the so-called *constant-interaction (CI) model* [48, 49]. This model is based on the assumption that Coulomb interactions of an electron on the molecule with all other electrons, in and outside the molecule, can be parametrized by a constant capacitance C. When N electrons reside on the molecule, its total energy is $E_{tot}(N) = \sum_{i=1}^{N} \epsilon_i + (Ne)^2/2C$. Here, the ϵ_i are the energies of the orbitals that can be occupied by electrons provided their total number does not change and the term $(Ne)^2/2C$ is the total electrostatic energy of the molecule with N electrons. The electrochemical potential μ_N, i. e. the minimum energy required to add the N-th electron to the molecule, is then given by

$$\mu_N = E_{tot}(N) - E_{tot}(N-1) = \epsilon_N + \left(N - \frac{1}{2}\right)\frac{e^2}{C}. \tag{2.11}$$

The resonant charge transport in the weak coupling regime can be described by a sequential tunneling process where an electron tunnels from the left electrode onto the molecule and subsequently off from it to the other electrode. Tunneling via the LUMO occurs when the molecule alternates between its anion state ($N+1$ electrons) and its neutral state (N electrons), i. e. μ_{N+1} enters the energetic window between the electrochemical potentials μ_l and μ_r of the left and right contact, respectively. Accordingly, tunneling via the HOMO takes place when μ_N lies in this window. The electrochemical potentials μ_N and μ_{N+1} are related to the ionization potential (IP) and the electron affinity (EA), respectively, defined as:

$$IP = -\mu_N = E_{tot}(N-1) - E_{tot}(N), \tag{2.12}$$

$$EA = -\mu_{N+1} = E_{tot}(N) - E_{tot}(N+1). \tag{2.13}$$

The difference between IP and EA is therefore

$$IP - EA = E_{tot}(N+1) - 2E_{tot}(N) + E_{tot}(N-1) = \frac{e^2}{C} + \epsilon_{N+1} - \epsilon_N. \tag{2.14}$$

One can see that the $(N+1)$-th electron needs to have an energy larger than the N-th electron by $e^2/C + \epsilon_{N+1} - \epsilon_N$. This term, commonly called the *charge additon energy*, consists of two contributions. The first term $e^2/C \equiv E_C$ is the charging energy,

required to overcome the Coulomb repulsion among different electrons. The second term $\epsilon_{N+1} - \epsilon_N$ is the result of the quantized electronic level structure of the molecule and is equal to the HOMO-LUMO gap of the neutral molecule in the ground state.

2.2 Semiconductivity in organic solids and thin films

In contrast to devices based on single molecules, bulk or thin film structures of organic molecules with semiconducting behaviour are already extensively applied in commercial opto(electronic) products, as outlined in the introductory chapter. The origin of semiconducting properties in organic compounds is commonly related to the existence of extended bonding (π) and anti-bonding (π^*) molecular orbitals. Intermolecular interactions in a solid consisting of molecules with delocalized π and π^* orbitals, lead to a splitting of these molecular energy levels, resulting in the formation of narrow bands. The existence of such bands is the basis of electrical conduction in organic solids and the origin of their semiconducting properties. In the case of organic materials, sophisticated molecular designs allow to specifically tune decisive characteristics such as charge carrier mobilities and energy gaps between the filled π states (valence band) and the π^* states (conduction band).
The crucial factors determining the formation of energy bands in organic materials can be seen by considering the simple example of a dimer made of two ethene molecules in a cofacial configuration, as illustrated in Figure 2.4 [30, 50]. The HOMO of the isolated ethene molecule is the bonding combination of the two $2p_z$ atomic orbitals where the lobes of the same sign interact, whereas the LUMO is the anti-bonding combination where lobes of opposite sign interact. In the cofacial dimer having an intermolecular distance of 0.4 nm, the interaction leads to a splitting of these molecular levels. The HOMO splits into two states separated by a quite large value of 0.539 eV, whereas the LUMO splitting is much smaller, 0.148 eV. This is due to the fact that the interaction between the molecular HOMO functions is either fully bonding or fully anti-bonding. The resulting HOMO-1 and HOMO level of the dimer are therefore considerably stabilized and destabilized, respectively. In contrast, direct bonding interactions of the molecular LUMO functions are compensated for by diagonal antibonding interactions

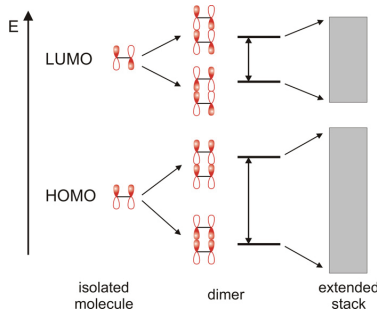

Figure 2.4: Sketch of the intermolecular interactions between the HOMO and LUMO in a dimer of two ethene molecules. Also indicated is the formation of the valence and conduction bands when a large number of molecules are stacked together [30].

or direct antibonding interactions are compensated for by diagonal bonding interactions, resulting in a smaller LUMO splitting in the dimer. In general, bonding and anti-bonding interactions are very sensitive to the relative positions of the interacting units. The magnitude of the splitting and the width of the associated energy bands therefore essentially depends on the specific packing of the molecules within the solid. One of the key parameters for charge transport in molecular crystals is the intermolecular transfer integral expressing the strength of the electronic coupling of the molecular orbitals between the adjacent molecules. This quantity also determines the dispersion relation of the crystal. Using the tight-binding model including nearest-neighbor interactions, one can write the eigenvalues of the crystal Hamiltonian $\hat{H}$ as [51–53]

$$E(\mathbf{k}) = \epsilon_0 + \sum_j t_j e^{i\mathbf{k}\cdot(\mathbf{R}_i - \mathbf{R}_j)}, \tag{2.15}$$

where ϵ_0 is the energy of the monomer state including energetic shifts due to the aggregation within the crystal and $\mathbf{k}$ is the reciprocal lattice vector. The summation only extends over lattice sites $\mathbf{R}_j$ being nearest-neighbors to the i-th molecule of the lattice. The transfer integrals t_j are defined as

$$t_j = \left\langle \Psi_j \left| \hat{H} \right| \Psi_i \right\rangle, \tag{2.16}$$

where Ψ_i is the wave function of the i-th molecule and Ψ_j the wave function of the molecule located at the neighboring lattice site $\mathbf{R}_j$.

In organic semiconductors generally two important types of packing motives featuring $\pi - \pi$ overlap are observed: a layered herringbone (also called edge-to-face) packing, characteristic for example in the case of oligoacenes like pentacene, and the π-stack (also called face-to-face) motif, characteristic for discotic molecules based on polycyclic aromatic hydrocarbons (PAHs). In both cases, the anisotropic intermolecular electronic overlap results in a very anisotropic charge transport, being mostly two-dimensional (2D) in oligoacene single crystals and one-dimensional (1D) in π-stacks of discotic PAHs. In the latter case, the intermolecular transfer integral along the stacking direction ($t_{||}$) is much larger than between the stacks, so that the dispersion relation can be approximated by the 1D relation [54, 55]

$$E(k) = \epsilon_0 + 2t_{||}cos(ka), \tag{2.17}$$

where a is the lattice constant in the stacking direction. The bandwidth of such a 1D stack is given by $BW = |E(\pi/a) - E(0)| = 4\left|t_{||}\right|$. Generally, a broader band leads to a lower effective mass, which, in turn, leads to a higher mobility and a higher conductivity. However, a band-like regime of charge transport similar to that of inorganic semiconductors is only applicable to single crystals of organic materials and highly organized thin films at sufficient low temperatures. For increasing temperature and/or disordered organic semiconductors, the charge transport gets dominated by a thermally activated hopping mechanism between localized polaronic states [50, 56]. The upper limit for the charge carrier mobility in organic thin-film field-effect transistors at room temperature was predicted to lie in the range of $10\,\mathrm{cm^2V^{-1}s^{-1}}$ [57] due to the weak intermolecular forces existing among nearest-neighbor molecules, so that the vibrational energy of the molecules at room temperature reaches a magnitude close to that of the intermolecular bonding.

2.3 Self-assembly of molecules on solid surfaces

The expression *molecular self-assembly* has been defined in [58] as the "spontaneous association of molecules under equilibrium conditions into stable, structurally well-defined aggregates joined by noncovalent bonds". The key issue for the self-assembly of molecules at solid surfaces is the subtle interplay between molecule-molecule and

molecule-substrate interactions as illustrated in Figure 2.5. The characteristic energies which are decisive for the formation of two-dimensional supramolecular structures are the adsorption energy, the energy barriers for diffusion and rotational motions, and the intermolecular interaction energy due to noncovalent bonds [59, 60]. Basic molecule-molecule interaction types to be considered are van der Waals (vdW), electrostatic, dipole-dipole, π–π interactions, and hydrogen bonds. The adsorption of molecules on the surface can be classified into two types: physisorption and chemisorption. The physisorption of molecules is characterized by mainly unperturbated electronic structures of the adsorbates and of the substrate surface. In contrast, chemisorption originates from the formation of strong covalent bonds between molecules and substrate atoms and thus involves a modification of their electronic structures. The physisorption is characterized by low binding energies of a few 100 meV and equilibrium adsorbate-surface separations in the order of about 0.3–1 nm, whereas chemisorption results in binding energies in the range of some eV and distances of 0.1–0.3 nm between the covalently bonded atoms of the molecule and the substrate surface [61]. When molecules chemisorb onto the surface, the diffusion barriers usually become very large. Investigations in the recent past have shown that the self-assembly process of chemisorbed molecules can be influenced by the fact that the molecule and an attached substrate atom form a new entity, which then can diffuse as one unit across the surface [59, 62–64]. Alkanethiols on Au(111), the archetypical system of self-assembled monolayers (SAMs) [65], involve a covalent sulphur-gold bond. For this example several indications suggest that the self-assembly is promoted by diffusing molecule-substrate atom entities [62, 66, 67].

Hooks *et al.* [68] described the equilibrium structure formed by a particular system with the energetic balance of the interaction energy E_{mm} between molecules in the adsorbate layer and an adsorbate-substrate interface energy E_{ms}. This balance is more precisely described in terms of the relative magnitudes of the corresponding elastic constants, c_{mm} and c_{ms}, being the second derivatives, $\mathrm{d}^2E/\mathrm{d}x^2$, at the potential energy minima of E_{mm} and E_{ms}, respectively, as illustrated in Figure 2.5(b). By comparing these energies, different regimes of the structure formation can be assigned. If the molecule-substrate interactions are very strong and the potential well of E_{ms} is highly curved ($c_{mm} < c_{ms}$), a commensurate adlayer structure can be formed. Contrary, incommensurate films are observed if $c_{mm} \gg c_{ms}$ because the energetic benefit of moving the molecules to preferred substrate sites cannot balance the perturbation of the molecule-molecule distances away from the native energetic minimum of the intermolecular potential. On

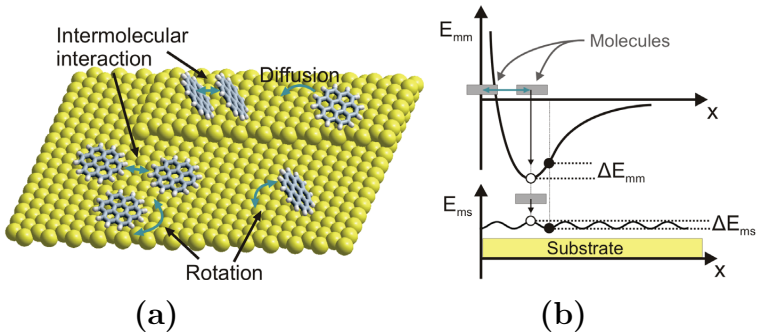

Figure 2.5: Illustration of the mechanisms controlling the self-assembly process of molecules on a solid surface. (a) The formation of self-assembled structures is the result of a balanced interplay between intermolecular interactions due to noncovalent bonds, molecule-substrate interactions, and the associated energy barriers for diffusion and rotational motions of the molecules. (b) The potential energy functions of the intermolecular interactions (E_{mm}) within the adsorbate layer and the molecule-substrate interactions (E_{ms}) determines the equilibrium molecular arrangement and the position of the molecules relative to the substrate lattice [68]. The minimization of the global energy is the driving force in all self-assembly processes.

the other hand, a coincident match may be achieved without the need of a strong modification of the native adsorbate structure. If a precise coincident configuration is not achieved and $c_{mm} \approx c_{ms}$, the native molecular distances may be adjusted slightly to achieve coincidence with a supercell containing a few primitive cells.

Because only the translational coordinates of the molecules were included, the above mentioned energetic considerations apply to point like objects and thus can only provide one aspect of the different structural regimes for the two-dimensional self-assembly of more complex molecules. An accurate description additionally has to take into account the mutual spatial orientation of the molecules with respect to the substrate surface and with respect to each other. In order to maximize intermolecular interactions, the molecules can furthermore perform conformational rearrangements and geometrical distortions like bond stretches or angle bends. The structure formation for systems of large organic molecules is therefore also governed by a delicate balance between the energies associated with the orientational and conformational degrees of freedom.

3 Scanning tunneling microscopy and spectroscopy

3.1 The working principle

The invention of the scanning tunneling microscope (STM) by Gerd Binnig and Heinrich Rohrer in the early 1980s [8, 9, 69] opened the way to investigate surface phenomena in real space on a truly atomic scale. The working principle of the STM is the very localized nature of probing a surface by utilizing the quantum mechanical tunneling effect. An atomically sharp metallic tip is approached towards a conductive substrate and kept in front of the surface at a very small distance of typically 0.5-1 nm (Figure 3.1). When a voltage is applied between the tip and the substrate, a tunneling current through the classically impenetrable barrier is induced which has an exponential dependence on the distance between the two electrodes. A variation in the tip-sample distance of only 0.1 nm leads to a change of the tunneling current by one order of magnitude. This dependency provides the possibility to control the distance between the tip and the surface with very high sensitivity and allows to obtain atomic resolution.
An image of the surface is generated by performing a raster scan over the surface. In the *constant current* mode of operation, an electronic feedback loop maintains a preset value of the tunneling current by controlling the z position of the tip relative to the surface. Piezoelectric elements are used to perform the fine motion required to generate data points with sub Ångström separation. A computer control system records the vertical position during scanning and plots the values as a function of the lateral position. The changes in tip height with position under feedback control reflect both the tip-sample separation and the spatial variation of the local density of states (LDOS) of the surface. Therefore, the STM constant current image only reflects true height changes if the LDOS

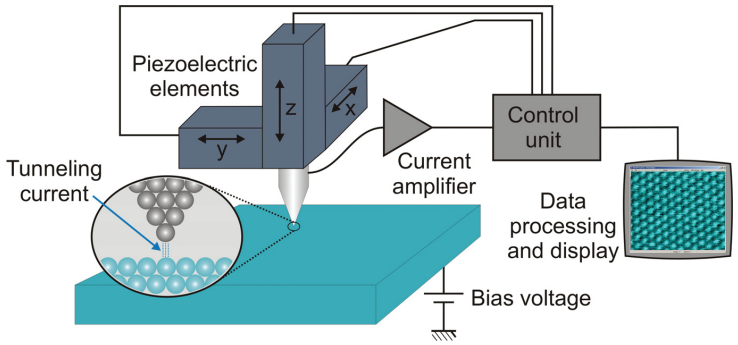

Figure 3.1: Schematic diagram illustrating the operation of a scanning tunneling microscope. A metallic tip is scanned across a conducting substrate in x- and y-direction. The strong dependence of the tunneling current on the distance between the tip and the substrate surface is used to probe the topography of the sample.

is constant across the scanned area. This is true for atomic steps of metal surfaces, but will for example not be the case for molecular adsorbates. A second mode of STM operation is the *constant height* mode. In this case the absolute vertical position of the tip remains constant during scanning and the value of the tunneling current is plottet as a function of the lateral tip position. Because the tip can easily touch protruding sites of the surface during scanning at constant height, this mode is only applicable for atomically flat surfaces.

3.2 Theoretical description

A theoretical basis for a general treatment of the tunneling process in a STM was developed by Bardeed and is known as the transfer Hamiltonian approach [70]. The total tunneling current I between two independent electrodes can be calculated for a weak wave function overlap by a summation of the contributions of all states involved in the tunneling:

$$\begin{aligned} I &= \frac{2\pi e}{\hbar} \sum_{m,n} |M_{mn}|^2 \, \delta\left(E_m - (E_n + eV)\right) \\ &\quad \times \left[f(E_m, \mu_t)\left[1 - f(E_n, \mu_s)\right] - f(E_n, \mu_s)\left[1 - f(E_m, \mu_t)\right] \right]. \end{aligned} \tag{3.1}$$

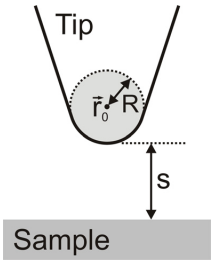

Figure 3.2: Schematic drawing of the tunneling geometry [71]. The tip is assumed to be locally spherical with a radius of curvature R.

Here, V is the sample bias voltage, $f(E, \mu_{t,s})$ is the Fermi distribution function (see Equation (2.1)) and M_{mn} is the tunneling matrix element between the states m and n of tip and sample having the energies E_m and E_n with respect to the electrochemical potentials μ_t and μ_s. The δ-Function accounts for an elastic tunneling process. M_{mn} quantifies the overlap of the wave functions Ψ_m and Ψ_n of tip and sample states in the tunneling gap and can be written as a surface integral over a surface separating the two electrodes:

$$M_{mn} = \frac{-\hbar^2}{2m} \int \mathrm{d}S \ (\Psi_m^* \nabla \Psi_n - \Psi_n \nabla \Psi_m^*) \,. \tag{3.2}$$

This approach was first applied by Tersoff and Hamann [71,72] to calculate the tunneling current in a STM configuration. They simplified the calculation of the matrix element by restricting the tip to a spherical shape with only s-type wavefunctions contributing to the tunneling process (Figure 3.2). Within the limits of zero temperature and small bias voltages, Tersoff and Hamann found the expression

$$I \propto V \cdot \rho_t(E_F) e^{2\kappa R} \sum_n |\Psi_n(\vec{r_0})|^2 \, \delta(E_n - E_F), \tag{3.3}$$

where $\kappa = \sqrt{2m\Phi_{eff}}/\hbar$ is the inverse decay length with Φ_{eff} being the effective local barrier height, $\rho_t(E_F)$ is the density of states of the tip at the Fermi level $E_F = \mu_t = \mu_s$ for $V = 0$, $\vec{r_0}$ is the center of curvature of the tip, and R is the effective tip radius. The sum $\sum_n |\Psi_n(\vec{r_0})|^2 \, \delta(E_n - E_F)$ represents the local density of states (LDOS) of the sample $\rho_s(E_F, \vec{r_0})$ at the Fermi energy measured at the position $\vec{r_0}$. For scanning at constant current and small voltage, the STM images a constant LDOS contour of the sample around E_F.

A generalization of the results of Tersoff and Hamann for higher values of the bias voltage is obtained by including all states m and n with energies E between the elec-

trochemical potentials μ_t and μ_s, i. e. the tunneling current can be expressed by the integral [73, 74]:

$$I \propto \int_0^{eV} \mathrm{d}E\, \rho_t(E - eV)\rho_s(E, \vec{r_0}), \tag{3.4}$$

where the electrochemical potential of the substrate is taken as a reference energy ($\mu_s = 0$). This equation can also be written in the form

$$I \propto \int_0^{eV} \mathrm{d}E\, \rho_t(E - eV)\rho_s(E)T(E, V, z), \tag{3.5}$$

where the LDOS of the sample measured at the center of curvature of the tip has been approximated by the product of the density of states at the sample surface and a transmission coefficient $T(E, V, z)$. Using the simplified model of a rectangular shape for the barrier, $T(E, V, z)$ is given by

$$T(E, V, z) = exp\left[-2z\sqrt{\frac{2m}{\hbar^2}\left(\overline{\Phi} + \frac{eV}{2} - E\right)}\right], \tag{3.6}$$

where $\overline{\Phi} = (\Phi_s + \Phi_t)/2$ is the average of sample and tip work functions and z is the tip-sample separation ($z = s + R$). The quantities of Equations (3.5) and (3.6) are illustrated in Figures 3.2 and 3.3.

The evaluation of the energy dependence of the density of electronic states at the sample surface is of particular interest within this work. For this purpose, scanning tunneling spectroscopy (STS) measurements are performed where the tunneling current is measured while a voltage ramp at a fixed tip-sample separation is applied. As will be shown in the following, one can numerically extract the sample DOS features form the measured $I(V)$ curves.

Stroscio *et al.* [75] suggested to use the normalized differential conductance $(\mathrm{d}I/\mathrm{d}V)/(I/V)$ for the extraction of the DOS. The properties of this quantity can be seen in its analytical expression. In a first step, the derivative of Equation (3.5), i. e. the differential conductance $\mathrm{d}I/\mathrm{d}V$, is calculated:

$$\frac{\mathrm{d}I}{\mathrm{d}V} \propto e\rho_s(eV)T(eV, V, z) + \int_0^{eV} \mathrm{d}E\, \rho_s(E)\frac{\delta T(E, V, z)}{\delta V}. \tag{3.7}$$

Here, it was assumed that the tip density of states is featureless. This assumption is

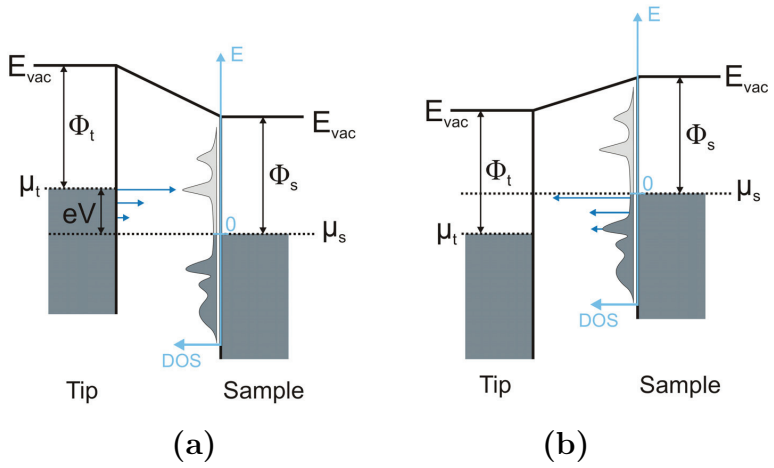

Figure 3.3: (a) Energy diagram for the tunneling process at positive bias voltage V. Electrons tunnel from the tip into empty states of the sample in the energy range between μ_s and $\mu_t = \mu_s + eV$. (b) Tunneling process for $V < 0$. Electrons tunnel from occupied states of the sample towards the tip. The arrows symbolize the tunneling direction of electrons. The contribution of tunneling electrons at different energies to the overall current is schematically indicated by the length of the arrows.

justified because the STM tip is usually a metal, but it has to be proved in each experiment since the electronic structure of the tip apex may deviate significantly from the bulk properties of the metal. The derivative of the tunneling current highlights the features of the sample density of states, but it also diverges exponentially both in separation z and in voltage V, and therefore relevant DOS features may be masked. These divergences can be eliminated by normalizing the derivative to the total conductance of the tunnel junction, i. e. one computes the ratio of differential to total conductance, called normalized differential conductance (ndc):

$$\frac{\mathrm{d}I/\mathrm{d}V}{I/V} = \frac{\rho_s(eV) + \frac{1}{e}\int_0^{eV} \mathrm{d}E \, \frac{\rho_s(E)}{T(eV,V,z)} \frac{\delta T(E,V,z)}{\delta V}}{\frac{1}{eV}\int_0^{eV} \mathrm{d}E \, \rho_s(E) \frac{T(E,V,z)}{T(eV,V,z)}}. \tag{3.8}$$

Because the transmission coefficients $T(E,V,z)$ and $T(eV,V,z)$ appear as ratios in the numerator and denominator of this equation, their exponetial dependence on z and V tend to cancel [76, 77]. This property of the ndc allows to directly compare STS measurements taken at different tip-sample separations and was the original motivation

for its use as the quantity resembling the DOS of the sample. The method of the ndc became a common tool for the analysis of STS results and it was also shown to be appropriate for the interpretation of STS measurements of organic adsorbate layers [78, 79]. On the other hand, a recent analysis of Wagner *et al.* [80] gave a differentiated view onto the usability of the ndc for the evaluation of tunneling spectra of organic molecules. Here, it was pointed out that the cancellation of the exponential backgrounds in the ndc is accompanied by unwanted shifts in the energetic positions and relative heights of DOS features. Thus, there are obvious contrary views on the applicability of the ndc for the extraction of the DOS of organic adsorbates. In the following chapter, some model calculations are aimed to get a better understanding of the DOS evaluation from STS $I(V)$ measurements.

3.3 Model calculations of tunneling spectra

To illustrate the evaluation of STS measurements, a model sample DOS $\rho_s(E)$ is created, which exhibits the general properties of real molecule-surface systems, namely separated and broadened resonances. The model DOS consists of two Gaussian peaks having a standard deviation of 0.1 eV and centered around +1 eV and −1 eV, respectively, superimposed on a constant background DOS of 1/ eV (Figure 3.4(a)). The $I(V)$ curve is then calculated using Equations (3.5) and (3.6). The DOS $\rho_t(E)$ of the tip is again assumed to be constant and thus merged with the proportionality prefactor. The work functions of the tip and the sample are set to a reasonable value of $\Phi_t = \Phi_s = 5\,\mathrm{eV}$. To discuss the DOS recovery in dependence on the tip-sample separtation z, the current is calculated for three different values of z (Figure 3.4(b)). Figures 3.4(c) and (d) show the differential conductance $\mathrm{d}I/\mathrm{d}V$ and the ndc $(\mathrm{d}I/\mathrm{d}V)/(I/V)$, respectively, which were calculated from the $I(V)$ curves of Figure 3.4(b). As expected from the discussion in Chapter 3.2 (Equations (3.7) and (3.8)), the strong dependence on the tip-sample separation in the differential conductance is canceled out in the ndc due to the normalization to the total conductance. For this example, the peak positions of the model DOS are already assignable in the $\mathrm{d}I/\mathrm{d}V$ plots but for larger tip-sample separations get more and more masked. Thus, very small DOS features on a larger background may not be observable anymore. The masking of less pronounced features is reduced in the ndc curves. The peak positions in the ndc are in quite good agreement with the

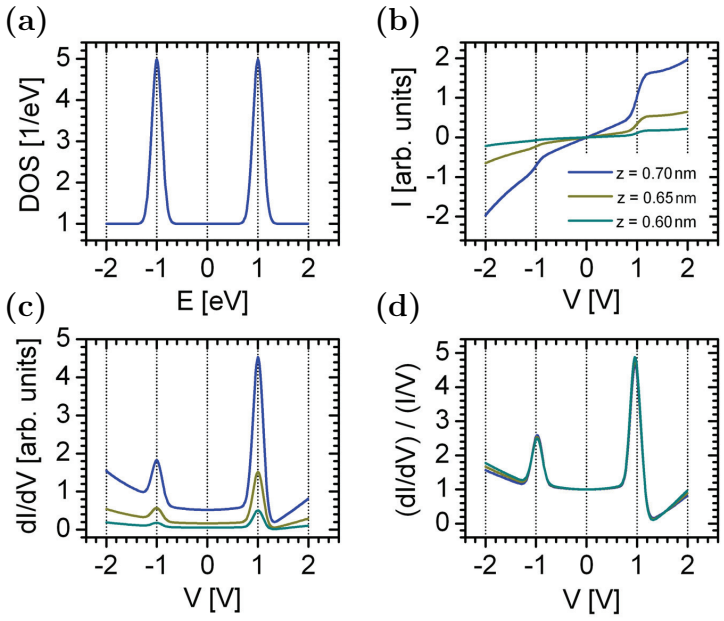

Figure 3.4: Model calculations illustrating the extraction of the sample DOS from STS $I(V)$ measurements. (a) Input DOS used for the calculations. (b) $I(V)$ curves for three different values of the tip-sample separation z, calculated with Equations (3.5) and 3.6. (c) Differential conductance $\mathrm{d}I/\mathrm{d}V$ and (d) normalized differential conductance $(\mathrm{d}I/\mathrm{d}V)/(I/V)$ versus voltage curves, obtained from the corresponding $I(V)$ characteristics in (b).

input DOS, but the partially very high slope of the normalization function (I/V) leads to small shifts ($< 50\,\mathrm{meV}$ in this example) in the direction of lower energetic differences to $E = 0$. It is also important to note that the occupied states appear with decreased intensities when compared to the unoccupied states. Whereas the model DOS is symmetric with respect to $E = 0$, the ndc produces a significant height difference between the peaks at negative and positive bias voltage. The reason for these differences becomes obvious when comparing the energetic situation of the tunneling electrons for the two polarities of the bias voltage (see Figure 3.3). For $V > 0$ (the empty states of the sample are probed), the maximum transmission occurs for electrons with an energy $E = eV$, while for $V < 0$ (the filled states of the sample are probed), the maximum transmission occurs at $E = 0$. The contribution of electrons tunneling at $V > 0$ into pronounced

features of the sample DOS is thus very significant, whereas electrons tunneling from maxima of the sample DOS for $V < 0$ contribute with a reduced weighting to the total current. This asymmetry in the contribution of tunneling electrons at different energies to the overall current is the origin of the intensity differences of the ndc peaks.

Based on these considerations, one can conclude that the ndc is a useful quantity to recover relevant features of the sample DOS. On the other hand, one has to be careful when interpreting the relative magnitude of different DOS features because their absolute values are strongly influenced by a specific weighting which depends on the polarity of the bias voltage, on its magnitude, and on the particular shape of the DOS. Furthermore, the normalization can cause shifts of the peak positions, the magnitude of which is varying for different specific $I(V)$ characteristics [80].

3.4 Experimental details

The STM and STS measurements of this thesis were performed under ultra-high vacuum (UHV) conditions with a JEOL 4500S STM head. The UHV system and the mechanisms for the sample and tip transfer were home-built at our institute during the PhD and diploma works of Lars Müller-Meskamp and Maria Christina Lennartz, respectively [81, 82]. The system consists of three UHV chambers, two for sample/tip exchange, storage and heating, and the other containing the STM scanner (Figure 3.5). Two chambers are equipped with ion getter pumps and the measurement chamber additionally with a titanium sublimation pump (TSP) providing a pressure of $\leq 1 \times 10^{-10}$ mbar during measurements. Isolation from mechanical vibrations is achieved by a Gimbal Piston type suspension system of the STM head and pneumatic feet lifting the whole vacuum chambers. A load lock chamber equipped with a turbomolecular pump is used to insert tips and samples into the UHV system. The sample stage of the STM head is connected to a cryostat mounted on top of the measurement chamber. The cryostat is a double-walled dewar vessel with liquid nitrogen shielding. The bottom part is occupied by a liquid helium tank. During the period of experiments of this thesis no practicable facility was available to transport liquid helium containers into the STM laboratory located in the basement of the institute. However, experiments could be carried out by cooling with liquid nitrogen, allowing a temperature of about 80 K at the sample position. The used STM tips were homemade by electrochemical etching of

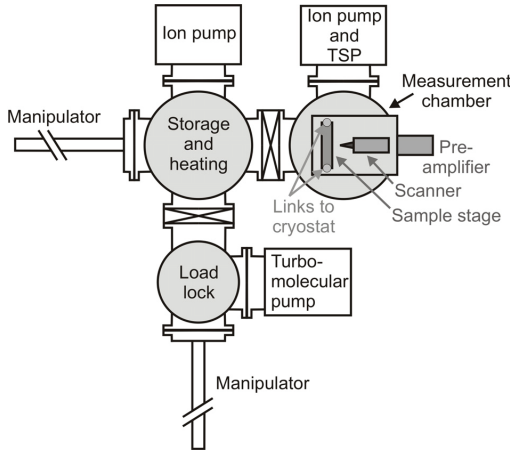

Figure 3.5: Schematic drawing of the UHV-STM system, showing the layout of the different chambers, the pumping system, and the manipulators for sample and tip exchange.

tungsten wires in a NaOH/KOH-solution and using a nanosecond-switch-off controller. Details of the tip preparation can be found in [83]. Prior to STM measurements, the tips are heated by a filament in the UHV storage chamber to remove adsorbates.

The STM topographic images shown in this thesis are obtained in constant current mode. The applied voltage and the reference current used during image acquisition are denoted as V_{sp} and I_{sp}. Positive bias voltages mean that electrons tunnel from the tip into unoccupied states of the sample.
STS measurements are conducted by measuring $I(V)$ curves for a fixed tip-sample distance, determined by the values of the voltage setpoint V_{sp} and the current setpoint I_{sp}. After the tip-sample distance has been adjusted according to the setpoint parameters, the feedback loop is switched off and a $I(V)$ curve is recorded. The $I(V)$ data are obtained either at a designated point of a topographic image or in the current imaging tunneling spectroscopy (CITS) mode. In the latter case, I(V) curves are recorded at each point of the topographic constant current STM image.
The ndc $(\mathrm{d}I/\mathrm{d}V)/(I/V)$ is calculated numerically from the measured $I(V)$ curves. The calculation of the ndc is problematic if the $I(V)$ characteristic shows a region of almost zero conductance around $V = 0$. To avoid artificial features in the ndc due to singularities, a offset method, introduced by Prietsch *et al.* [84], was used. The denominator I/V is replaced by $\sqrt{(I/V)^2 + c^2}$, where c is a small constant. This modification is negligible when $I/V \gg c$. On the one hand, the value of c has to be chosen large enough to avoid an amplification of the noise signal in the low conductance region and,

on the other hand, sufficiently small to maintain the normalization property of the denominator.
The STM/STS data shown in this thesis were analyzed with three different software tools, namely WinSPM DPS Version 2.00 from Jeol Ltd., SPIP Version 5.0.1.0 from Image Metrology, and WSxM 4.0 Develop 10.1 from Nanotec Electronica S.L.

4 Investigated organic compounds

4.1 Arylthio-substituted coronenes

The investigated dodecakis(arylthio)coronenes (DATCs) belong to the class of organic molecules consisting of a polycyclic aromatic core (see section 2.1.2), which is per-substituted with arylthio ligands. The functionalization of the aromatic core with arylthio groups leads to several unique chemical and physical properties (redox potential, UV/Vis absorption, conductivity, liquid crystallinity, etc.) [85]. The characteristic features have been ascribed to the aromaticity of the rings with sp^2 hybridized carbon atoms and the electronic contribution from numerous divalent sulfur ligands. For instance, spectroelectrochemisty studies of DATC molecules indicated that an electronic delocalization over the whole molecule exists in its anionic or dianionic forms [86]. Cyclic voltammetry measurements revealed furthermore that DATCs show two reversible one electron reduction steps and the stabilization by the arlythio substituents was estimated to about 1 V for each reduction, compared to coronene itself [87]. X-ray crystallographic studies of persulfurated arenes showed that these compounds exhibit a conformational preference in the solid state for an up and down alternation of the substituents above and below the plane of the central arene unit, in a pattern and sequence that depends on the aromatic core and the specific functionalization [85]. For example, the smaller analogue to the molecules studied in this thesis, having benzene instead of coronene as central aromatic core, i. e. hexakis(phenylthio)benzene, exhibits an up and down alternating pattern of the phenylthio groups in the solid state [88]. In summary, the findings suggest that such molecular systems can be seen as nanomolecules with a three-dimensional electronic network, in which an effective delocalization of charges throughout the molecules exists.
In this thesis DATC molecules with three different functionalizations are investigated.

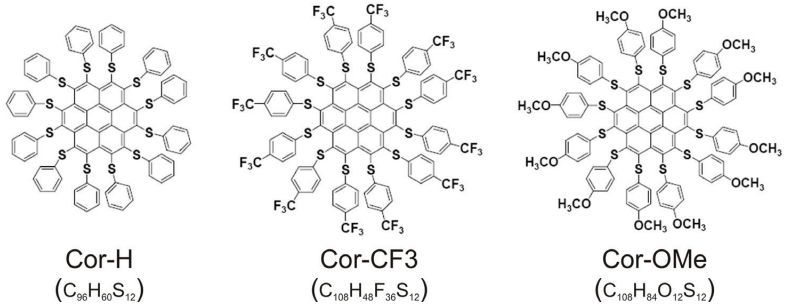

Figure 4.1: Chemical structures of the investigated organic compounds and their acronyms used in this thesis.

Figure 4.1 shows the chemical structure of these compounds. Dodecakis(phenylthio)-coronene (Cor-H) is the basic building block. The other derivatives have additional substituents in para-position at the peripheral phenyl groups. Dodecakis[p-(trifluoro-methyl)phenylthio]coronene (Cor-CF3) possesses electron-withdrawing CF_3 groups and dodecakis(p-methoxyphenylthio)coronene (Cor-OMe) electron-donating OCH_3 groups. All molecules were synthesized in the group of Prof. Marc Gingras at the University of Nice-Sophia Antipolis (France). The preparation is based on the nucleophilic aromatic substitution of dodecachlorocoronene with thiolate anions of the desired substituents. Details of this procedure can be found in [87] and [85].

4.2 Deposition of molecules

Monolayer films of the investigated DATC molecules are obtained by deposition from solution. The used drop casting technique [89–91] is schematically depicted in Figure 4.2. A drop of a DATC solution is applied onto the substrate surface. The solvent evaporates and leaves a layer of molecules on the surface. The rate of solvent evaporation can be controlled by using solvents with different vapour pressures. Additionally, the solvent evaporation can be slowed down by storing the solution covered substrate in a sealed atmosphere saturated by the vapour of the solvent. This is done by placing the sample and a beaker of solvent under a bigger beaker. The average thickness of the resulting molecular layer is dependent on the concentration of the solution. In this

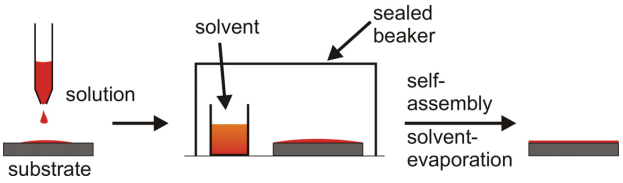

Figure 4.2: Scheme of the drop casting technique.

thesis, films in the range of one monolayer are investigated. The required concentrations of the corresponding solutions are estimated by assuming that each molecule covers a surface area of $A_m = 2\,\text{nm} \times 2\,\text{nm}$ within the monolayer. The concentration is then calculated from

$$c = \left(\frac{A_s/A_m}{N_A} \right) / V_d, \tag{4.1}$$

where A_s is the surface area of the substrate covered with solution, N_A is the Avogadro number and V_d is the volume of the applied droplet. The required mass of DATC molecules in a solution of volume V is calculated according to $m = cVM$, where M is the molecualr weight of the molecules (Cor-H: 1598.2836 g/mol, Cor-CF3: 2414.2592 g/mol, Cor-OMe: 1958.5954 g/mol). The used substrates have a size of $3\,\text{mm} \times 7\,\text{mm}$. A complete coverage of the substrates is obtained by using a droplet of volume $V_d = 7\,\mu\text{l}$. Toluene, dimethylformamide, and 1,2,4-trichlorobenzene, having vapour pressures of 29 hPa, 3.8 hPa, and 1.3 hPa at $20°C$, respectively, are used as solvents. The period of the solvent evaporation can be varied from approximately one minute to more than 12 hours. The former is achieved by using toluene as solvent and leaving the sample in air during evaporation, and the latter by using 1,2,4-trichlorobenzene and storing the sample in a sealed atmosphere of the solvent during the whole period of the evaporation. All deposition experiments were performed at room temperature. Specific procedures and parameters, tested for a particular molecule/substrate system, will be given in the corresponding chapters of this thesis.

5 Substrates

Two substrates are used for the deposition of molecules: (i) Au(111) and (ii) graphite. The fabrication of (111)-oriented gold thin films is well-established at our institute and was successfully utilized to prepare highly ordered thiol-based SAMs [92–96]. Section 5.1 will give a short overview of the the main characteristics of this substrate. A more detailed description will be given for the graphite substrate. On the one hand, the ease of preparation and the chemical inertness of the graphite surface made it a very commonly used substrate for the deposition of chemical and biological species [97–99]. However, there are a number of unusual properties of graphite surfaces [100–104], the understanding of which is still not complete. For the interpretation of STM/STS data of deposited molecules it is of paramount importance to be aware of the structural and electronic properties as well as of the anomalies of the graphite surface. Section 5.2 introduces some of these unique features of graphite.

5.1 Gold thin film substrates

(111)-oriented gold thin films are fabricated by electron beam evaporation of gold on mica. Gold can be grown on mica in an epitaxial fashion [105]. The used muscovite form of mica basically consists of aluminium silicate sheets and can easily be cleaved along the (001)-plane. The cleaved surface provides a clean and atomically flat surface. The arrangement of surface oxygen atoms of the SiO_4-tetraeders promotes an epitaxial (111)-oriented growth of gold [106].
The gold thin films are evaporated on mica by using a two step deposition process. The method was originally proposed by Höpfner *et al.* [106] and was specifically optimized at our institute [82, 107, 108]. The samples are manufactured according to the following steps. Immediately before insertion into the vacuum chamber of the electron beam

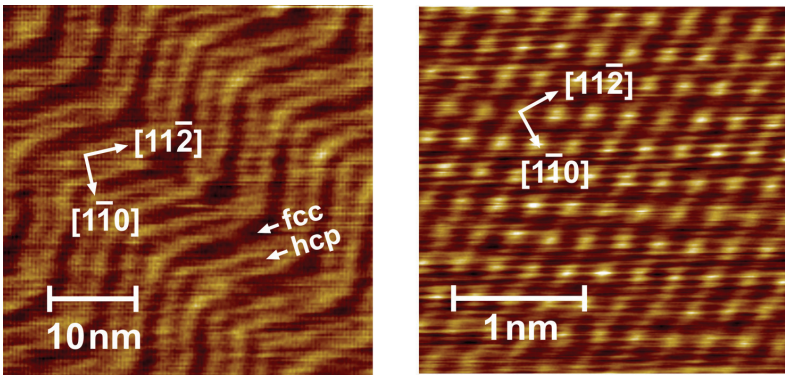

Figure 5.1: STM imgages showing the (111) surface of gold. (a) Herringbone reconstruction of the surface. (b) Atomically resolved image of the Au(111) surface.

evaporation system the mica samples[1] are freshly cleaved to prepare a clean and flat surface. In order to remove residual gases and moisture, the samples are heated in vacuum ($< 1 \cdot 10^{-7}$ mbar) at a temperature of 640 K for about five hours. The gold film is deposited at the same substrate temperature after reaching a pressure of $\sim 5 \times 10^{-8}$ mbar. First, a 150 nm thick layer is deposited with a high evaporation rate of 5 nm/s to achieve a continuous gold film. Immediately afterwards 50 nm are deposited at a very low rate of 0.05 nm/s. Remaining holes and rough surface features of the first deposition step are leveled out during this second step and during the subsequent annealing at deposition temperature for 1.5 hours. Finally, the samples are slowly cooled down to room temperature during 2.5 hours. The procedure yields (111)-oriented gold surfaces which are dominated by atomically flat terraces of triangular shape with monoatomic steps along the $[0\bar{1}1]$, $[\bar{1}10]$ and $[01\bar{1}]$ directions.

The close packed (111) surface of gold exhibits the so-called herringbone reconstruction (Figure 5.1(a)) arising from a contraction of the interatomic distance in the topmost surface layer along the $[1\bar{1}0]$ direction [109–111]. This is due to the fact that 23 gold atoms of the surface layer are arranged over 22 bulk atoms in this direction resulting in a $(23 \times \sqrt{3})$ rectangular overlayer structure. Domains with hexagonal close packed (hcp) and face centered cubic (fcc) stacking are alternating within the overlayer unit cell.

[1] Ultra-clean muscovite mica samples were purchased from Plano GmbH, Wetzlar (Germany).

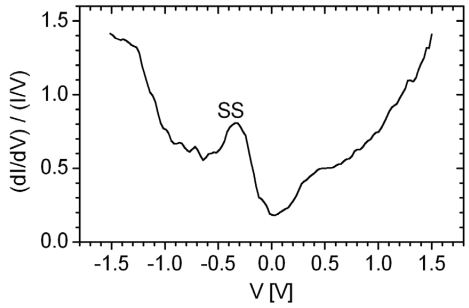

Figure 5.2: Tunneling spectrum of the Au(111) surface. The shown ndc curve was obtained numerically from an average of 50 individual $I(V)$ curves ($V_{sp} = 1.0\,\mathrm{V}$, $I_{sp} = 0.2\,\mathrm{nA}$) obtained within a surface area of $2\,\mathrm{nm} \times 2\,\mathrm{nm}$.

The transition between fcc and hcp domains results in about 0.02 nm high domain walls formed by surface atoms near bridge sites. These lines are running along the $[11\bar{2}]$ direction and rotated periodically by 120°, forming the characteristic herringbone pattern. The surface reconstruction leads to a periodic structure of inequivalent adsorption sites for atoms and molecules. This was observed to affect the pattern formation in several cases, as demonstrated by preferred nucleation at the elbows and commensurabilities with the herringbone structure [112–116].

Characteristic for the density of electronic states of the clean Au(111) surface is a Shockley-type surface state (SS) having a band onset at $\sim 0.4\,\mathrm{eV}$ below the Fermi level [117–119]. Figure 5.2 shows a normalized differential conductance versus voltage curve measured on the Au(111) surface. The peak observed at a voltage of about $-0.35\,\mathrm{V}$ is due to the surface state. The increase in the density of states beginning near $-1\,\mathrm{V}$ can be attributed to the $L_{2'}$ band edge of gold [118].

5.2 Graphite

5.2.1 Basic properties

Lattice structure

Graphite, next to diamond the second crystalline modification of carbon, consists of stacked layers (basal planes) of sp^2 hybridized carbon atoms. The carbon atoms within each layer sit on the corners of hexagons and are covalently bonded to three nearest neighbors with a bond length of 0.142 nm (Figure 5.3(a)). The unhybridized $2p_z$ orbitals of the carbon atoms, oriented perpendicular to the plane, give rise to a delocalized π-system.

The weak interlayer bonding in graphite is due to van der Waals interactions and the small overlap of the π-orbitals between atoms of adjacent layers. The anisotropic layered structure of graphite is reflected in its macroscopic material properties like elasticity, thermal and electrical conductivity. The latter has a value of $1 \times 10^4\,\Omega^{-1}\mathrm{cm}^{-1}$ along the layers, which is four magnitudes higher than in the perpendicular direction [120].

In natural graphite two stacking types of basal planes are observed, leading to the existence of a rhombohedral and a hexagonal lattice structure. While the stacking in rhombohedral graphite has an ABC sequence, the hexagonal form (Figure 5.3) is stacked in AB fashion. In the latter case, one half of the atoms (α-atoms) of each layer is positioned above an atom and the other half (β-atoms) above the hexagon centres of the adjacent layer. The hexagonal lattice vectors $\mathbf{a}_1$ and $\mathbf{a}_2$ within the plane have an absolute value of 0.246 nm. The lattice constant in perpendicular direction is $c = 0.67\,\mathrm{nm}$.

Within this work, synthetic highly oriented pyrolytic graphite (HOPG) is used. HOPG consists of crystallites with hexagonal lattice structure. The size of these crystallites is in the range of some micrometers within the layer plane and of some ten nanometers along the vertical direction [121]. The crystallites are aligned along the c-axis. The full width at half maximum of the angle distribution between the c-axes of different crystallites, called mosaic spread, defines the quality of the crystal and is specified to $(0.4 \pm 0.1)^\circ$ for the used substrates[2]. Within the plane no specific orientation exists

[2]HOPG substrates were purchased from Plano GmbH, Wetzlar (Germany).

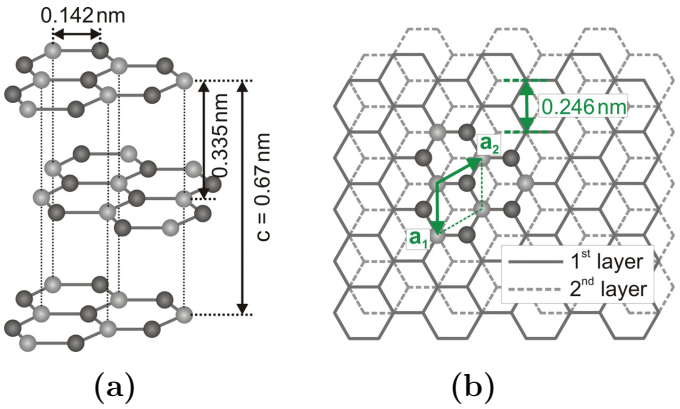

Figure 5.3: Lattice structure of hexagonal graphite. (a) Schematic drawing of the three-dimensional arrangement of carbon atoms. The interatomic distance within the basal planes is 0.142 nm and the layer separation is 0.335 nm. Light and dark balls represent the differently coordinated α- and β-atoms, respectively. (b) Top view onto the basal plane and the surface unit cell. The continuous grey lines depict the surface layer and the dotted grey lines the second layer underneath.

between the crystallites, so that the stacking at the crystallite boundaries can deviate from the ABAB sequence.

For the deposition of organic molecules and their characterization by STM, graphite has some very useful properties. Due to the weak interlayer interactions compared to the binding of atoms within the layers, it is easy to separate the layers from each other. By stripping some layers with an adhesive tape, one obtains a clean surface with atomically flat, monocrystalline terraces which extend over some square micrometers. Furthermore, the graphite surface is chemically inert to a large extent. The physisorption of organic molecules on graphite provides the opportunity to investigate molecular properties with minimal perturbation by the substrate [122, 123].

STM image contrast and electronic structure

Figure 5.4(a) shows an experimental STM image ($V_{sp} = 0.5\,\mathrm{V}, I_{sp} = 0.25\,\mathrm{nA}$) of the graphite surface. Instead of the actual atomic arrangement at the surface, the STM image shows maxima only at every second carbon atom. The origin of this phenomenon

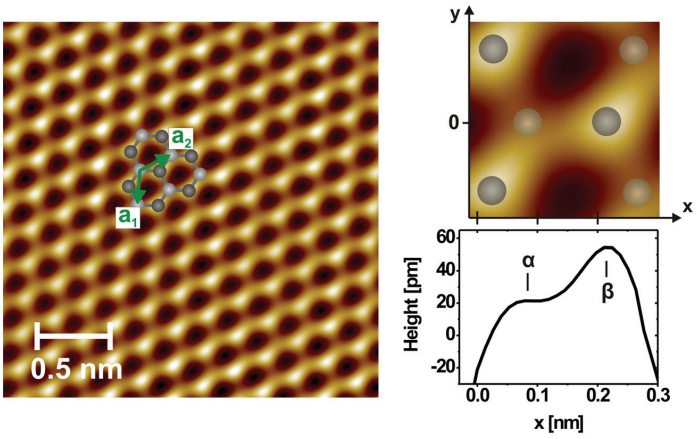

Figure 5.4: (a) STM image ($V_{sp} = 0.5\,\mathrm{V}, I_{sp} = 0.25\,\mathrm{nA}$) of the graphite surface. The zoom-in in (b) highlights the apparent height difference corresponding to different local densities of states for α- and β-atoms. Positions of α- and β-atoms are marked with light grey and dark grey balls, respectively. The line profile shows the apparent height along the x-direction for $y = 0$.

is due to the electronic dissimilarity of carbon atoms on the graphite surface which have atoms directly below them (α-atoms) and those who are located above the hexagon centres (β-atoms). The electronic density of states near the Fermi level E_F is reduced at the α-sites due to the π-orbital overlap with atoms directly below. Since the STM is sensitive to the LDOS near E_F for low bias voltages, the β-atoms give a greater contribution to the image (see Figure 5.4(b)).

In Figure 5.5 a tunneling spectroscopy measurement for the pure graphite surface is shown. Features characteristic for the graphite surface are observed at about 0.7 eV below and 0.8 eV above the Fermi level. They can be attributed to states of the bonding π and antibonding π^*-bands located around the K points of the graphite Brillouin zone [124–126].

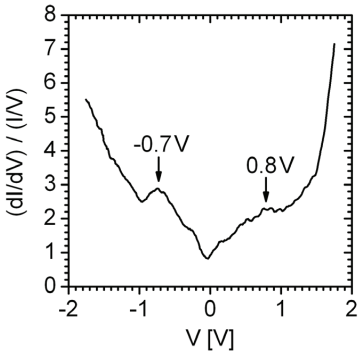

Figure 5.5: Tunneling spectrum recorded on pure graphite. The ndc curve was obtained numerically from an average of 50 individual $I(V)$ curves ($V_{sp} = 1.0\,\mathrm{V}$, $I_{sp} = 0.3\,\mathrm{nA}$) within a surface area of $1\,\mathrm{nm} \times 1\,\mathrm{nm}$.

5.2.2 Superlattice phenomena

At the graphite surface a variety of defects can occur which might be formed during crystal growth or cleavage [100]. Examples are distorted cleavage steps, ridges, graphite fibres, folded-over flakes, or small carbon particles. The most puzzling phenomenon of the graphite surface during the last two decades was the occurrence of superperiodic hexagonal structures on top of the graphite atomic lattice [101, 127, 128]. It is widely believed that most of the observed superlattice structures are the result of a Moiré rotation pattern, arising from the misorientation between surface graphite layers [101, 129–131], but details of such superlattices are not yet well understood. The Moiré superlattice has the same symmetry as the original hexagonal graphite atomic lattice and its periodicity P is dependent upon the misorientation angle θ of the topmost surface layer with respect to the graphite crystal underneath:

$$P = \frac{a}{2sin\,(\theta/2)}, \tag{5.1}$$

where $a = 0.246\,\mathrm{nm}$ is the lattice constant of the graphite surface. The orientation of the Moiré pattern with respect to the atomic orientation of the top layer is given by

$$\phi = 30^\circ - \theta/2. \tag{5.2}$$

The observation of Moiré superlattices shows the capability of the STM technique to image also the nature of internal defects which are below the surface. However, superlattices can be a potential problem for imaging deposited species on graphite, particularly if the deposited molecules form periodic structures on the graphite surface. In order to distinguish the presence of deposited molecules from the apparent modification in the atomic corrugation of graphite, it is important to understand the relationship between superlattice pattern and interlayer interactions. During the experiments of this thesis, in particular after deposition of the investigated DATC molecules, a variety of superlattices were observed. Several of these structures showed periodicities in the range of the molecular dimensions. Therefore, it was necessary to figure out whether the molecules assemble into hexagonal structures on graphite or a Moiré effect is responsible for the observations. In short, non of the observed hexagonal structures could definitely be ascribed to a molecular structure, but they were consistent with Moiré rotation patterns of graphite. Figure 5.6(a) shows an example of a superperiodic hexagonal structure with a periodicity of $P = 1.92\,\mathrm{nm}$. The superlattice extends over an area of more than $200\,\mathrm{nm} \times 200\,\mathrm{nm}$. In the magnified and Fourier filtered image of this structure (Figure 5.6(b)) the superlattice and the atomic lattice of the graphite surface are simultaneously visible. By using the two-dimensional Fourier transform (Figure 5.6(c)) of this image, an accurate determination of the lattice parameters and the orientation between two lattices is possible. A value of $\phi = 26.33°$ is obtained. The application of Equations (5.1) and (5.2) shows that this structure can be assigned to a Moiré rotation pattern where the top layer has a misorientation angle $\theta = 7.34°$. The explanation of the superstructure with a Moiré rotation is further evidenced by its three-fold symmetry like the graphite atomic lattice. The line profile in Figure 5.6(d) shows areas of three different apparent heights, which are denoted as M-α-sites, M-β-sites, and M-h-sites, respectively. Xhie *et al.* [129] suggested an explanation based on the assumption that an atom in the top rotated layer above a hole site in the second layer would show maximum intensity in the STM images, just like β-atoms of the graphite surface with normal stacking. An atom above an α-atom in the second layer would show a lower intensity and an atom above a β-atom would show the minimum intensity. Figure 5.7 shows a schematic drawing based on a superposition of three layers. The surface layer is rotated by $\theta = 7.34°$ with respect to two normally stacked bulk graphite layers. The resulting local density of states at the surface is encoded in the colour of the superimposed atoms. The three different sites of the STM image (Figure 5.6(b) and (d)) can be identified.

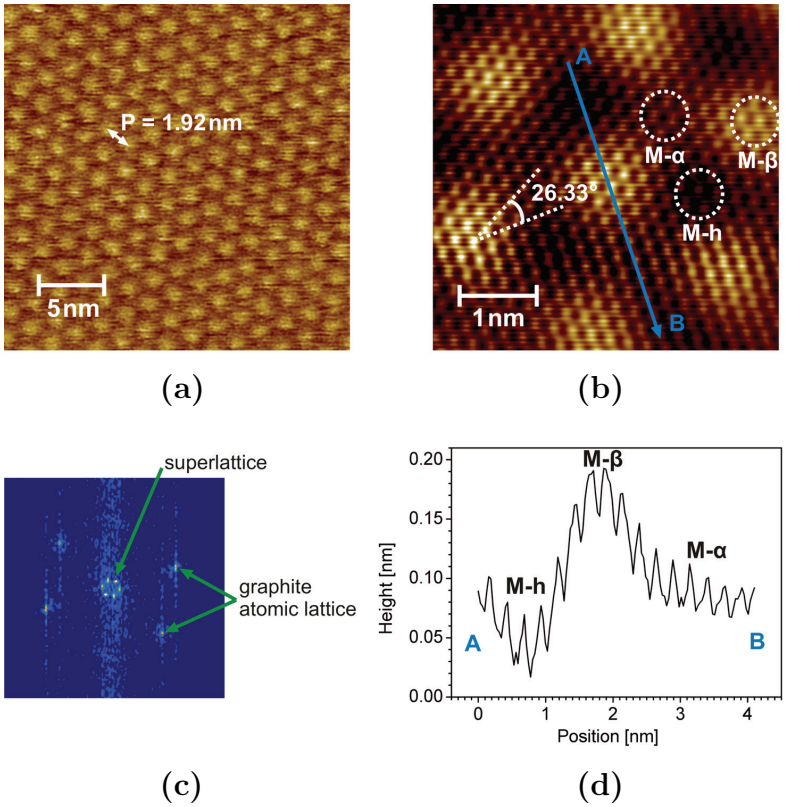

Figure 5.6: Example of a superlattice observed on graphite. (a) STM image showing the hexagonal symmetry of the superlattice with a periodicity of $P = 1.92\,\text{nm}$. The magnified and Fourier filtered image in (b) and the two-dimensional Fourier transform in (c) show the simultaneous imaging of the superlattice and the graphite atomic lattice. The orientation of the superlattice with respect to the atomic lattice is $\phi = 26.33°$. The superlattice has a three-fold symmetry. Areas with three different apparent heights are observed: M-β-sites are the brightes, M-α-sites the second brightes, and M-h-sites the darkest in the STM image. (d) Line profile along the AB line of the image in (b).

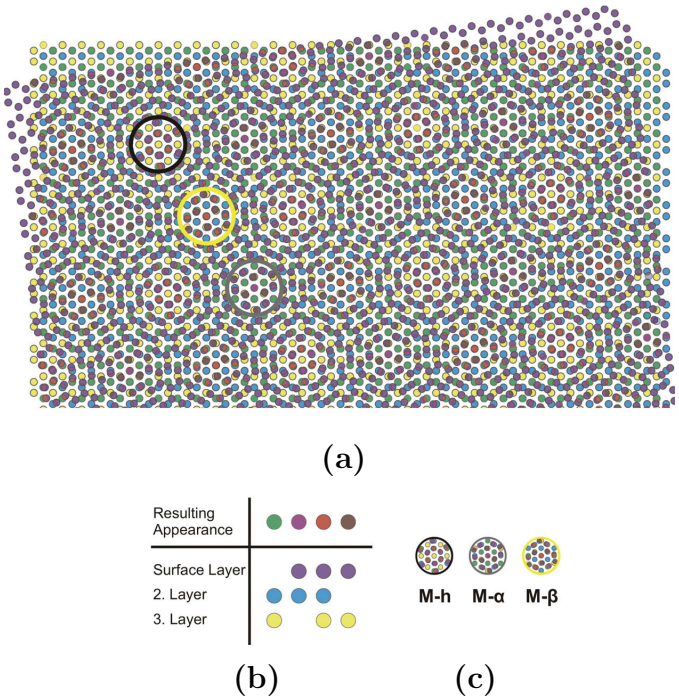

Figure 5.7: Layer superposition model to explain the formation of the Moiré rotation pattern on graphite. (a) The surface graphite layer is rotated by $\theta = 7.34°$ with respect to the underlying normally stacked layers. (b) Colour code for the resulting appearance in differently stacked areas. (c) M-α-, M-β- and M-h-sites exhibit different density of states due to different locations of atoms in the surface layer relative to the substrate crystal.

According to Xhie *et al.*, the M-β-sites of the Moiré pattern appear brightest as the atoms within these areas are located above either the hole-sites or atomic α-sites in the second layer, which will render the atoms of the M-β-sites a higher electronic density of states. Likewise, the M-α-sites are expected to be the second brightest, while the M-h-sites are the darkest in the STM images. Recent theoretical studies, based on the density functional theory, revealed that the correlation of the local stacking with the local density of states is different from this first estimation [132]. These studies showed that the M-h-sites should be the brightest in the STM image, M-β-sites the medium brightest, and M-α-sites the darkest.

In conclusion, the graphite surface is on the one hand a very advantageous substrate due to its atomic flatness, chemical inertness, ease of preparation, and applicability as a weakly interacting substrate for investigations of deposited molecules. On the other hand, the interpretaton of STM data can be hampered by the existence of various kinds of graphite surface defects. Within this thesis numerous experiments have been performed to determine whether DATC molecules self-assemble into ordered arrangements on graphite (see section 6.1). A detailed analysis of the measurements was necessary to decide about this question.

6 Self-assembly of Cor-H

This chapter describes the experimental results concerning the self-assembly of the molecule dodecakis(phenylthio)coronene (Cor-H), the basic molecular building block of this thesis. An understanding of the assembly process is gained by analyzing and comparing measurements performed for monolayers on graphite (section 6.1), on Au(111) (section 6.2), and for molecules in solution (section 6.3).

6.1 Adsorption of Cor-H on graphite

A number of STM and STS investigations on conjugated organic molecules, adsorbed on the graphite surface, have been published in recent years [123, 133]. In most cases molecules having a planar geometrical structure were used for these studies. In particular, PAH molecules (see section 2.1.2), like coronene and hexa-peri-benzocoronene (HBC), were observed to form commensurate monolayers with their molecular planes oriented parallel to the graphite surface [134–137]. Cor-H molecules (see section 4.1) are quite different from such discotic PAH systems. By simple considerations it is clear that Cor-H is not a planar molecule even though it has a planar core. Twelve phenylthio substituents are bound to the coronene core, which are forced to adopt a position above or below the plane of the core due to an assumable C-S-C angle of around $\sim 109.5°$ (tetrahedral angle of the sp^3 hybridized sulfur atoms) and the space requirement of the phenyl rings themselves (steric effects). This nonplanarity makes the molecules quite complex regarding their conformational degrees of freedom.

Much effort has been made to obtain an ordered arrangement of Cor-H molecules on the graphite surface. The solution based deposition technique described in section 4.2 was used to obtain a monolayer coverage of the graphite surface. To test the influence of the solvent evaporation rate on the molecular assembly process, solvents with different

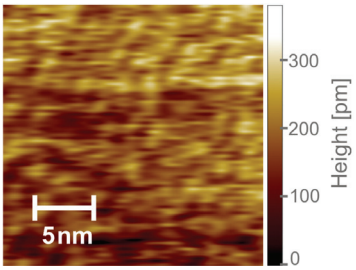

Figure 6.1: STM constant current image ($V_{sp} = 1.1\,\mathrm{V}$, $I_{sp} = 0.17\,\mathrm{nA}$, $T \approx 80\,\mathrm{K}$) obtained for the one monolayer Cor-H covered graphite surface. For the Cor-H/graphite system no ordered domains were observed. Furthermore, the residual mobility of the weakly adsorbed molecules leads to an unstable imaging.

vapour pressures (toluene, dimethylformamide, and 1,2,4-trichlorobenzene) were tested. By additionally storing the solution covered sample for varying times in an environment saturated with the vapour of the solvent, the period of the solvent evaporation was varied from one minute to more than 12 hours. Even for the lowest evaporation rate, no ordered domains of self-assembled Cor-H molecules were observed. No structural resolution at all was achieved for STM measurements at room temperature. In order to reduce thermal fluctuations, the sample was cooled down to around 80 K. But also at this temperature only indistinct and quite unstable STM images could be achieved (see Figure 6.1). It is therefore assumed that Cor-H is only weakly physisorbed and also no strong intermolecular interactions are present within the molecular layer. Residual molecular motions, induced thermally or additionally by disturbances due to the presence of the STM-tip, might prevent an imaging with STM.

This result shows that the molecules have no well-defined recognition properties, which are necessary for the formation of a distinct supramolecular order. On the other hand, weak molecule-molecule and molecule-substrate interactions should allow to obtain intrinsic electronic properties of the molecules. This issue will be further discussed on the basis of tunneling spectroscopy measurements presented in section 7.1.

6.2 Supramolecular self-assembly on Au(111)

In the following, the STM investigations of the Cor-H self-assembly on the Au(111) surface are described. The molecules were deposited on Au(111) by drop casting from a solution in toluene. The concentration and volume of the droplet were chosen such that a coverage of the Au(111) surface with approximately one monolayer was obtained. The

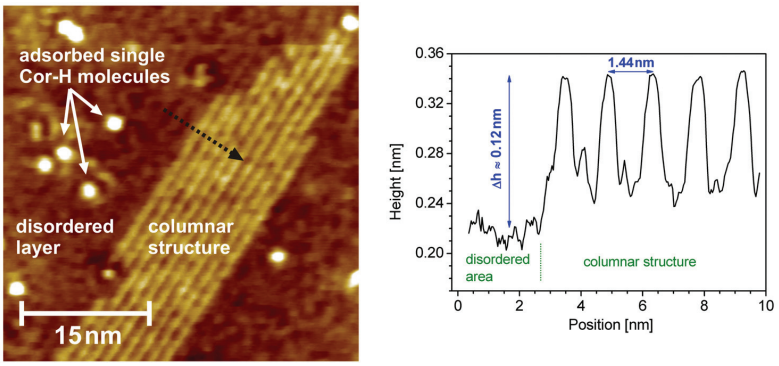

(a) **(b)**

Figure 6.2: (a) STM topographic image ($V_{sp} = 0.9\,\mathrm{V}$, $I_{sp} = 0.1\,\mathrm{nA}$) of approximately one monolayer Cor-H on Au(111). The ordered columnar structure is surrounded by a disordered monolayer, on top of which some additional physisorbed single molecules are observed (b) Height profile of the STM image in (a), obtained along the direction of the black dotted arrow.

dependence of the structure formation on the rate of solvent evaporation was tested by storing the sample in a sealed atmosphere of the solvent, so that the evaporation time was varied between one minute and one hour. Subsequent STM measurements showed no significant influence of the duration of the self-assembly process in solution on the resulting monolayer structures.

Figure 6.2(a) shows the typical surface morphology obtained for a Cor-H monolayer on Au(111). Three prominent features of the Cor-H layer are seen: areas with a disordered monolayer, some bright spots of nearly identical size, and most interestingly a well ordered phase consisting of parallel columns. The bright spots have an apparent diameter of approximately 1.7 nm corresponding to the size of a single Cor-H molecule. Hence, these spots are ascribed to single molecules adsorbed on the first molecular layer.

Previous studies concerning the adsorption of molecules with thioether groups on gold surfaces gave evidence for a pronounced affinity of this functionality towards the gold atoms [138–141]. This suggests that Cor-H molecules might adsorb on gold in a *face-on* configuration (coronene core parallel to the substrate) and that all substituents point away from the surface, since all twelve thioether groups could possibly form coordinate links to the gold atoms. In contrast to this expectation, the row structure of Cor-H is

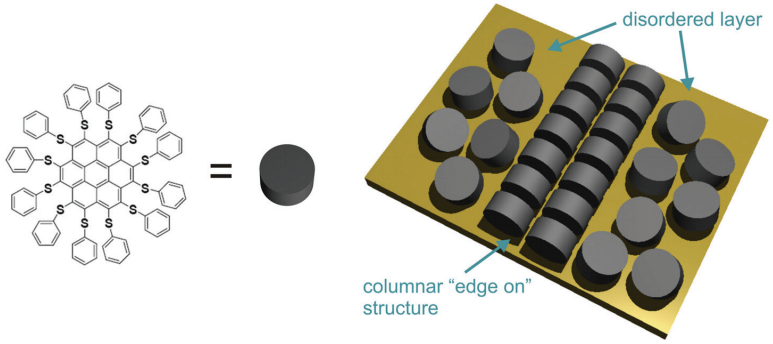

Figure 6.3: (a) Chemical structure and schematic representation of the Cor-H molecule. (b) Schematic drawing showing the suggested arrangement of Cor-H molecules on Au(111). Cor-H assembles into rows of stacked molecules with *edge-on* configuration. Disordered areas are surrounding this columnar structure.

most likely described by an arrangement with an *edge-on* orientation of the molecules as depicted in Figure 6.3. The height profile perpendicular to the rows (Figure 6.2(b)) shows that the height difference Δh between the maxima of the rows and the disordered area around the columnar structure amounts to about 0.12 nm. A higher resolution STM image of the columnar structure is shown in the inset of Figure 6.4. Within the columns one obtains protruding features having a distance of $a_{STM} = (0.49 \pm 0.05)$ nm and the separation between adjacent columns is $b_{STM} = (1.44 \pm 0.20)$ nm. Obviously, a_{STM} is linked to the $[11\bar{2}]$ direction of the underlying Au(111) surface having a next-nearest-neighbor distance of $\sqrt{3} \cdot a_{Au(111)} = 0.499$ nm, where $a_{Au(111)} = 0.288$ nm is the lattice constant of the gold surface. The alignment of the stacks to the substrate lattice is further evidenced by the relative orientation of the rows in neighboring domains. In Figure 6.4 it can be seen that the enclosed angle between the growth directions of the columns is 120° and thus reflects the hexagonal symmetry of the Au(111) surface.
For a more detailed interpretation of the obtained STM data an analysis of the Cor-H geometry is necessary. The molecular rotational degrees of freedom lead to many possible structural conformers. In section 8.1 quantum chemical calculations are aimed to identify the most stable conformations. Based on these simulations a further discussion of the Cor-H arrangement will be given in section 8.4.

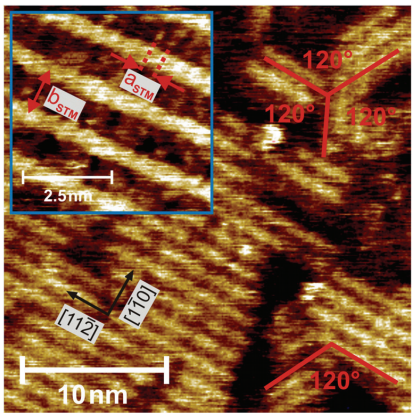

Figure 6.4: STM image ($V_{sp} = 0.6\,\mathrm{V}$, $I_{sp} = 0.09\,\mathrm{nA}$) showing the 120° rotation between the directions of columnar growth in neighboring domains. Inset: Higher resolution STM image ($V_{sp} = 0.36\,\mathrm{V}$, $I_{sp} = 0.15\,\mathrm{nA}$) of a highly ordered domain of the columnar Cor-H arrangement. a_{STM} denotes the distance between protruding features within the columns and b_{STM} the intercolumnar spacing.

6.3 Structural properties and aggregation behaviour in solution

In order to gain a first estimation of the size and shape of Cor-H or possible aggregates in the precursor solution before deposition on the surface, fluorescence correlation spectroscopy (FCS) measurements were performed. These investigations were carried out in collaboration with Dr. Habil. Silke Rathgeber at the Max Planck-Institute for Polymer Research in Mainz.

Molecular aggregations can be detected with FCS by evaluating the diffusion coefficients of the molecular species as a function of their concentration. The diffusion coefficient D is obtained from the measured fluorescence intensity correlation function

$$G(t) = \frac{1}{\bar{N}} \left(1 + \frac{4}{w_{xy}^2} Dt\right)^{-1} + 1, \tag{6.1}$$

where $\bar{N}$ is the average number of labeled molecules in the focus, t the lag time, and w_{xy} the lateral focus dimension determined by reference measurements. For details of the

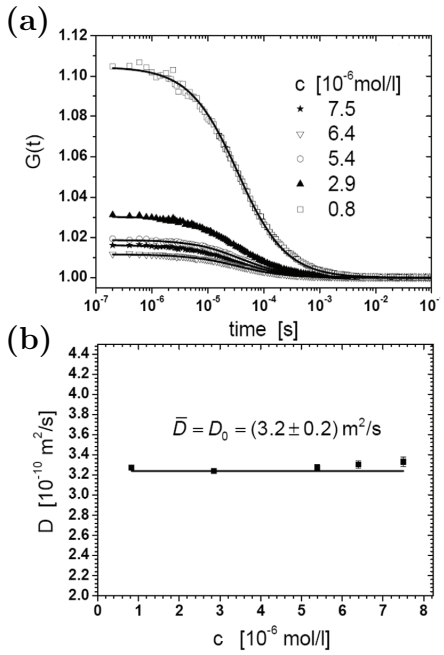

Figure 6.5: (a) FCS correlation functions measured for solutions of Cor-H in DMF with different concentrations c. The solid lines correspond to a fit of the spectra with Equation (6.1). (b) Diffusion coefficients D as a function of Cor-H concentration, determined from the fit of the FCS correlation functions. The solid line corresponds to the average value $\bar{D} = D_0$.

FCS technique and experimental procedures the reader is referred to [142] and [143]. The concentration dependence was measured for Cor-H dissolved in dimethylformamide (DMF). Figure 6.5(a) shows the measured FCS correlation functions for five samples with concentrations ranging from $c \approx 7.5 \cdot 10^{-6}$ mol/l down to $c \approx 0.8 \cdot 10^{-6}$ mol/l. The solid lines correspond to fit curves calculated by application of Equation (6.1) from which the diffusion coefficients are derived. Figure 6.5(b) presents the so obtained diffusion coefficients as a function of the Cor-H concentration. D is found to be concentration independent yielding an average value of $\bar{D} = (3.2 \pm 0.2)\mathrm{m}^2/\mathrm{s}$. Therefore, aggregations and significant intermolecular interactions in the solutions can be ruled out since both should lead to a decrease of D with increasing concentration. This is additionally evidenced by the determined magnitude of the diffusion coefficient which can be related to

the hydrodynamic radius R_h of the species in solution by the Stokes-Einstein relation

$$D_0 = \frac{k_B T}{6\pi\eta_{DMF} R_h}, \tag{6.2}$$

where D_0 is the diffusion coefficient in the limit of zero concentration and $\eta_{DMF} = 0.919\,\mathrm{Pa\,s}$ is the viscosity of DMF. By setting D_0 equal to the measured average value $\bar{D}$ the hydrodynamic radius $R_h = (0.72 \pm 0.04)\,\mathrm{nm}$ is obtained. This value can be compared to an estimated size of the Cor-H molecule. Assuming that the peripheral phenyl groups have an alternating position above and below the plane of the coronene core, the shape of the molecule can roughly be described by a cylinder. The cylinder radius and height are approximately $R \approx 0.8\,\mathrm{nm}$ and $L \approx 1.1\,\mathrm{nm}$, respectively, assuming a C-S-C angle of 109.5°. With these values the hydrodynamic radius, corresponding to a sphere having the same volume as the cylindrical molecules, i. e. $R_h \approx \sqrt[3]{3R^2L/4}$, is evaluated. The resulting value, $R_h = 0.73\,\mathrm{nm}$, agrees reasonable well with the measured hydrodynamic radius and thus confirms that Cor-H molecules are molecularly dissolved entities. The experiments allow the conclusion that strong intermolecular interactions are not present in diluted solutions. Molecular aggregates like columnar stacks are not intrinsically formed due to a pronounced intermolecular recognition. The self-assembly has to take place during the deposition process on the surface when competing solvating effects gradually decrease.

7 Impact of molecular order on charge transport characteristics

7.1 Tunneling through undisturbed molecular states

7.1.1 Tunneling spectroscopy measurements

Despite the residual mobility of Cor-H on graphite and therewith the difficulty to obtain a topographic image of the Cor-H layer, it was possible to record quite reproducible $I(V)$ characteristics when the tip was stabilized at a sufficient large tip-sample distance (high V_{sp} and low I_{sp}). Figure 7.1(a) shows a set of single $I(V)$ traces which were recorded with the tunneling setpoint values $V_{sp} = 1.45\,\mathrm{V}$ and $I_{sp} = 0.17\,\mathrm{nA}$. These characteristics clearly show a region of zero conductance around the Fermi level and a sharp rise in current above certain threshold voltages within the negative and positive bias voltage region. In Figure 7.1(b) an average of 100 single $I(V)$ curves and the corresponding normalized differential conductance (ndc) are plotted. The distinct peaks of the spectrum can be assigned to an orbital mediated tunneling (OMT) through the highest occupied (HOMO) and lowest unoccupied (LUMO) states of the Cor-H molecules. At negative sample bias a peak at a voltage of about $-1\,\mathrm{V}$ and at positive bias a peak at $1.3\,\mathrm{V}$ are observed, corresponding to tunneling through HOMO and LUMO, respectively. The measured energetic gap between these molecular states thus amounts to a value of $\Delta E_{STS} \approx 2.3\,\mathrm{eV}$. The $I(V)$ traces of Figure 7.1(a) exemplify that the onset of the orbital mediated tunneling process is not distinct. This is most obvious for tunneling through the HOMO state at negative bias voltages. These variations of the energetic position of the molecular resonances can be explained by considering

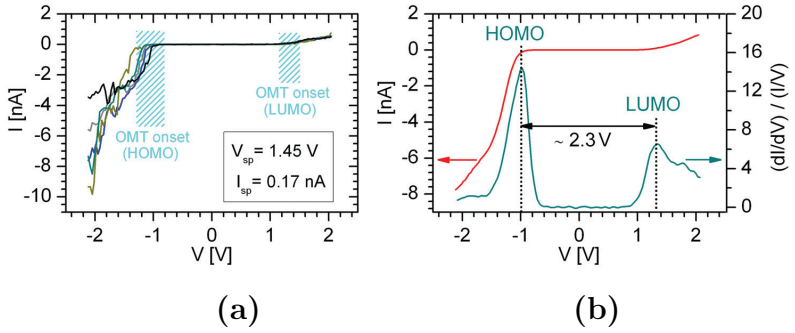

Figure 7.1: Tunneling spectroscopy data obtained on the Cor-H covered graphite surface. (a) A set of single $I(V)$ traces exemplifying the observed variations in the onset of the orbital mediated tunneling process. (b) Averaged $I(V)$ characteristic from 100 single measurements (red) and corresponding normalized differential conductance curve (green). Features due to orbital mediated tunneling through HOMO and LUMO states are observed at bias voltages of $-1\,\mathrm{V}$ and $1.3\,\mathrm{V}$, respectively.

that the molecules are not fully immobilized on the graphite surface and thus the Cor-H/substrate interface is not clearly defined. Furthermore the position of the tip with respect to specific molecular parts is not equal for different $I(V)$ measurements and also the distance to neighboring molecules is varying.

In the STM topography images of Cor-H on Au(111) (see Figure 6.2(a) of section 6.2) distinct bright spots were observed which could be assigned to non-aggregated single molecules adsorbed on the first disordered monolayer. In Figure 7.2 the STS data are plotted which were obtained after stabilizing the tip above such single molecules. It can be seen that these spectroscopic characteristics are very similar to the measured curves of the Cor-H/graphite system. The distinct peaks in the ndc curves can again be assigned to tunneling through the frontier molecular states. The measured HOMO-LUMO gap amounts to $\sim 2.2\,\mathrm{eV}$ which is comparable to the value obtained for Cor-H adsorbed on graphite. Therefore, similar to the Cor-H/graphite system, one can state that no strong electronic couplings to adjacent molecules or the substrate exist, so that mainly undisturbed frontier molecular states are probed. Local potentials of the molecules and polarization contributions may of course be different and result in variations of the measured orbital energies.

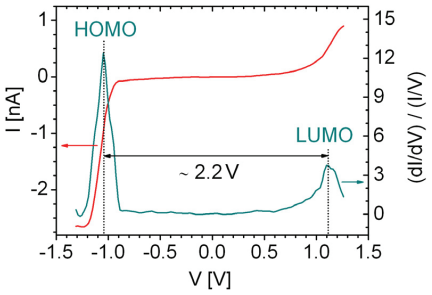

Figure 7.2: $I(V)$ characteristic (average of 20 single $I(V)$ traces with $V_{sp} = 0.9\,\mathrm{V}$ and $I_{sp} = 0.12\,\mathrm{nA}$) and corresponding ndc curve obtained for non-aggregated single Cor-H molecules adsorbed on top of the disordered Cor-H monolayer on Au(111) (see topographic STM image Figure 6.2(a) in section 6.2). The peaks in the ndc are ascribed to orbital mediated tunneling through mainly undisturbed HOMO and LUMO molecular states.

The STS measured energetic gap between occupied and unoccupied molecular orbitals can be compared to results from other spectroscopic techniques. In Figure 7.3 the UV/Vis absorption spectrum of Cor-H in DMF-solution ($c \approx 7.5 \cdot 10^{-6}\,\mathrm{mol/l}$) is shown. The optical HOMO-LUMO gap can be derived from the onset of the energetically lowest absorption band and amounts to about $\Delta E_{opt} \approx 2.05\,\mathrm{eV}$. This is the lowest neutral excitation (transition of an electron from the HOMO to the LUMO) of the molecule. In contrast, the STS technique probes energies related to a transient addition or removal of electrons, i. e. the measured gap corresponds to the difference $\Delta E = IP - EA$ between the ionization potential IP and the electron affinity EA of the molecule (see Equation (2.14)). For thin films of large π-conjugated organic molecules, the difference between ΔE and ΔE_{opt} is in the range of a few 100 meV. However, depending on the specific system, a quite large spread of values, ranging from 0.1 eV to more than 1 eV, was determined experimentally and theoretically over the past years [144–146]. The measured difference of $\sim 0.2\,\mathrm{eV}$ between ΔE_{STS} and ΔE_{opt} in the case of Cor-H lies well within this range.

Orbital mediated tunneling spectra can also be related to solution phase electrochemical measurements [37]. Electrochemical potentials are usually specified relative to a standard electrode like the saturated calomel electrode (SCE). In order to correlate these potentials to tunneling spectroscopy data, one has to reference them to an elec-

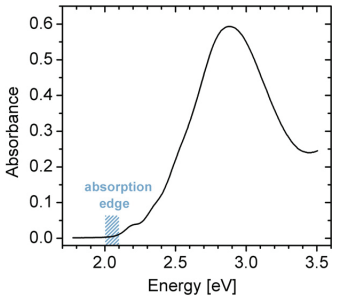

Figure 7.3: Optical absorption spectrum of Cor-H dissolved in DMF.

tron in the vacuum: $E_{1/2}(\text{vac}) = eE_{1/2}(\text{SCE}) + 4.7\,\text{eV}$, where $E_{1/2}(\text{vac})$ and $eE_{1/2}(\text{SCE})$ are the energies relative to the vacuum level and SCE, respectively [37, 147, 148]. The potential for the reversible one-electron reduction of Cor-H was measured by cyclic voltammetry in DMF to be $E_{1/2} = -0.92\,\text{V}$ vs. SCE. Thus, the electron affinity level of Cor-H is expected at an energy of 3.78 eV relative to the vacuum level. The ndc of Cor-H on graphite (see Figure 7.1(b)) showed an orbital mediated tunneling through the LUMO at a bias voltage of around 1.3 V. Therefore, this level lies at an energy $\Phi_{graphite} - 1.3\,\text{eV} = 3.3\,\text{eV}$ relative to the vacuum level, with $\Phi_{graphite} = 4.6\,\text{eV}$. The comparison to the electrochemical derived value of 3.78 eV shows that the reduction potential measured in solution can give a rough estimation of the energies which can be expected in tunneling spectroscopy measurements. The crucial differences of these two measurement techniques are the unequal degrees of relaxations as well as the differences in possible stabilization energies associated with the surrounding solvent and the polarization within the monolayer/metal system, respectively.

7.1.2 Empirical simulations of tunneling spectra

In section 7.1.1 it was mentioned that the onset of the orbital mediated tunneling process measured for the Cor-H/graphite system is varying for different $I(V)$ traces (see Figure 7.1(a)). A closer inspection of these meausurements showed that a correlation between the onset value and the maximally reached current exists. To evaluate this correlation, 15 single $I(V)$ traces having a low and another 15 traces having a high threshold voltage of the orbital mediated tunneling were selected. The averaged curves for these two cases are plotted in Figure 7.4. From the characteristics one can conclude that $I(V)$ curves with higher threshold voltages also show a steeper rise of the current

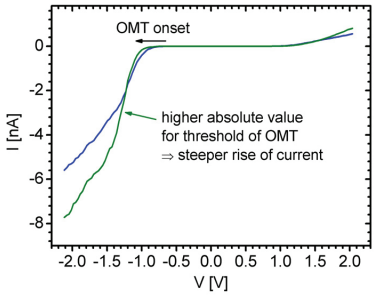

Figure 7.4: $I(V)$ characteristics averaged over 15 single curves. The blue characteristic is an average of curves having a low absolute value of the threshold voltage for orbital mediated tunneling and the green one is an average of curves with higher threshold voltage. Significant is the observation that a higher threshold voltage accompanies a steeper rise of the current after the onset of orbital mediated tunneling.

after onset, so that the current reaches a higher value after a further increase of the voltage. As will be shown in the following, these shifts can be understood on the basis of a double-barrier tunnel junction model and the charge transport equations derived in section 2.1.4. The current between the STM-tip and the graphite substrate via the electronic states of the adsorbate is given by the equation

$$I = \frac{e}{\hbar} \int_0^{eV} \mathrm{d}E \; D(E) \frac{\Gamma_t \Gamma_s}{\Gamma_t + \Gamma_s}. \tag{7.1}$$

Here, Γ_t and Γ_s describe the coupling of the adsorbate levels to the tip and to the substrate, respectively. For the STM configuration the rate $\Gamma_t/\hbar$ of electron transfer between tip and molecule is expected to be much lower than the rate $\Gamma_s/\hbar$ between substrate and molecule. Therefore, the approximation $(\Gamma_t\Gamma_s)/(\Gamma_t + \Gamma_s) \approx \Gamma_t$ can be used. The quantity $D(E)$ is the effective density of states of the adsorbate. The width of the molecular resonances is determined by the coupling of the levels primarily to the substrate ($\Gamma_s >> \Gamma_t$) and may additionally be influenced by contributions from inelastic processes, such as excitations of molecular vibronic states [149]. For simplicity, only tunneling through the occupied molecular states at negative bias voltage is considered in the following. The measured ndc of Figure 7.1(b) shows that the DOS of the occupied states is adequately described by a single Gaussian peak. The corresponding model DOS used in the calculations is depicted in Figure 7.6(a). The crucial point for the analysis

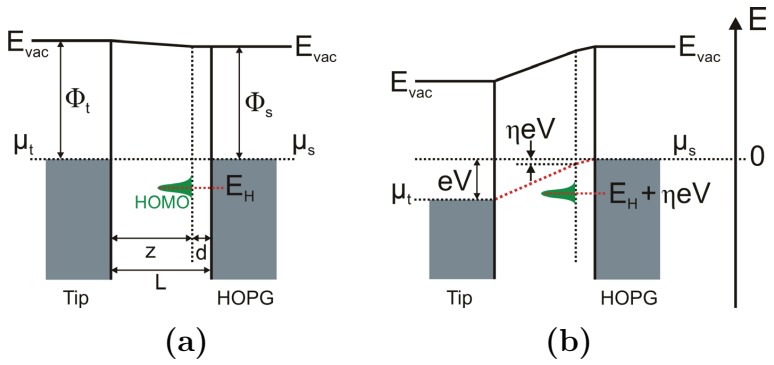

Figure 7.5: Energy level diagrams of the STM-tip/molecule/graphite junction. (a) Energetic situation at zero bias. The electrochemical potentials of the tip and the substrate are aligned ($\mu_t = \mu_s$). E_H is the energetic position of the HOMO. z and d denote the spatial separation of this molecular resonance from the tip and the substrate, respectively. (b) The case when a negative sample bias voltage V is applied. The specific junction geometry, that is the distance between the molecule and the electrodes, determines the magnitude of the voltage drop ηV occuring at the molecule-substrate interface.

of the STM-tip/molecule/graphite junction lies in the residual mobility of Cor-H on the surface. This is equivalent to a not well-defined distance of the molecule with respect to the tip and the surface even for the same values of the voltage and current set point used for stabilizing the tip. Since the electrostatic potential at the molecule is sensitive to changes of the junction geometry, the energy of a molecular state is recorded at different values with respect to the electrochemical potential of the substrate. Approximately, one can assume that the energy levels of the molecule are simply shifted by an average electrostatic potential ηeV, where η is the fraction of the bias voltage which drops between the molecule and the substrate (see Figure 7.5). If the tip and the substrate are viewed as the two plates of a parallel plate capacitor, the factor η would be given by $\eta = d/L$, where d and L are the molecule-substrate and tip-substrate separations, respectively. The evaluation of tip-sample distance dependent tunneling spectroscopy measurements by Deng and Hipps [150] showed that simple electrostatic models can only provide a qualitative description and that the potential at the molecule is much closer to that of the substrate than these models predict. Therefore, the empirical relation $\eta = d/L - C$ with a constant $C > 0$ gives a better description of the experimental

observations. A rough estimation of the expected magnitude of the parameter η can be obtained by considering characteristic values for the tip-molecule separation z and the molecule-substrate separation d. z is typically in the range of 0.5 nm [80] and the value of d at closest approach is about 0.25 nm, deduced from vdW-DFT calculations. Assuming that for this optimal configuration the fraction η is close to zero and that the molecule-substrate separation may vary due to the residual mobility by up to 0.1 nm, one obtains $\eta = d/0.75\,\mathrm{nm} - 1/3$ which varies between $\eta = 0$ for $d = 0.25$ nm to $\eta = 0.133$ for $d = 0.35$ nm. Despite the crude assumptions made, this range for the value of η properly reproduces the measured onset variations of $0.1 - 0.2$ V. The shifting of the molecular levels due to the voltage division is taken into account in the simulation by moving the energy E_H of the HOMO by ηeV for a given bias voltage V. The dependence of the tunneling rate $\Gamma_t/\hbar$ on the tip-molecule separation and the energy of the tunneling electrons is approximated by the barrier penetration term $T(E, V, z)$ for a rectangular barrier (see Equation (3.6) of section 3.2), that is

$$\Gamma_t/\hbar \propto T(E, V, z) = exp(-\beta z), \tag{7.2}$$

where the decay parameter β is written as

$$\beta = \sqrt{\frac{8m}{\hbar^2}\left(\overline{\Phi} - E + \frac{(1-\eta)\cdot eV}{2}\right)}. \tag{7.3}$$

The simulated $I(V)$ characteristics obtained from Equations (7.1)-(7.3) are plotted in Figure 7.6(b). The graph shows four characteristics corresponding to different values of η. A higher η leads to a shift of the threshold for orbital mediated tunneling through the HOMO to a more negative voltage. Additionally, the origin of a higher η is a larger molecule-substrate separation d and likewise a smaller distance $z = L - d$ between molecule and STM-tip. Because the vacuum barrier between tip and molecule is the current limiting barrier ($\Gamma_t/\hbar << \Gamma_s/\hbar$), the current rises more steeply and finally reaches a higher value in the case of a smaller z. The experimental observations are therefore qualitatively quite well reproduced with this model. Not considered were possible conformational differences of the molecules through which is tunneled. Different conformations result in different electronic structures, i. e. in energetic variations of the molecular states. However, the observed correlation between the OMT onset and the steepness of the rise in tunneling current gives a clear indication that the variations

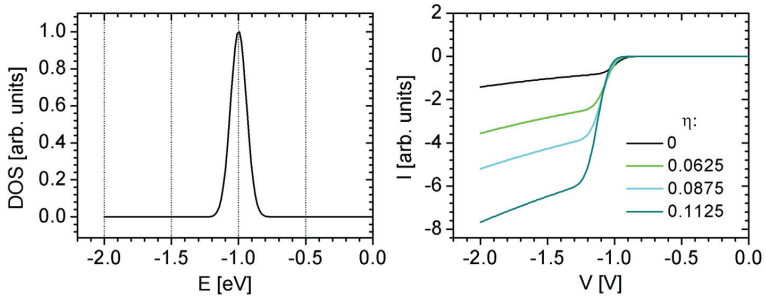

Figure 7.6: (a) Model DOS for the unoccupied molecular states used in the calculations. (b) Simulated $I(V)$ characteristics for four different values of the voltage division factor η. The molecule-substrate separation d and the tip-molecule separation z were varied from $d = 0.25\,\mathrm{nm}, z = 0.55\,\mathrm{nm}$ ($\eta = 0$) to $d = 0.34\,\mathrm{nm}, z = 0.46\,\mathrm{nm}$ ($\eta = 0.1125$). The sum $L = z + d$ was kept constant.

between different $I(V)$ traces can partially be attributed to changes of the specific position of Cor-H molecules within the tip-graphite junction.

7.2 Formation of band-like electronic states

The structural arrangement of the Cor-H molecules in the columnar stacks found on Au(111) suggest that substantial π-π-interactions between neighboring molecules exist, particularly along the direction of the rows. The STS measurements shown in the following will reveal a pronounced influence on the electronic structure when going from single molecules to ordered stacks.

Figure 7.7 shows the spectroscopy data which were measured in the area of the columnar *edge-on* arrangement of Cor-H. The plotted $I(V)$ curves correspond to different values of the current setpoint I_{sp} at a fixed voltage setpoint $V_{sp} = 0.9\,\mathrm{V}$. Each of the displayed curves represents an average over more than 100 single $I(V)$ traces. In comparison to the non-aggregated single molecules, a strongly reduced tunneling gap is observed. The corresponding ndc curves clearly show that the electronic density of states has changed considerably. It is reasonable to assign these new features to a band of states formed

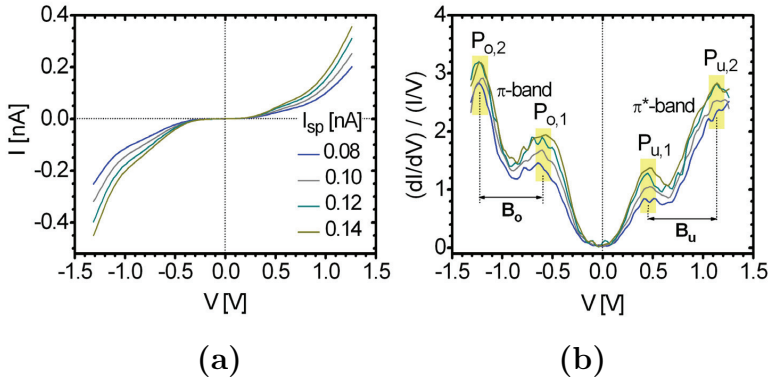

Figure 7.7: (a) $I(V)$ curves and (b) ndc versus voltage curves of stacked Cor-H molecules within the area of the columnar *edge-on* arrangement on Au(111). The peaks in the ndc can be ascribed to the increased density of states occurring at the edges of expected quasi-one-dimensional bands formed by stacking interactions mainly along the direction of the columns. The reproducible occurrence of relevant density of states features was controlled by measuring $I(V)$ curves for different values of I_{sp}, i. e. varying tip-sample distances, while keeping $V_{sp} = 0.9\,\mathrm{V}$ constant.

by the $\pi - \pi$ interactions between adjacent molecules in the columnar structure. An estimation of the strength of these interactions can be gained by applying the tight-binding model of section 2.2. The STM topographic observations suggest that the degree of electronic overlap is greater along the direction of the columns than perpendicular to them. Therefore, it can be expected that the electronic dispersion is mainly one-dimensional and can be written as $E_{o,u}(k) = \epsilon_{o,u} + 2t_{o,u}cos(ka)$ (see Equation (2.17) of section 2.2). The subscripts o and u denote the band of occupied states (π-band) and unoccupied states (π^*-band), respectively, $\epsilon_{o,u}$ are the centers of each band, and $t_{o,u}$ the transfer integrals in the direction of the columns. The Cor-H structure consists of a finite number N of interacting molecules and thus a more appropriate description is an energy spectrum with the discrete values $E_m = \epsilon_{o,u} + 2t_{o,u}cos\left[(m\pi)\,/\,(N+1)\right]$, where m is an integer ($1 \leq m \leq N$) [55]. For the measured tunneling spectra of Figure 7.7 the number of Cor-H molecules in the probed columns was around $N \approx 40$. Therefore, the peaks in the ndc can approximately be assigned to the increased density of states occurring at the band edges and the transfer integral is thus estimated to be $|t_{o,u}| \approx B_{o,u}/4$, where $B_{o,u}$ is the experimentally derived bandwidth (see Figure 7.7(b)).

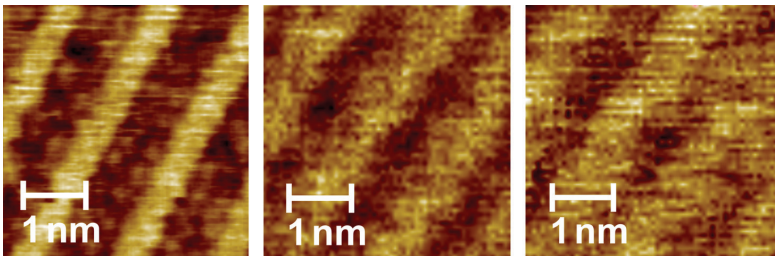

Figure 7.8: STM constant current images ($I_{sp} = 0.1\,\mathrm{nA}$) of the columnar Cor-H structure on Au(111) for scanning at bias voltages V_{sp} of (a) 0.4 V, (b) 0.9 V, and (c) 1.1 V. The appearance of the rows becomes more and more cloudy due to a increasing number of delocalized states contributing to the images.

Thus, one obtains values of $|t_o| \approx 0.16\,\mathrm{eV}$ and $|t_u| \approx 0.17\,\mathrm{eV}$. Transfer integrals and accordingly bandwidths of this magnitude are also observed in the case of π-stacks of planar PAHs [30,151,152]. This would suggest that the distance z between two coronene planes of the Cor-H molecules in the stackes should be similar to typical intracolumnar spacings of π-stacked discotic aromatic mesogens lying in the range from 0.33 nm to 0.37 nm [153–156]. Intracolumnar protruding features within the Cor-H arrangement were observed at a distance of $a_{STM} = (0.49 \pm 0.05)\,\mathrm{nm}$ (see Figure 6.4 of section 6.2). To achieve a typical vertical π-π-stacking separation z between coronene planes, the molecular plane has to be tilted by an angle $\gamma = arccos\,(z/a_{STM})$ with respect to the surface normal. For example, a coronene separation of $z = 0.35\,\mathrm{nm}$ would imply a tilt angle $\gamma \approx 45°$.

The formation of band-like states delocalized throughout the columns is further evidenced by the dependence of STM images on the applied bias voltage V. Figure 7.8 exemplifies the effect when the columnar structure is scanned at different voltages. It is observed that the rows become more and more featureless and broad when the voltage is increased. Such a dependence was observed in a variety of STM measurements using different STM-tips. Generally, it can be stated that intracolumnar features could only be resolved when the absolute value of the voltage used during scanning was in the range of 0.4 eV or bellow, but for scanning at voltages lying in the energetic window of the STS measured electronic bands, i. e. at energies subsequent to the peaks $P_{o,1}$ and $P_{u,1}$

(see Figure 7.7), the STM images showed always nearly continuous bright rows. This observation can be explained by the fact that an increasing number of states, which are delocalized throughout the columns, contribute to the STM image. Therefore, the appearance of the rows becomes more and more cloudy for increasing voltages.

The charge delocalization properties of specific organic monolayer systems on metal surfaces could so far only be detected in a few other recent studies. Käfer *et al.* [157] studied the properties of self-assembled monolayers of hexa-peri-benzocoronene (HBC) molecules on Au(111). Molecular domains of increasing size were observed to have increasing apparent heights. This was ascribed to additional current paths originating from intermolecular charge transfer. However, spectroscopic data showing the formation of a band of states was not obtained in these studies. Temirov *et al.* [158] investigated the degree of electron delocalization of nanometer-sized monolayer islands of 3,4,9,10-perylenetetracarboxylicacid-dianhydride (PTCDA) on Ag(111) by means of STS. They observed a delocalized two-dimensional band having a much stronger dispersion as expected for the organic layer alone. Their experimental observations gave some indications that a strong substrate-mediated coupling between the molecules might be the origin for the pronounced delocalization in this particular system. Gonzalez-Lakunza *et al.* [159] found by means of combined STS and DFT studies that organic-metal hybrid bands are formed in the case of the donor-acceptor complex tetrathiafulvalene-tetracyanoquinodimethane (TTF-TCNQ) on Au(111). In this case, a mixing of metal and molecular states gave rise to a one-dimensional interface band. Here, the molecular layer causes the anisotropic nature of the band, but the dispersion basically stems from the metal states.

8 Analysis of structural and electronic properties based on DFT simulations

In the following sections theoretical support of the presented STM/STS results as well as additional details of the structural and electronic properties of the Cor-H molecules will be presented. *Ab initio* calculations based on the density functional theory (DFT) were carried out by N. Atodiresei and V. Caciuc at the *Institut für Festkörperforschung* of the *Forschungszentrum Jülich*. The single molecule is already quite complex regarding its conformational degrees of freedom. Therefore, the geometrical structure and stabilities of Cor-H conformers are analyzed first (section 8.1). Thereafter, the energetics of adsorption on graphite (section 8.2) is discussed. The STS measurements for the case of Cor-H monolayers on graphite, which suggested an orbital mediated tunneling through mainly undisturbed frontier molecular states, are evidenced by electronic structure calculations (section 8.3). Finally, a refined analysis of the structural arrangement of Cor-H molecules within the columnar structure observed on Au(111) will be presented (section 8.4).

8.1 The geometrical structure of single Cor-H molecules

In the following, the geometry of two possible conformers of the isolated Cor-H molecule are considered: (i) in the *up-down* conformer 6 phenyl rings are situated above and 6 phenyl rings below the plane of the coronene unit, while (ii) in the *up-up* conformer

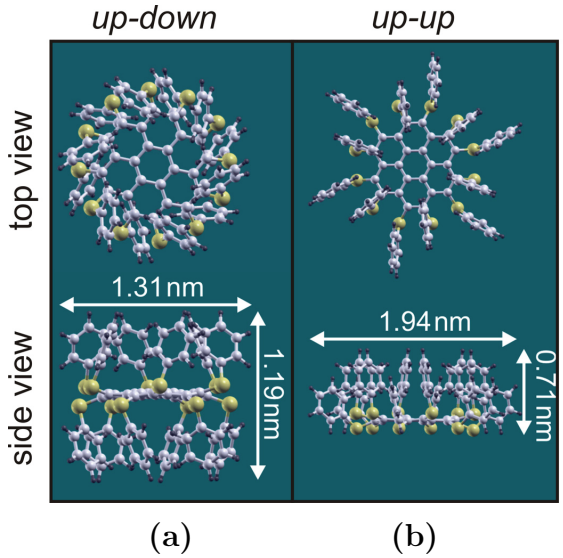

Figure 8.1: Top and side views of the optimized geometries of the isolated Cor-H conformers. (a) The *up-down* conformer has 6 phenyl rings above and 6 phenyl rings below the coronene unit (diameter: 1.31 nm, height: 1.19 nm). (b) In the *up-up* conformer all 12 phenyl rings are located above the plane of the coronene unit (diameter: 1.94 nm, height: 0.71 nm).

all 12 phenyl rings are located above the coronene plane. These are two extreme cases within a variety of other possible conformers. Therefore, it is reasonable that the geometrical dimensions, i. e. diameter and height, of all other conformers lie within the values determined for these two cases.

Figure 8.1 shows the top and side views of the optimized geometries of the isolated Cor-H conformers as derived from DFT total energy calculations, employing the generalized gradient approximation (GGA) and including semiempirical corrections to account for long-range van der Waals interactions. It turns out that the more stable conformer in the gas phase is the *up-down* configuration. The total energy difference between both conformers amounts to 0.67 eV. The lower stability of the *up-up* conformer arises to a large extent from the fact that the phenyl groups are partially pushed away from the coronene core due to steric effects, i. e. the space requirement of the substituents. Additionally, this leads to a diameter of the *up-up* conformer being considerably larger than the *up-down* conformer since in the latter no steric hindrances between adjacent

phenyl groups exist.

8.2 Energetics of adsorption on graphite

In the case of Cor-H monolayers on graphite residual motions of the molecules were assumed to prevent an imaging with STM (see section 6.1). In the following, interaction energies relevant for the Cor-H/graphite system will be evaluated to rationalize this instability of the molecular layer.

First of all, the molecule-substrate interaction (adsorption energy) plays an important role. A first estimation of the adsorption energy of Cor-H on graphite is gained when looking at the binding energies of (poly)aromatic molecules in different configurations. The adsorption energy of coronene on graphite in *face-on* configuration amounts to about 1.5 eV as derived experimentally by thermal desorption spectroscopy [160] and also calculated theoretically on the basis of *ab initio* quantum force field simulations [161]. The binding energy for benzene was determined to be around 0.5 eV in the case where the benzene plane is parallel to the graphite surface [160–163]. No data are available for the adsorption geometry with the benzene plane perpendicular to the graphite surface. An estimation for this adsorption configuration can be obtained from theoretical investigations of the benzene dimer in the T-shaped configuration having a binding energy of approximately 0.1 eV [164]. At least this value is expected when benzene is adsorbed on graphite in a perpendicular orientation. Using the theoretical results of the Cor-H geometries (see section 8.1), one can state the following. The *up-down* conformer will have a binding energy of at least 6×0.1 eV since six phenyl groups are pointing in nearly perpendicular orientation towards the graphite surface for the case when the coronene core is parallel to the surface. Since the *up-down* configuration is 0.67 eV more stable than the *up-up* conformer, an energy gain due to a transition into the *up-up* conformation is not expected because the adsorption energy of the *up-up* conformer in *face-on* configuration will most probably be in the range of coronene. The steric hindrance introduced by the bulky phenylthio substituents is therefore the decisive factor leading to low binding energies. The large size of the molecule will additionally lead to a large number of energetically similar adsorption sites and therewith to low barriers between different sites. Furthermore, different energetically comparable adsorption configurations, like *face-on* or *edge-on* adsorption, might be possible. The

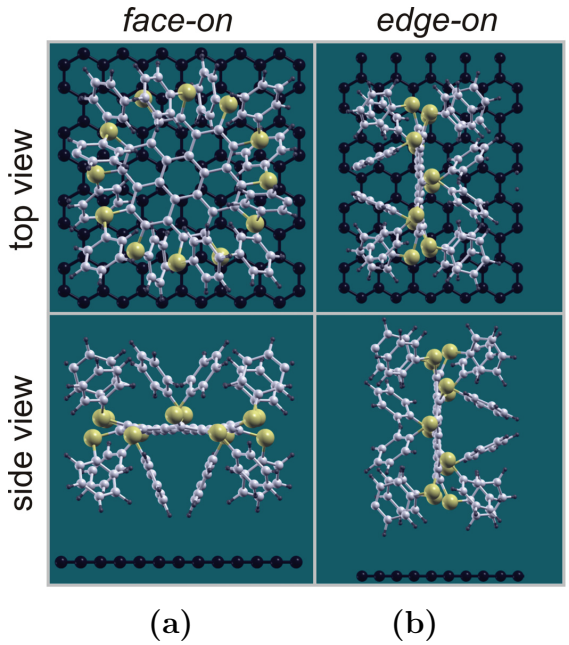

Figure 8.2: Top and side views of the (a) *face-on* and (b) *edge-on* adsorption of the Cor-H *up-down* conformer on a graphene layer, obtained from vdW-DFT calculations.

intermolecular interactions are mostly of van der Waals type and provide no selectivity and no well-defined orientation. The combined effects of low barriers for diffusion, rotations, and conformational motions together with nonselective intermolecular interactions anticipate the formation of a distinct ordered structure.

The conclusions of these simple energetic considerations are further evidenced by vdW-DFT calculations. Figure 8.2 shows the relaxed structures of the *up-down* conformer adsorbed on graphite (approximated with a single layer in the simulations) in (a) *face-on* and (b) *edge-on* configuration. The adsorption energies are calculated to be (a) 1.25 eV and (b) 0.99 eV. The difference is thus quite marginal, suggesting that molecules within the monolayer may possess different orientations with respect to the graphite surface. Generally, the calculated adsorption energies of the *up-down* conformer support the above mentioned statement that a transition into the *up-up* conformation is unlikely since it will not lead to an energetic benefit.

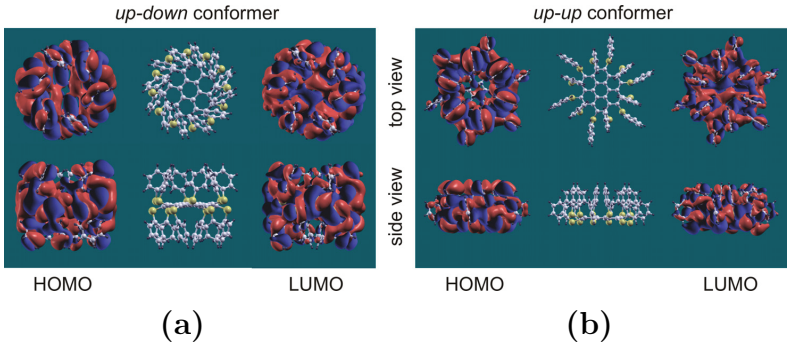

Figure 8.3: Top and side views of the HOMO and LUMO orbitals of (a) the *up-down* conformer and (b) the *up-up* conformer. For both conformers the HOMO and LUMO have different nodal planes in the coronene unit, while the phenyl rings have a structure which resembles the HOMO π-orbitals of benzene (i. e. the phenyl rings of the HOMO and LUMO have a π-type character for both conformers).

8.3 Electronic structure calculations

The STS measurements for Cor-H monolayers on graphite proved that weak molecule-molecule and molecule-substrate interactions exist, so that the spectroscopic characteristics were ascribed to orbital mediated tunneling through HOMO and LUMO states which are mainly undisturbed (see section 7.1). Electronic structure calculations presented in the following will support this experimental finding.

The HOMO and LUMO of the previously considered *up-down* and *up-up* conformers obtained from DFT calculations are plotted in Figure 8.3. For both conformers, the HOMO and LUMO have a different nodal structure in the coronene unit, while the phenyl rings have a characteristic π-structure which resembles that of the benzene HOMO π-orbitals. Notably is furthermore the result that both, the HOMO and LUMO of the Cor-H conformers, are delocalized throughout the molecular system which confirms the expectations gained from earlier spectroelectrochemistry studies of these compounds (see section 4.1).
The STS measured HOMO-LUMO gap $\Delta E_{STS} \approx 2.3\,\text{eV}$ (see section 7.1) can be compared to the theoretical value $\Delta E_{theo} = IP - EA$, where the ionization potential $IP = E_{tot}(N-1) - E_{tot}(N)$ and electron affinity $EA = E_{tot}(N) - E_{tot}(N+1)$ are calculated from the ground state total energies of the anion ($E_{tot}(N+1)$), neutral ($E_{tot}(N)$)

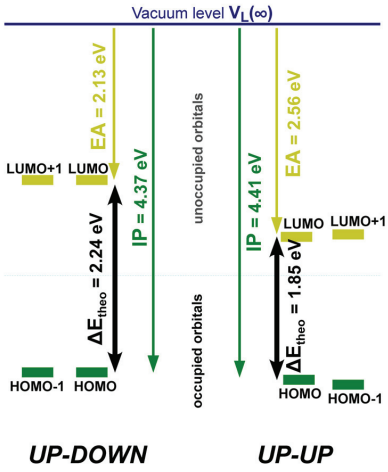

Figure 8.4: The ground state total energies of the anion ($E_{tot}(N+1)$), neutral ($E_{tot}(N)$) and cation ($E_{tot}(N-1)$) species have been used to calculate the ionization potentials $IP = E_{tot}(N-1) - E_{tot}(N)$ and electron affinities $EA = E_{tot}(N) - E_{tot}(N+1)$ of the *up-down* and *up-up* Cor-H conformers, from which the energetic gap $\Delta E_{theo} = IP - EA$ can be determined.

and cation ($E_{tot}(N-1)$) species. A schematic energy diagram for both conformers is shown in Figure 8.4. The energetic gap of the *up-down* conformer is $\Delta E_{theo} = 2.24\,\text{eV}$, while for the less stable *up-up* conformer a value of $\Delta E_{theo} = 1.85\,\text{eV}$ is obtained.
The comparison shows that the value of the HOMO-LUMO gap obtained from the tunneling spectra is in very good agreement with the theoretical value of the most stable *up-down* conformer. It is therefore very reasonable that Cor-H molecules adsorb on graphite without remarkable geometrical or electronic distortions compared to the stable gas phase *up-down* conformation.

8.4 Analysis of the adsorbate structure on Au(111)

On the basis of the theoretically derived geometries of the Cor-H conformeres (see section 8.1) a more detailed analysis of the columnar structure observed on Au(111) is

possible. The STM data of section 6.2 would suggest an arrangement of the Cor-H molecules within the columns where the coronene cores are stacked in a commensurate fashion along the $[11\bar{2}]$ direction at an intermolcular separation of $a_{STM} \approx \sqrt{3} \cdot a_{Au(111)}$. The results of the DFT calculations of the gas phase molecular geometries contradict such a stacking of the molecules. The coronene planes of the molecules might only be stacked at such a small separation if the molecules are forced to adopt a greater planarity. Taking the gas phase *up-up* conformer as starting point, a greater planarity implies an increase of the C-S-C bond angles and thus the diameter of the molecules will also increase. However, this is prohibited by the fact that in this case one can not achieve an intercolumnar distance as small as the the measured value of 1.44 nm.
It turns out that an *edge-on* adsorption in a conformation close to the more stable *up-down* geometry is consistent with the obtained STM data. The diameter of the *up-down* conformer is 1.31 nm and fits well to the observed intercolumnar spacing of $b_{STM} \approx 1.44$ nm. The height of this conformer is 1.19 nm and therefore somewhat larger than twice the distance a_{STM} of protruding intracolumnar features in the STM data. Obviously, each pair of these features has to be assigned to only one *edge-on* Cor-H molecule. The intermolecular separation along the direction of the rows is therefore $a = 2\sqrt{3} \cdot a_{Au(111)}$ and features due to protruding phenyl groups on each side of the coronene plane are observed at approximately equidistant separations of $a/2 \approx a_{STM}$ (see Figure 8.5). Furthermore, one finds that three sulfur atoms of each Cor-H molecule in *edge-on* orientation are simultaneously positioned above preferential triple hollow adsorption sites on the surface [165]. Such an adsorption configuration is quite reasonable due to the affinity of the sulfur atoms towards the gold surface, which might promote the commensurability to the substrate lattice. Strong intermolecular interactions between molecules within the rows are expected as the intermolecular distance a is smaller than the height of the isolated *up-down* conformer. As a result, the phenyl groups of adjacent molecules will interdigitate and lead to $\pi - \pi$ interactions.

DFT simulations were conducted to determine the degree of geometrical reorganization occurring during the columnar stacking of the molecules and the amount of energy which is gained due to the stacking. For this purpose the system was modeled by positioning Cor-H molecules in *edge-on* configuration onto the $Au(111)$ surface, according to the dimensions of the unit cell determined by STM, and allowing all atoms of the molecules to relax. First of all, the simulations yield that a $\left(5 \times 2\sqrt{3}\right)$ rectangular unit cell, suggested by the STM measurements, is a stable structure. The arrangement of the

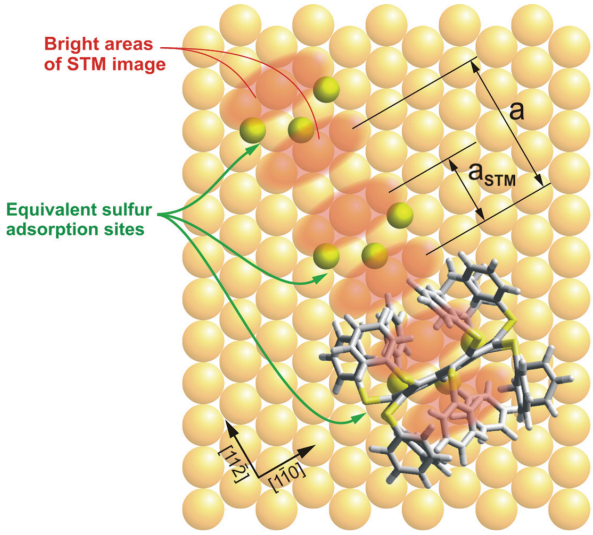

Figure 8.5: Sketch of the suggested *edge-on* adsorption of Cor-H on Au(111) showing that up to three sulfur atoms (displayed as yellow balls) of each *up-down* Cor-H conformer might point towards the substrate surface and possibly form coordinate links to the gold atoms. The columns grow along the $11\bar{2}$ direction with the Cor-H molecules positioned at equivalent adsorption sites. The intracolumnar distance between neighboring molecules amounts to $a = 2\sqrt{3} \cdot a_{Au(111)}$, where $a_{Au(111)}$ is the lattice constant of the Au(111) surface. In the STM image bright areas due to protruding phenyl-groups on each side of the coronene core are observed at approximately equidistant separations of $a/2 \approx a_{STM} = (0.49 \pm 0.05)\,\mathrm{nm}$.

molecules in the relaxed adlayer on Au(111) is shown in Figure 8.6. The sulfur atoms are observed to have no great impact on the commensurable alignment of the molecules because the phenyl groups adjacent to the surface do not allow the sulfur atoms to be strongly attached to the substrate. This is contrary to the prior expectation that the commensurability might be mainly due to a simultaneous attachment of three sulfur atoms on equivalent adsorption sites.
The most significant finding of the calculations is the energetic gain of the molecules within the molecular layer. On the one hand, the geometry of the molecules changes slightly during the relaxation in the molecular layer to achieve a commensurable stacking on the Au(111) surface with an intracolumnar separation of $a = 2\sqrt{3} \cdot a_{Au(111)}$. A small reorientation of the phenyl arms of the stable *up-down* gas phase configuration occurs during adsorption. However, only an energy of 52 meV has to be payed to achieve this geometrical adjustment. In contrast, the gain in energy due to molecule-molecule van der Waals interactions within the adlayer is found to be 2.70 eV. For comparison the binding energies of related PAH compounds, obtained from equivalent DFT calculations with dispersion corrections [155], should be mentioned. The most stable face-to-face dimers (ring separation 0.34 nm) of coronene, hexa-peri-benzocoronene (HBC) and $(H_3C(CH_2)_5)_6$-HBC have binding energies of about 0.97 eV, 1.93 eV and 2.25 eV, respectively. The kind of stacking within the Cor-H arrangement is quite different form that of planar PAHs, since the polyaromatic cores of the Cor-H molecules can not be stacked as densely as in dimers of such PAHs due to the steric hindrance of the phenylthio groups. In contrast, the comparatively large interaction energy between the molecules in the columnar Cor-H structure is a consequence of the strong interdigitation of phenyl-groups of adjacent molecules. Considering that the average contribution of aromatic carbon atoms to the interaction energy is expected to lie in the range of 50 meV [160,161] and that a total of twelve phenyl groups of each molecule interdigitate with those of adjacent molecules, the theoretically obtained strength of the interactions becomes reasonable.

In contrast to the π-π-stacking motif of planar PAH systems, in the Cor-H stacks not the polyaromatic core is responsible for the intermolecluar electronic overlap, but the peripheral phenyl groups. The HOMO and LUMO of isolated Cor-H molecules are delocalized throughout the whole molecular system and therefore an overlap between the peripheral groups will enable charge delocalization throughout the columnar stacks. The transfer integrals of occupied and unoccupied states were evaluated to be nearly

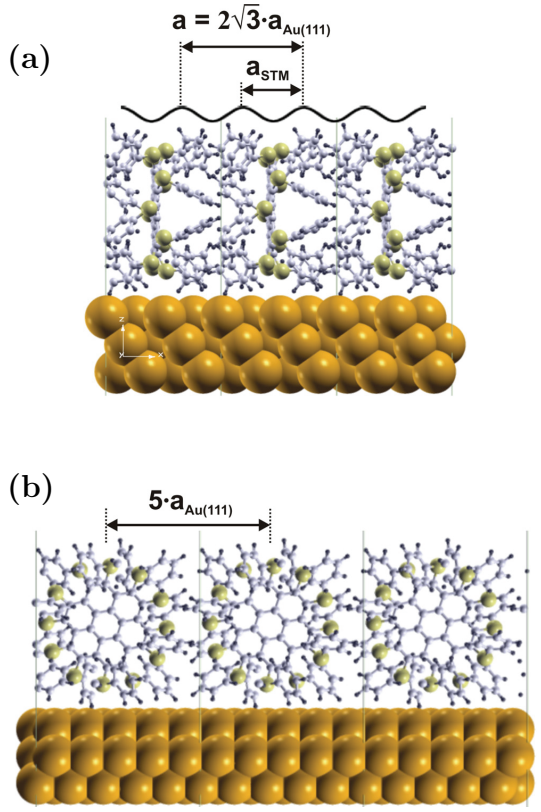

Figure 8.6: Structural arrangement of Cor-H molecules in *edge-on* orientation on the Au(111) surface obtained from DFT calculations including van der Waals interactions within the molecular layer. A stable columnar structure with a $\left(5 \times 2\sqrt{3}\right)$ rectangular unit cell is obtained. Strong intermolecular van der Waals interactions lead to a energetic gain of 2.70 eV per molecule. (a) Side view plot of the structure along the $[1\bar{1}0]$ and (b) along the $[11\bar{2}]$ direction.

equal (see the STS measurements of section 7.2). A reasonable explanation might be that this equal splitting originates from a similar orbital structure of the phenyl rings for the HOMO and LUMO of Cor-H (see section 8.3), resulting in comparable bonding and antibonding interactions of the stacked Cor-H molecules. This is certainly a first guess. The electronic structure of the Cor-H stacks is presumably also affected by interactions with the gold substrate.

8.5 Summary

The geometrical structures of possible Cor-H conformers are evaluated on the basis of vdW-DFT simulations. The most stable conformation is an *up-down* alternation of the phenyl groups above and below the plane of the coronene unit. The conformation with all phenyl arms located on the same side with respect to the coronene plane (*up-up* conformer) is 0.67 eV less stable.
Energetic considerations support the experimentally observed residual mobility of Cor-H molecules on graphite and suggest that the molecules might predominantly be adsorbed in their stable gas phase *up-down* conformation.
The latter is affirmed by the comparison of the tunneling spectroscopy measurements with electronic structure calculations. The theoretically obtained HOMO-LUMO gap of the *up-down* conformer is in very good agreement with the measured spectra. Thus, Cor-H molecules are identified to adsorb without remarkable geometrical and electronic distortions compared to their stable gas phase conformation.
A refinement of the structural arrangement of Cor-H molecules within the self-assembled columnar *edge-on* structure on Au(111) is given on the basis of the derived geometries of the molecules. It turns out that the molecules can not be stacked at an intermolecular separation of $a_{STM} = \sqrt{3} \cdot a_{Au(111)}$ within the columns. The molecules are adsorbed in *up-down* conformation and each pair of bright intracolumnar STM features has to be assigned to only one *edge-on* Cor-H molecule. DFT simulations of the columnar structure show that a substantial amount of energy is gained due to the columnar stacking within the suggested $5 \times 2\sqrt{3}$ rectangular adlayer structure.
The interdigitation of the peripheral phenyl groups causes π-π interactions between adjacent molecules, enabling charge delocalization throughout the columnar stacks. This supports the formation of band-like electronic states which are observed in STS mea-

surements. It is important to note that the properties are specific for the hybrid system of organic monolayer and metal surface. The experiments have shown that the assembly process is mediated by the substrate surface and thus it can be expected that also the electronic intermolecular coupling and therewith the formed band structure is affected by the interface between the molecules and the substrate. Electronic structure calculations of the columnar stacks including the interactions with the gold substrate were started to clarify this issue. These simulations constitute an enormous computational cost and unfortunately were not finished at the time of writing this thesis.

9 Substituent effects on structure formation and charge transport

The STM measurements of Cor-H monolayers on Au(111) revealed the formation of a columnar phase of stacked molecules in *edge-on* configuration. In the framework of discotic liquid crystals it was already observed that a clear correlation between the tendency of discotic molecules to form columnar mesophases and substituent effects exists [166, 167]. A quantitative relationship was obtained by comparing Hammett parameters, which provide a measure of the electron-withdrawing or donating ability of a functional group, with the clearing temperature of the liquid crystal columnar phase. Molecules with strongly electron-withdrawing groups formed stable columnar hexagonal mesophases over a broad temperature range, while their analogs with electron-donating substituents directly melted from the crystalline state to the isotropic liquid. These observations were explained by the stabilization of a π-π-stacking between discotic aromatic molecules due to the fact that electron-withdrawing groups help to minimize the repulsive interactions between adjacent aromatic π-systems [168, 169].

In this chapter the properties of Cor-H molecules substituted with additional electron-donating or electron-withdrawing groups are discussed. For this purpose monolayers of dodecakis(p-methoxyphenylthio)coronene (Cor-OMe) and dodecakis[p-(trifluoromethyl)phenylthio]coronene (Cor-CF3) on the Au(111) surface are prepared. The resulting surface assemblies are analyzed on the basis of STM/STS measurements and theoretically derived geometries and electronic structures of the molecules.

9.1 Cor-OMe on Au(111)

9.1.1 Structural observations

Cor-OMe films on Au(111) were prepared by applying the drop casting technique with a solution of Cor-OMe in toluene. The required concentration for one monolayer coverage was estimated by assuming that each molecule covers a surface area of $A_m = 2\,\text{nm} \times 2\,\text{nm}$ (see section 4.2). In Figure 9.1(a) the morphology of the obtained Cor-OMe layer is shown in a $70\,\text{nm} \times 70\,\text{nm}$ STM scan. First of all, it is observed that Cor-OMe does not form a columnar phase of stacked *edge-on* molecules, but seems to lie on the surface in *face-on* configuration with the coronene core oriented parallel to the surface. Furthermore, the molecules assemble within islands leaving some substrate areas uncovered. The island growth indicates that the molecule-substrate interactions are weak in the sense that the diffusion barrier is low enough to facilitate surface migration of the molecules at room temperature. The zoom-in depicted in Figure 9.1(b) shows that Cor-OMe molecules assemble into structures having a short range order with hexagonal symmetry. The intermolecular distance has an average value of approximately 1.75 nm, but deviations of up to $\pm 0.2\,\text{nm}$ are observed. Furthermore, the apparent height of the molecules is varying in the range of $< \pm 0.1\,\text{nm}$. Therefore, the interactions between the molecules seem to be neither strongly directional nor selective, leading to degrees of freedom regarding rotations, especially within the plane parallel to the surface. Small conformational differences might also be possible.
The *face-on* adsorption of Cor-OMe is in line with the previously mentioned finding that electron-donating groups anticipate the stacking of discotic aromatic molecules into columnar phases. Stronger repulsive interactions between the aromatic π-systems of the Cor-OMe molecules might probably be an explanation for their completely different adsorption configuration when compared to the columnar structure of Cor-H. However, steric effects, i. e. hindrances due to the additional methoxy groups, might be an additional reason that Cor-OMe does not assemble into columnar stacks and thus prefers a *face-on* configuration.

Regarding the STM scans, distinct intramolecular features of Cor-OMe molecules could be observed within small ordered domains when a sufficiently large negative bias voltage was used during image acquisition. Figure 9.2 shows STM images of a Cor-OMe

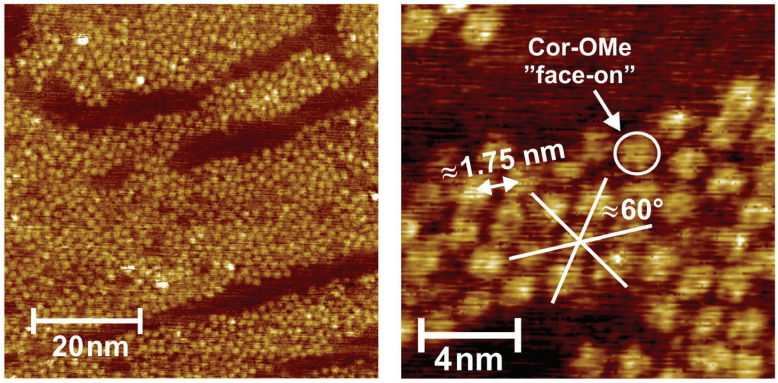

Figure 9.1: (a) STM constant current image (70 nm×70 nm, $V_{sp} = 1.2\,\mathrm{V}$, $I_{sp} = 0.12\,\mathrm{nA}$) of less than one monolayer Cor-OMe on Au(111). (b) Magnified image (15 nm × 15 nm) showing the short range hexagonal order of the Cor-OMe molecules.

arrangement which was resolved with submolecular resolution. In Figure 9.2(a) the occupied molecular states are probed ($V_{sp} = -1.3\,\mathrm{V}$), whereas in Figure 9.2(b) electrons tunnel into unoccupied states ($V_{sp} = +1.3\,\mathrm{V}$). The occupied states image clearly shows a threefold symmetry of each Cor-OMe. Since the STM images represent a combination of electronic and topographic features, it is not possible to draw an unambiguous conclusion from this observations. However, the measurements indicate that the aryl groups have a greater contribution to the molecular orbitals in the case of occupied states than in the case of unoccupied states. The occupied states STM image might therefore be more appropriate to gain information about the configuration of these substituents. The STM image 9.2(a) could therefore intuitively be explained by a configuration of the molecules where the coronene plane is parallel to the surface and alternately two adjacent aryl groups are located above and below this plane (*2up-2down* conformer). In this case, a geometrical threefold symmetry is obvious. However, it is difficult to draw a conclusion based only on the STM topography. In the following, the STM observations are therefore further analyzed on the basis of theoretically derived Cor-OMe geometries.

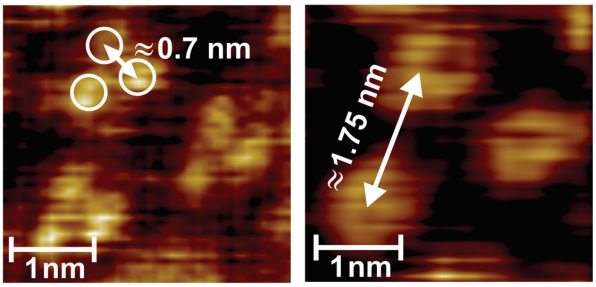

Figure 9.2: Submolecularly resolved STM images of Cor-OMe molecules on Au(111). (a) Occupied and (b) unoccupied molecular states are probed at bias voltages $V_{sp} = -1.3\,\mathrm{V}$ and $V_{sp} = 1.3\,\mathrm{V}$, respectively.

9.1.2 Analysis of molecular conformations

The geometrical structures of different Cor-OMe conformers were calculated with the same vdW-DFT method used previously for Cor-H molecules (see section 8.1). The simulations were carried out by N. Atodiresei and V. Caciuc. In addition to the conformational degrees of freedom regarding the orientation of the aryl groups relative to the coronene unit, the methoxy groups of Cor-OMe can also have varying orientations. In the following it is assumed that this orientation alternates between pointing into the direction of the molecule centre and away from the centre. In this configuration the steric hindrance between adjacent methoxy-groups is minimized and additionally weak intramolecular hydrogen bonds may be formed more easily.

The optimized geometries of three plausible Cor-OMe conformers are depicted in Figure 9.3. A threefold rotational symmetry is only obvious in the case of the *2up-2down* conformer. Interestingly, the *up-down* conformer is considerably more stable than the other two. The total energy of the *2up-2down* conformer is 1.15 eV and that of the *up-up* conformer 1.18 eV higher than that of the *up-down* conformer.

Comparing the dimensions of the conformers with the STM observation, one can state that the molecules do not adsorb in *up-up* configuration, since the diameter of this conformer ($\sim 2\,\mathrm{nm}$) is large in comparison to the measured average intermolecular distance of 1.75 nm. An interdigitation of the aryl groups of adjacent molecules is not possible

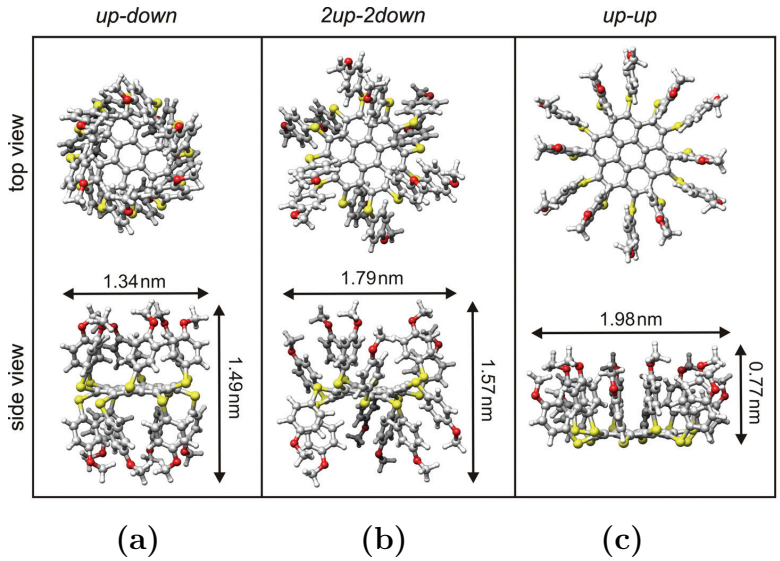

Figure 9.3: Top and side view plots of the optimized Cor-OMe conformers. (a) *up-down*, (b) *2up-2down*, and (c) *up-up* conformer.

in the case of the *up-up* conformer, because the substituents of one molecule already occupy the whole space around the coronene core. A comparison of the *up-down* and the *2up-2down* configuration with the STM observations is visualized in Figure 9.4. For the sake of clarity, only the aryl groups above the plane of the coronene core are plotted in Figure 9.4(a) and (c) for the *up-down* and the *2up-2down* conformer, respectively. Here, it can be seen that not only in the *2up-2down*, but also in the *up-down* conformer the aryl groups are arranged in pairs of two. Weak directional hydrogen bonds between methoxy groups are most probably the origin for such a pairing and therewith for the threefold symmetry. The distance between the centres of such pairs is roughly 0.75 nm and 1.1 nm for the *up-down* and the *2up-2down* conformer, respectively. If these pairs make up the bright features of the occupied states STM image, the *up-down* conformer fits almost perfectly to the measurements, as illustrates in Figure 9.4(b). The match of the measurement with the geometry of the *2up-2down* conformer is obviously not that good (Figure 9.4(d)). The significantly higher stability of the *up-down* conformer additionally indicates that this configuration should also be observed when the molecules are adsorbed on the surface. The interactions with the Au(111) surface can be

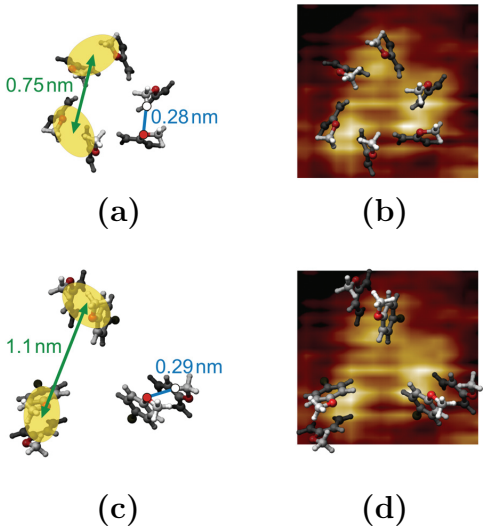

Figure 9.4: The arrangement of the aryl groups above the plane of the coronene unit is illustrated for (a) the *up-down* and (c) the *2up-2down* conformer. In both cases the aryl groups are arranged in pairs of two. The origin of such pairing is mainly due to weak directional hydrogen bonds (indicated by blue lines) between adjacent methoxy groups. The aryl pairs can be assumed to form the three bright intramolecular features of the occupied states STM images of the Cor-OMe molecules. An overlay of the geometrical structure with a STM image of one molecule is shown in (b) for the *up-down* and in (c) for the *2up-2down* conformer. Obviously, a nearly perfect match of the experimental observations is obtained in the case of the *up-down* conformer. The considerably higher stability of the latter strongly suggests that this conformation is maintained during the adsorption on the Au(111) surface.

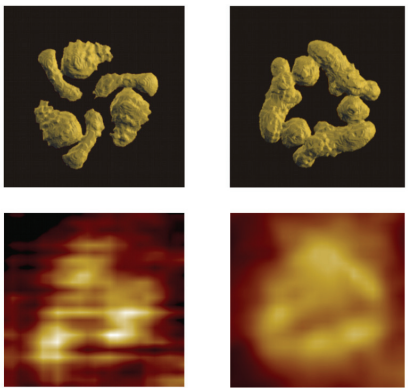

Figure 9.5: Simulated STM constant current images (upper part) of the Cor-OMe *up-down* conformer, verifying the experimental observation (lower part) that the occupied states image (left) shows up three bright features located at each pair of the aryl groups above the coronene plane, while the unoccupied states (right) rather exhibit a "triangle-like" shape.

expected to be quite similar for both conformers, and therefore no reason exists why the molecules should change their stable gas phase conformation.
Figure 9.5 shows a comparison between experimental STM images recorded for $V_{sp} = -1.3\,\mathrm{V}$ and $V_{sp} = 1.1\,\mathrm{V}$, respectively, and simulations of the occupied and unoccupied states image of the *up-down* conformer. The simulations confirm that the occupied states make up a threefold symmetric image. This symmetry is also observed in the case of the unoccupied states, but appears less pronounced with a "triangle-like" shape similar to the experimental findings.
The STM topographic indications for an adsorption of Cor-OMe in *up-down* conformation is additionally supported by tunneling spectroscopy measurements, as will be described in the following section.

9.1.3 Tunneling spectroscopy measurements

Figure 9.6 shows tunneling spectroscopy data which were measured after stabilizing the tip above Cor-OMe molecules within the short range hexagonally ordered surface arrangement. The ndc versus voltage curve of Figure 9.6(a) was obtained at a larger

tip-sample distance than that of Figure 9.6(b). It is important to note that (i) the energetic gap ΔE_{STS} between the peaks labeled N and $N+1$ is dependent on the tip-sample separation, and is larger when the tip is close to the sample, (ii) subsequent to these first peaks at positive and negative voltages, respectively, additional features are observed (denoted as $N-1$ for $V<0$ and $N+2$, $N+3$ for $V>0$), and (iii) the energy differences $E_{C,STS}$ between the peaks $N+1 \rightarrow N+2$, $N+2 \rightarrow N+3$, and $N \rightarrow N-1$ are all approximately equal for a fixed tip-sample separation, but get larger when the tip is brought closer to the sample. The following derivation will show that these characteristics can properly be explained by describing the STM-tip/molecule/substrate system as a double-barrier tunnel junction, analogous to the STS simulations of Cor-H on graphite in section 7.1.2. The energetic diagram in the inset of Figure 9.6 illustrates the relevant quantities. The energetic gap ΔE_{theo} between the ionization potential and the electron affinity can be written in terms of the CI model (section 2.1.4) as

$$\Delta E_{theo} = IP - EA = \mu_{N+1} - \mu_N = \Delta_{HL} + E_C, \tag{9.1}$$

where Δ_{HL} is the HOMO-LUMO gap of the neutral molecule and E_C is the charging energy, which is approximated to be independent on the particular charge state of the molecule. An estimation for Δ_{HL} is the optical HOMO-LUMO gap. From the onset of optical absorption, measured for Cor-OMe dissolved in toluene, a value $\Delta_{HL} \approx 2.0\,\mathrm{eV}$ is obtained.

The shift of the peak positions to higher absolute values of the bias voltage when the tip is brought closer to the sample is consistent with the model already used for the tunneling spectroscopy simulations in the case of Cor-H molecules on graphite (see section 7.1.2). The fraction η of the total bias voltage which drops between the molecule and the substrate gets larger when the tip is closer to the molecules. When the molecular energy levels are taken as a fixed reference, the electrochemical potentials of the tip (μ_t) and the substrate (μ_s) float up or down by an amount

$$\mu_t = E_F + (1-\eta)eV \tag{9.2}$$

$$\mu_s = E_F - \eta eV, \tag{9.3}$$

where E_F denotes the common electrochemical potential of the tip and substrate for $V=0$. For instance, a sequential tunneling through the LUMO of the molecule starts

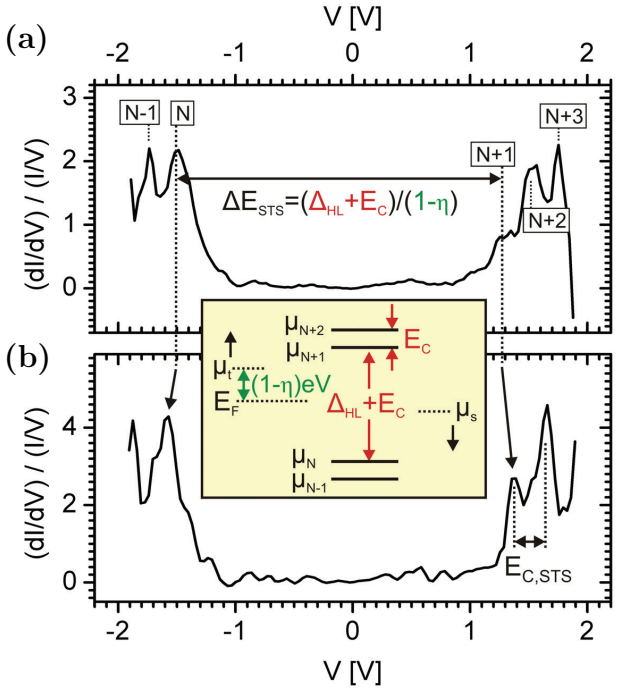

Figure 9.6: Tunneling spectroscopy data of Cor-OMe molecules within the short range hexagonal arrangement on Au(111). The shown ndc versus voltage curves were recorded with spectroscopy setpoint values of (a) $V_{sp} = 1.3\,\mathrm{V}$ and $I_{sp} = 0.08\,\mathrm{nA}$ and (b) $V_{sp} = 1.3\,\mathrm{V}$ and $I_{sp} = 0.65\,\mathrm{nA}$. The peaks N and $N+1$ are assigned to tunneling through the first ionization and electron affinity level of Cor-OMe, respectively. The measured gap ΔE_{STS} between these two levels is dependent on the tip-sample distance. ΔE_{STS} gets larger when the tip is closer to the molecules, i. e. when I_{sp} is increased. The successive features at negative and positive bias voltages, respectively, have approximately and equal spacing $E_{C,STS}$ for a fixed tip-sample separation. The STM-tip/molecule/substrate system is described as a double-barrier tunnel junction to explain the observed features. The inset shows a schematic energy diagram of the junction for $V > 0$ and illustrates the relevant quantities and notations.

	up-down	*2up-2down*	*up-up*
IP[eV]	3.88	3.32	3.55
EA[eV]	1.72	2.27	2.15
ΔE_{theo}[eV]	2.16	1.05	1.40

Table 9.1: Theoretical values of the ionization potentials (IP), electron affinities (EA) and energetic gaps $\Delta E_{theo} = IP - EA$ of the Cor-OMe conformers.

when μ_{N+1} aligns with the electrochemical potential of the tip, i. e. $\mu_{N+1} = E_F + (1-\eta)eV_{N+1}$, where V_{N+1} is the required bias voltage. Therefore, the experimentally measured transport gap between μ_{N+1} and μ_N is given by

$$\Delta E_{STS} = e(V_{N+1} - V_N) = \frac{1}{1-\eta} \cdot (\Delta_{HL} + E_C)\,. \tag{9.4}$$

The value $\Delta E_{theo} = \Delta_{HL} + E_C$, i. e. the experimentally expected value in the case of $\eta = 0$, is obtained from DFT calculations (see Table 9.1). The values 1.40 eV, 1.05 eV, and 2.16 eV are obtained for the *up-up*, *2up-2down*, and *up-down* conformer, respectively. Obviously, only the ΔE_{theo} value of the most stable *up-down* conformer is consistent with the findings of the optical absorption and STS experiments. The STM topographical measurements already indicated that the stable *up-down* conformation of Cor-OMe is maintained during adsorption on the Au(111) surface. The comparison between the spectroscopic measurements and the DFT electronic structure calculations provides an additional evidence.

With $\Delta_{HL} = 2.0\,\text{eV}$ and $\Delta E_{theo} = 2.16\,\text{eV}$ the charging energy is estimated to be $E_C = 0.16\,\text{eV}$. This value suggests that every peak of the ndc might correspond to the opening of a new tunneling channel when an additional charge state passes into the energetic window between the electrochemical potentials of the electrodes. The energetic distance between the charge states $N+1 \to N+2$ and $N \to N-1$ provides another experimental estimation for the charging energy, since the $(N+2)$-th electron can occupy the same orbital (LUMO) as the $(N+1)$-th electron and the $(N-1)$-th electron the same orbital (HOMO) as the N-th electron. Therefore E_C is approximated by

$$E_C = \mu_{N+2} - \mu_{N+1} = \mu_N - \mu_{N-1}. \tag{9.5}$$

The subsequent charge states are observed in the STS measurements with an energetic

distance

$$E_{C,STS} = e(V_{N+2} - V_{N+1}) = e(V_N - V_{N-1}) = \frac{1}{1-\eta} \cdot E_C. \tag{9.6}$$

The charging energy E_C and the parameter η for a given tip-sample distance can be derived from Equations (9.4) and (9.6) by using the measured quantities ΔE_{STS} and $E_{C,STS}$. $E_C \approx 0.19\,\text{eV}$ and $\eta \approx 0.20$ are obtained for the case of Figure 9.6(a) and $E_C \approx 0.2\,\text{eV}$ and $\eta \approx 0.26$ for the measurement of Figure 9.6(b). Therefore, both measurements yield approximately the same value for the charging energy. In addition, this result agrees very well with the value $E_C = 0.16\,\text{eV}$, estimated above by using the findings of DFT calculations and optical absorption measurements.

Furthermore, the DFT calculations yield that the Cor-OMe *up-down* conformer has two degenerate LUMO orbitals (LUMO and LUMO+1), but the subsequent LUMO+2 has an energy which is 0.6 eV higher than the first two unoccupied states. The observed tunneling spectrum is therefore not reflected in the electronic structure of the neutral Cor-OMe molecule in its ground state. This gives a further indication that the tunneling process has to involve a significant charging contribution of the molecules due to a weak coupling to both electrodes. In addition, the almost equidistant spacing between the observed peaks $N+1 \rightarrow N+2$ and $N+2 \rightarrow N+3$ is plausible since two degenerate LUMOs can be occupied. However, this is certainly a rough estimation because one can expect that the degeneracy between the LUMO and the LUMO+1 of the previous neutral molecule is lifted when the charge state has changed.

Interestingly, the gap ΔE is very close to the values measured for example in the case of Cor-H molecules on graphite. However, contrary to Cor-OMe, a sequential occupation of additional charge states was not measurable for the Cor-H/gaphite system. This can be explained with the quite high voltage division factors η in the case of Cor-OMe on Au(111), leading to a larger energetic distance between subsequent states in the measurement, which in turn is more easy to resolve. This is consistent with the fact that the methoxy groups adjacent to the substrate surface should act as spacers and give rise to an additional thin insulating tunneling barrier between the substrate and the aromatic system of the molecules.

9.2 Cor-CF3 on Au(111)

9.2.1 Structural observations

In this section, the self-assembly of Cor-CF3 molecules on Au(111) is described. A nominally one monolayer thick film was prepared by drop casting from a solution in toluene. The assembled structures shown in the following are readily obtained by performing the deposition in air, i. e. without storing the solution covered sample in a sealed atmosphere saturated by the vapour of the solvent. The evaporation of the solvent takes about one minute. Figure 9.7(a) shows a STM image of the resulting Cor-CF3 layer on Au(111). Ordered domains consisting of parallel columns, similar to the structure of Cor-H molecules on Au(111), are observed. The fraction of the gold surface covered with ordered columnar structures is higher in the case of Cor-CF3. The fraction is estimated to be $\sim 10\%$ for Cor-H and $\sim 50\%$ for Cor-CF3 in the case of a freshly prepared sample. However, the columns proceed to grow at room temperature after the solvent evaporation. The samples become "better" from day to day, i. e. show an increasing number of highly ordered columnar structures. This was observed for both Cor-H and Cor-CF3 molecules.
Figure 9.7(c) displays a high resolution image of the Cor-CF3 columnar structure. Within each row protruding features at distances a_{STM} are seen. These features are approximately equidistant with an average value of $a_{STM} = (0.47 \pm 0.05)\,\mathrm{nm}$. This points to a growth of the columns along the $[11\overline{2}]$ direction of the Au(111) surface as already observed for Cor-H molecules. The intercolumnar spacing $b_{STM} = (2.24 \pm 0.20)\,\mathrm{nm}$ is considerably larger than in the Cor-H structure. In Figure 9.7(b) a zoom-in into the STM image of Figure 9.7(a) is depicted. Some rows are interrupted and continue to grow in the same direction but with a small shift vertical to this direction. The displacement is equal to or an integer multiple of the Au(111) lattice constant $a_{Au(111)} = 0.288\,\mathrm{nm}$ and thus also points to a growth of the Cor-CF3 rows which is commensurable to the substrate surface.

As mentioned above, the growth of the columns proceeds during the STM measurements. This is exemplified in Figure 9.8, which shows three consecutively recorded STM images. It is seen that the upper row is extended and then another row begins to grow. The molecules in the disordered regions around the columnar structure are

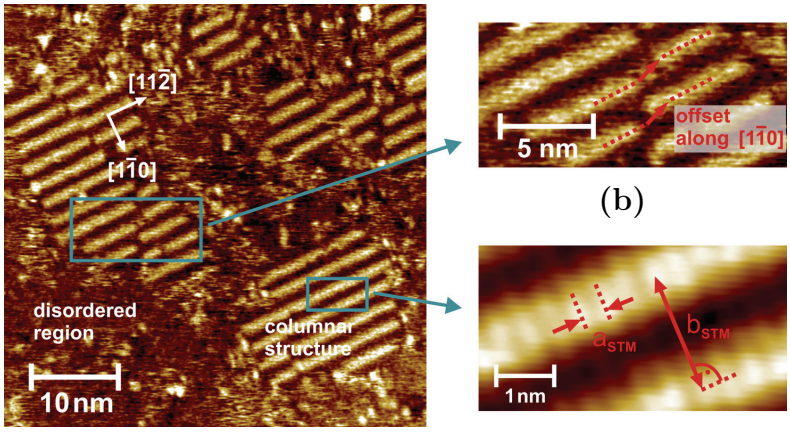

Figure 9.7: (a) STM image ($V_{sp} = 1.0\,\mathrm{V}$, $I_{sp} = 0.12\,\mathrm{nA}$) of a Cor-CF3 monolayer on Au(111). A columnar structure similar to that of Cor-H is observed. (b) Zoom-in showing columns which are offset vertical to the growth direction by an integer multiple of the Au(111) lattice constant. In the depicted case, this offset amounts to $2a_{Au(111)}$. (c) High resolution image of the structure. The distance between bright intracolumnar features has the average value $a_{STM} = (0.47 \pm 0.05)\,\mathrm{nm}$. The intercolumnar spacing is $b_{STM} = (2.24 \pm 0.20)\,\mathrm{nm}$.

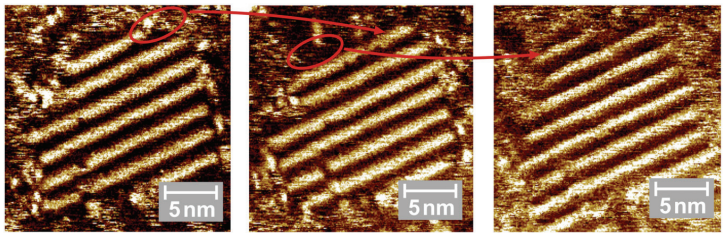

Figure 9.8: Consecutively recorded STM images showing the proceeding growth of the columns at room temperature. Regions, in which rows are developing, are marked in red colour.

thus still mobile at room temperature and can aggregate at the corners of the ordered columnar domains.

9.2.2 Tunneling spectroscopy measurements

In the STM topographic images some bright spots are observed which can be ascribed to single Cor-CF3 molecules scattered around within the disordered regions. The left part of Figure 9.9(a) shows a STM image where three Cor-CF3 molecules with a spherical shape and apparent diameters of about 1.5 nm are seen. The right part of Figure 9.9(a) depicts the obtained ndc versus voltage characteristics of these molecules. The peak positions are varying only slightly for different molecules, giving a measured HOMO-LUMO gap of roughly $\Delta E_{STS} \approx 2.4\,\mathrm{eV}$.
In a very few cases molecules are observed which might have another, less opportune, conformation. This conformer has a larger lateral size ($\sim 2\,\mathrm{nm}$ diameter) and a threefold symmetry, as shown in the STM image of Figure 9.9(b). Three bright intramolecular features with a centre to centre separation of about 1.1 nm can be seen. The HOMO-LUMO gap measured in this case is considerably reduced in comparison to the spherically shaped molecules. The ndc curve in the right part of Figure 9.9(b) yields a value of $\Delta E_{STS} \approx 1.6\,\mathrm{eV}$.
In Figure 9.10 the UV/Vis absorption spectrum of Cor-CF3 in toluene-solution ($c \approx 7.5 \cdot 10^{-6}\,\mathrm{mol/l}$) is depicted. The onset of absorption is located at an energy of about 2 eV. This indicates that the conformer of Figure 9.9(b) exists in the solution with a too small amount for detection in the absorption spectrum. This conclusion can be drawn since the STS measured gap $\Delta E_{STS} = (IP - EA)/(1 - \eta)$ (see Equation (9.4)) can be expected to be at least as large as the optical HOMO-LUMO gap. Therefore, the predominant part of the molecules has a conformation that corresponds to the STM/STS measurements of Figure 9.9(a).
The spectroscopic characteristics of the columnar structure shown in Figure 9.9(c) are obviously different from the characteristics of single molecules, both the spherically shaped and the threefold symmetric ones. It is very probable that the intermolecular electronic overlap between the densly stacked molecules of the columns alters the electronic structure of the single molecules significantly, like it was observed for Cor-H. In analogy to the findings made for Cor-H, the molecules might be stacked in a conformation that is already preferred in the case of non-aggregated molecules. The experi-

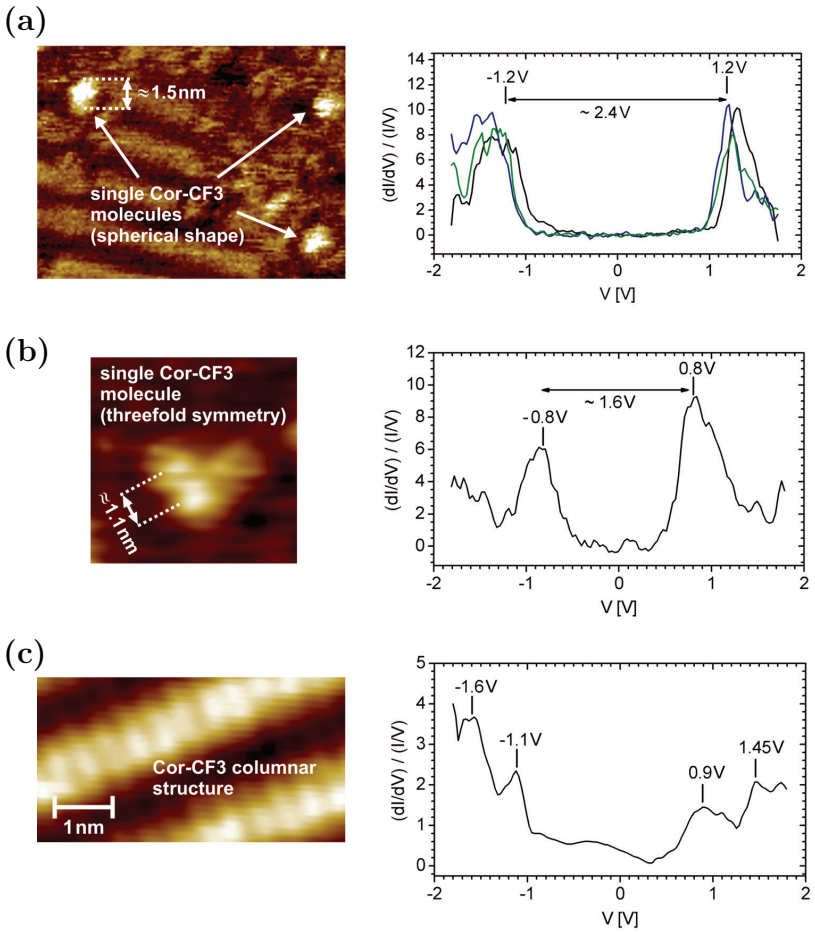

Figure 9.9: Tunneling spectroscopy data of Cor-CF3 on Au(111). All shown ndc versus voltage curves were recorded with spectroscopy setpoint values of $V_{sp} = 1.3\,\mathrm{V}$ and $I_{sp} = 0.1\,\mathrm{nA}$. (a) Single Cor-CF3 molecules with spherical shape and an apparent diameter of $\sim 1.5\,\mathrm{nm}$. (b) Single Cor-CF3 molecule with a threefold symmetry. (c) STS characteristics measured on top of the rows of the ordered Cor-CF3 columnar structure.

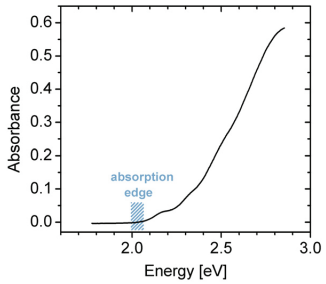

Figure 9.10: Optical absorption spectrum of Cor-CF3 dissolved in toluene.

mental findings indicate that the preferentially realized conformation should be equal to that measured in Figure 9.9(a). Thus, the pronounced DOS features of the Cor-CF3 stacks at negative voltages of −1.6 eV and −1.1 eV and at positive voltages of 0.9 eV and 1.45 eV are presumably due to a set of stabilized and destabilized HOMO/LUMO levels, respectively.

9.2.3 DFT calculations and discussion

Like for Cor-OMe, three different conformers of Cor-CF3, namely the *up-down*, *2up-2down*, and *up-up* conformer, were geometrically optimized with vdW-DFT calculations. The obtained geometries are depicted in Figure 9.11. The *2up-2down* is calculated to be the most stable one. However, the total energy of the *up-down* conformer is not significantly higher (only 0.16 eV). Like for Cor-H and Cor-OMe, the *up-up* conformer is the highest energy conformer, being 0.77 eV less stable than the *2up-2down* conformation.

Table 9.2 shows the calculated ionization potentials (IP), electron affinities (EA) and HOMO-LUMO gaps ($\Delta E_{theo} = IP - EA$) of the different conformers. The comparison of these DFT results with the measurements of Figure 9.9 allows the following statements: (i) The topographic appearance of most single molecules observed in the STM scans (Figure 9.9(a)) fits best to the DFT geometry of the *up-down* conformer, (ii) the STS measured energy gap $\Delta E_{STS} = (IP - EA)/(1 - \eta)$ in the case of these molecules agrees very well to the theoretical results of the *up-down* conformer considering the possible occurrence of a voltage drop at the molecule-substrate interface, i. e. a non-zero value of η, (iii) the rarely observed threefold symmetric appearance of Cor-CF3 molecules in the STM topographic images (Figure 9.9(b)) can be assigned to the *2up-2down*

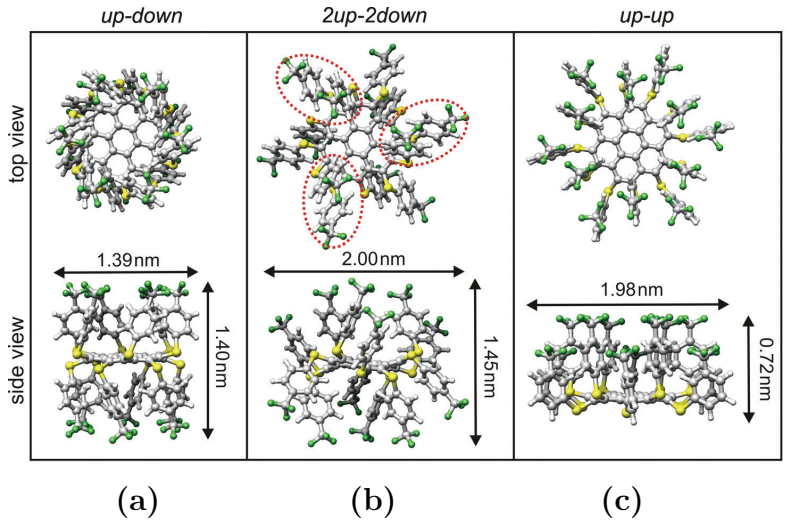

Figure 9.11: Top and side view plots of the optimized Cor-CF3 conformers. (a) *up-down*, (b) *2up-2down*, and (c) *up-up* conformer. For the *2up-2down* conformer the three pairs of aryl groups located above the plane of the coronene core have been marked by red ovals to visualize the threefold symmetry. In contrast to Cor-OMe, the aryl groups of the *up-down* Cor-CF3 conformer are not arranged in pairs of two. Thus, a circular shape with sixfold symmetry is seen in the top view.

	DFT calculations			STS measurements	
	up-down	*2up-2down*	*up-up*	*ss*	*ts*
IP[eV]	4.96	4.75	4.99		
EA[eV]	2.76	3.44	3.13		
$\Delta E_{theo/STS}$ [eV]	2.20	1.31	1.86	2.4	1.6

Table 9.2: Theoretical values of the ionization potentials (IP), electron affinities (EA) and HOMO-LUMO gaps ($\Delta E_{theo} = IP - EA$) of the Cor-CF3 conformers. Also shown are the experimentally obtained values ΔE_{STS} for the two cases of the observed topographic appearance (*ss*: spherical shape, *ts*: threefold symmetry) of the molecules (see Figure 9.9).

conformer since the experimentally measured intramolecular features fit almost perfectly to the three pairs of protruding aryl groups above the plane of the coronene core (Figure 9.11(b)), (iv) the theoretical HOMO-LUMO gap of the *2up-2down* conformer agrees also reasonable well to the measured characteristics. Considering furthermore that the UV/Vis spectrum showed no absorption below 2 eV, the conclusion can be drawn that the predominant part of Cor-CF3 molecules in solution as well as within the disordered regions on the Au(111) surface exhibit an *up-down* conformation.
Based on these findings, it is reasonable that the stacking motif of Cor-CF3 molecules in the columnar structure is similar to the determined arrangement of Cor-H, i. e. the molecules are adsorbed in *up-down* conformation and have an *edge-on* orientation within the rows. However, the CF_3 groups have an additional space requirement. Since the phenyl groups in the Cor-H columnar structure are already very densely packed, it is questionable if Cor-CF3 molecules can be stacked in the same way. DFT calculations have been started to analyze the stacking of Cor-CF3 molecules in detail, but by the time of writing this thesis these simulations were not finsished. To gain a first estimate, the columnar arrangement was modeled by much less accurate molecular mechanical calculations. The optimization was done by using the *Amber ff99* force field implemented in the molecular modeling software *UCSF Chimera*. The expected intracolumnar spacing between the molecules of $a = 2\sqrt{3} \cdot a_{Au(111)} \approx 2a_{STM}$ implies a strong interdigitation of the aryl substituents of adjacent molecules and each CF_3 group will approach the centres of the neighboring aryl rings. In order to figure out if such a close stacking is possible, a Cor-CF3 dimer was modeled, for which the distance between the coronene planes was fixed to the value $a = 2\sqrt{3} \cdot a_{Au(111)}$ during geometry optimization.

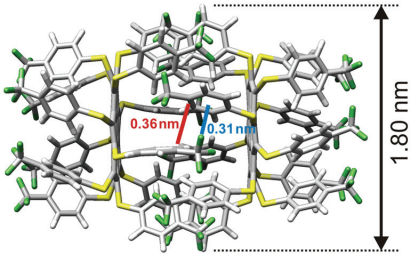

Figure 9.12: Optimized geometry of a Cor-CF3 dimer composed of two *up-down* conformers. The planes of the coronene core have been fixed at the distance $a = 2\sqrt{3} \cdot a_{Au(111)}$ during the geometry optimization. The space requirement of the aryl groups results in a widening of the C-S-C angle and therewith to an increase of the molecular diameter to 1.80 nm within the stacking region. Intermolecular C-F$\cdots\pi$ and π-π interactions are indicated by red and blue lines, respectively.

The result for this dimer is shown in Figure 9.12. The arylthio substituents within the stacking region move a little away from the coronene core, i. e. the C-S-C bond angle increases (from 100° to 108°). This brings about the required space for the interdigitation of the aryl groups. The resulting increased diameter of the stacked molecules is probably the main factor leading to the observed larger intercolumnar separation when compared to the Cor-H structure. Interestingly, the distance between fluorine atoms and the aryl ring centres of neighboring molecules is in the range of 0.31 nm, which is expected for C-F$\cdots\pi$ interactions between CF_3 groups and trifluoromethyl substituted aromatic rings [170]. Intermolecular π-π interactions can also be expected since the distance between the nearest aromatic carbon atoms is about 0.36 nm, as indicated in Figure 9.12.

The results of the dimer structure affirm that the arrangement of Cor-CF3 molecules in the columns is similar to that of Cor-H. Additional C-F$\cdots\pi$ interactions might lead to an even greater stability of the Cor-CF3 structure. However, accurate DFT simulations are still necessary to support these conclusions. Figure 9.13 shows a schematic of the suggested arrangement. The STM measurements gave evidence for a commensurable overlayer structure having a $\left(8 \times 2\sqrt{3}\right)$ rectangular unit cell. Each pair of intracolumnar bright features is again assigned to only one Cor-CF3 molecule in *edge-on* orientation. The intracolumnar appearance is certainly a combination of topographic effects, i. e. protruding aryl groups, and an electronic contribution. It has to be assumed that the

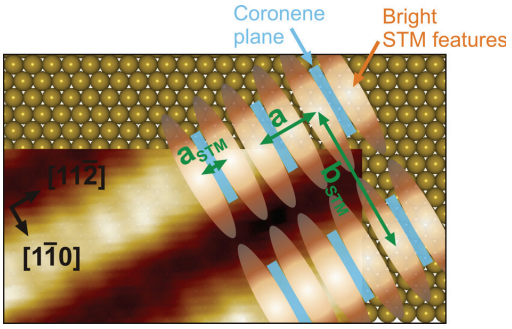

Figure 9.13: Schematic drawing of the Cor-CF3 arrangement within the columnar structure, overlayed with an experimental STM image. In analogy to the observations made for Cor-H molecules, the rows grow along the $[11\bar{2}]$ direction. The molecules are adsorbed in *up-down* conformation and lie *edge-on* on the Au(111) surface. The molecular layer has a $\left(8 \times 2\sqrt{3}\right)$ rectangular unit cell which contains two bright STM features located on both sides of the coronene plane of each molecule.

latter shifts the most intensive features seen in the STM images away from the topographic maximum into the regions directly above and below the plane of the coronene unit, resulting in bright features having apparently equidistant separations along the columnar stacks.

9.3 Summary

The self-assembly of Cor-H molecules substituted with additional electron-donating or electron-withdrawing groups is investigated by STM measurements. Cor-OMe molecules adsorb on Au(111) in a *face-on* configuration and assemble into structures with a short range hexagonal order. Intramolecular features of the Cor-OMe molecules are resolved and compared to theoretical geometries of three possible conformers and to simulated STM images based on DFT calculations. The conclusion is drawn that the molecules adsorb most probably in their stable *up-down* gas phase conformation. The latter is strongly supported by STS measurements and electronic structure calculations. The experimentally derived HOMO-LUMO gap is consistent only with the theoretical value for the *up-down* conformer. A double-barrier tunnel junction model is used to analyze the tunneling spectra. It is shown that subsequent charge states of the Cor-OMe

molecules can be resolved in the measurements.
Cor-CF3 molecules build up a highly ordered columnar *edge-on* structure on Au(111). STS measurements show that the dense stacking results in a modified electronic structure when compared to non-aggregated molecules. Like for Cor-H, this is assigned to π-π interactions between adjacent molecules in the columnar stacks. STM topographic features of adsorbed single molecules, tunneling spectroscopy data and comparisons to DFT calculations show that different conformers are possible after adsorption on the surface. The measurements show that the predominant part is presumably adsorbed in *up-down* conformation. To a much less amount a *2up-2down* conformation is observed. Preliminary geometry optimizations for a Cor-CF3 dimer suggest that the stacking motif within the columnar structure is similar to that of Cor-H. Additional C-F$\cdots\pi$ interactions might lead to an even greater stability of the Cor-CF3 structure.
It is concluded that the self-assembly of the basic building block Cor-H can strongly be affected by modifying the aryl substituents. The influence of the electron-donating or electron-withdrawing ability and therewith the magnitude of repulsive interactions between adjacent aromatic π-systems is one reason for the observed totally different self-assembly properties of Cor-OMe and Cor-CF3. However, also steric effects in the case of Cor-OMe might be another reason that a columnar stacking is unfavourable for theses molecules. Contrary, C-F$\cdots\pi$ interactions in the case of Cor-CF3 might be an additional driving force for the formation of a columnar *edge-on* structure.

10 Nanoscale structures for single molecule electronics

The STM technique is certainly a very powerful tool to study structural and electronic properties of single molecules or molecular assemblies. However, a conventional UHV-STM system can not be employed in commercial electronic products. As a first step towards molecular electronic applications, it is desirable to develop fabrication techniques for semiconducting or metallic electrodes, which are able to "wire up" single molecules. The introductory chapter of this thesis outlined some basic routes of innovative fabrication techniques for nanometer-spaced electrodes. In general, most of these methods involve (i) the definition of "rough" structures (typically some ten nanometers) by established lithographic techniques and (ii) a series of additional processes that were especially elaborated to produce pairs of electrodes with molecular scale separation.
Within this thesis, different procedures have been worked out to provide nanoscale electrode structures. This chapter summarizes the employed fabrication methods. Furthermore, preliminary charge transport measurements through Cor-OMe molecules, deposited between nanogap electrodes, are described.

10.1 Fabrication of nanometer-spaced metal electrodes

10.1.1 Direct fabrication by electron-beam lithography

The most straightforward way to fabricate electrode structures with feature sizes in the nanometer range is the use of a high-resolution lithographic technique, such as electron-beam lithography (EBL). The EBL technique consists of defining a desired structure

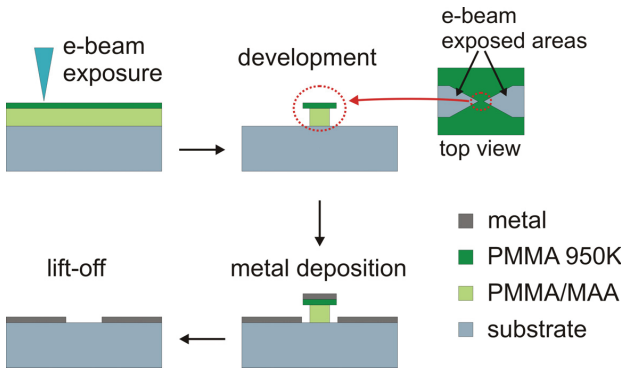

Figure 10.1: Illustration of the process steps used for patterning nanogap electrodes by EBL.

in a layer of resist by directly writing with a focused beam of electrons. The resolution of the EBL process naturally depends on the diameter of the electron beam, but the actual limiting factor is the exposure of the resist by scattered electrons. As the primary electrons of the beam traverse the resist, elastic and inelastic scattering events result in a widening of the effective beam diameter. Furthermore, as the electrons continue to penetrate through the resist into the substrate, a great part will experience large angle scattering events. These electrons may return to the resist layer at a significant distance from the incident beam and cause an additional resist exposure, known as proximity effect. The beam widening and the reward exposure of the resist account for a maximum practical resolution of $\sim 20\,\mathrm{nm}$, even for the highest resolution EBL systems.

The employed procedure for the fabrication of nanogap electrodes by EBL is illustrated in Figure 10.1 and basically consists of five steps: 1. Spin coating the substrate with resist, 2. Exposure of predefined regions with an electron beam, 3. Development, 4. Metal deposition, 5. Lift-off. Details of each step are outlined in the following.

1. The used substrates are $1\,\mathrm{inch} \times 1\,\mathrm{inch}$ pieces of Si wafers with a $400\,\mathrm{nm}$ thick thermally oxidized insulating layer on top. A two layer resist system [171] is applied in this thesis. The upper layer is poly(methyl-methacrylate), in short PMMA. The lower layer consists of poly(methyl-methacrylate/methacrylic acid), in short PMMA/MAA. The higher sensitivity of the copolymer PMMA/MAA

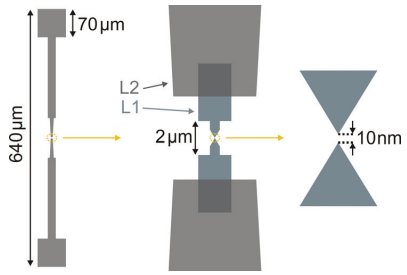

Figure 10.2: CAD layout of the electrodes. The left part shows an overview of the whole electrode structure with contact pads, the middle part the transition from the rougher features (layer L2) to the fine structure (layer L1), and the right part the merging electrode pair with a predefined 10 nm gap between them.

compared to the PMMA top layer results in an undercut resist profile, which is necessary for the lift-off process. The actual structure definition is provided by the upper layer. PMMA/MAA is applied in a 1% 2-methoxyethanol solution via spin coating with 500 rpm for 5 s and subsequently 1000 rpm for 30 s, yielding a thickness of 60 nm. Afterwards, the film is baked for 5 min on a hot plate at 200°C. 1% PMMA (950K molecular weight) in chlorobenzene is applied onto the bottom layer and spun at 500 rpm for 5 s and subsequently 6000 rpm for 30 s, yielding a total thickness of the double layer resist system of 85 nm. A final bake at 180°C for 5 min is used.

2. In this thesis, the Gaussian vector scan system EBPG 5000 Plus from Vistec Electron Beam GmbH is used. The system can be operated with a beam diameter of < 2 nm at an accelerating voltage of 50 kV. The layout of the pattern is designed with the AutoCAD program from Autodesk and converted to a machine-specific file format. The requested features are written in the form of a raster pattern. The beam current I_b and the sampling frequency f_s of the raster define the writing dose D:

$$D = \frac{I_b}{d_s^2 f_s}, \tag{10.1}$$

where d_s is the step size of the raster. The smaller the beam current is, the smaller is the beam diameter that can be achieved. The basic layout of the used electrode structures is depicted in Figure 10.2. The pattern file consists of two layers. The

layer L1 contains the nanometer-sized features, i. e. the regions around the actual nanogap, and the layer L2 the larger structures, in particular the contact pads for electrical access. Layer L1 is written with $I_b = 100\,\mathrm{pA}$, $d_s = 1.25\,\mathrm{nm}$ and layer L2 with $I_b = 150\,\mathrm{nA}$, $d_s = 50\,\mathrm{nm}$.

3. The used copolymer/polymer combination is a positively working resist system, i. e. the exposed resist areas become soluble in a developer. AR 600-55 from Allresist GmbH is used as a developer with a development time of 80s. Subsequently, the development is stopped by rinsing the sample for 60s in isopropanol (IPA).

4. Metal films are deposited by electron-beam evaporation in a vacuum system with a background pressure of $< 1 \cdot 10^{-7}\,\mathrm{mbar}$. First, a sticking layer, typically 1 nm Ti, is deposited at a rate of 0.05 nm/s. Afterwards, a 25 nm thick layer of the actual electrode material (Au or Pt) is evaporated at a deposition rate of 0.3 nm/s.

5. In the final lift-off process the remaining resist, including the metal on top, is removed by rinsing the sample in acetone. Only the predefined electrode structures remain.

The electrode separation is designed to 10 nm (see Figure 10.2). In order to determine the appropriate dose, several test series are performed. The electrode structure is written 15 times for each given dose in an interval from $150\,\mu\mathrm{C} \cdot cm^{-2}$ to $350\,\mu\mathrm{C} \cdot cm^{-2}$. First a rough dose series with steps of $25\,\mu\mathrm{C} \cdot cm^{-2}$ is performed to figure out an appropriate interval for which a subsequent finer dose test with a step size of $5\,\mu\mathrm{C} \cdot cm^{-2}$ is written. After electron-beam exposure, the samples are further processed and subsequent inspection by scanning electron microscopy (SEM) is used to characterize the electrode structures (Figure 10.3). The best yield of the predefined 10 nm electrode separation is achieved by writing the layer L1 with $250\,\mu\mathrm{C} \cdot cm^{-2}$ and the layer L2 with a somewhat lower dose of $210\,\mu\mathrm{C} \cdot cm^{-2}$. Approximately one half of the electrodes shows a $\sim 10\,\mathrm{nm}$ gap, another 30% lie in the range of $(10 \pm 5)\,\mathrm{nm}$ and the rest exhibits rather large variations (from shorted electrodes to 20 nm separations). A further increase of the dose, i. e. the use of a small overexposure, allows the fabrication of electrodes with $\leq 5\,\mathrm{nm}$ separation. However, this is not achieved reproducibly. In the best case, 20% of the electrodes have such a small gap. The other fraction is predominantly shorted. This can be explained by an increasing instability of the thin PMMA bridge when its width is decreased bellow 5 nm. The PMMA birdge is completely removed during the

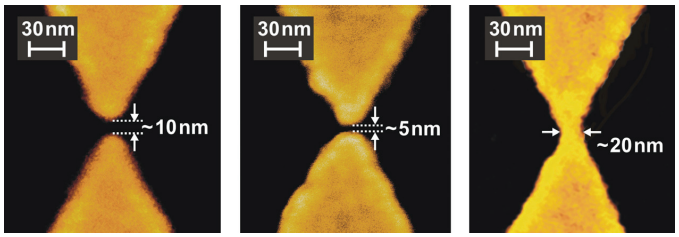

Figure 10.3: Scanning electron micrographs showing examples of processed nanogap electrodes. The structures were written with different doses: (a) $250\,\mu C \cdot cm^{-2}$ (L1), $210\,\mu C \cdot cm^{-2}$ (L2), (b) $260\,\mu C \cdot cm^{-2}$ (L1), $220\,\mu C \cdot cm^{-2}$ (L2), (c) $270\,\mu C \cdot cm^{-2}$ (L1), $230\,\mu C \cdot cm^{-2}$ (L2).

delevelopment step for a dose of $230\,\mu C \cdot cm^{-2}$ (L2) and $270\,\mu C \cdot cm^{-2}$ (L1), i. e. all electrode pairs are connected in this case.
The electrode structures obtained by EBL may thus occasionally be used to electrically address single molecules with sizes of $\leq 2\,nm$. Furthermore, the shorted electrodes provide a very narrow constriction that is useful for a subsequent nanogap fabrication by the electromigration procedure, as described in section 10.1.3.

10.1.2 Suspended nanogap electrodes with self-aligned gate

Electrodes with separations $\geq 10\,nm$ can be fabricated by the EBL process in a reproducible fashion. In this thesis, a method has been elaborated which allows to further reduce the gap size in a controllable way. The basic idea of this process lies in an additional metalization step which reduces the electrode separation due to a material deposition at the edges of the pre-patterned electrodes [172,173]. In detail, the method involves the following steps (Figure 10.4):

1. The procedure described in section 10.1.1 with an adapted CAD layout is used to pattern electrodes with gap sizes of $\sim 20\,nm$. These electrodes consist of a metal film with 1 nm Ti and 20 nm Au.

2. Buffered hydrofluoric acid (BHF) is used to isotropically etch a 100 nm thick SiO_2 layer and thus create a suspended electrode structure.

3. Conventional optical lithography is employed to define a window of 1.5 μm width above the EBL patterned electrodes. The lithography is performed with a 1.5 μm thick layer of the image reversal resist AZ 5214E from MicroChemicals® and by using the mask aligner MA6 (UV400 exposure optics) from Süss MicroTec for alignment and exposure.

4. During the second metal deposition step the reduction of the gap size is achieved. The evaporation of the metal film on top of the pre-patterned electrodes results in a build-up of material at the edges of the electrodes and thus in a decreasing electrode separation. The evaporation of 1 nm Ti/50 nm Au results in a gap size reduction of approximately 20 nm. Final electrode separations in the range of 1 nm can be produced in this way. A great advantage of the fabrication method is furthermore that a gate electrode is formed underneath the nanogap during this second metalization step. The separation between the gate and the nanogap electrodes and thus the strength of the gate coupling can be optimized by choosing an appropriate ratio of the etching depth and the thickness of the metal films.

5. The remaining photoresist and the metal deposited on top is removed during a final lift-off process.

Figure 10.5 displays scanning electron micrographs of the electrode structure after the etching process in BHF and after completion of all additional lithographic steps. The originally 20 nm large gap has been reduced to a size which can not anymore be resolved directly with SEM. However, electrodes with separations below $\sim$ 3 nm are accessible in electrical measurements. Figure 10.6 shows examples of $I(V)$ curves obtained for such nanogap electrodes. The curve of Figure 10.6(b) corresponds to the gap shown in Figure 10.5(c). By applying the Simmons model (see section 2.1.3), the electrode

Figure 10.4: Schematics of the process used to fabricate suspended nanogap electrodes with < 2 nm separation and a self-alinged gate electrode underneath the gap.

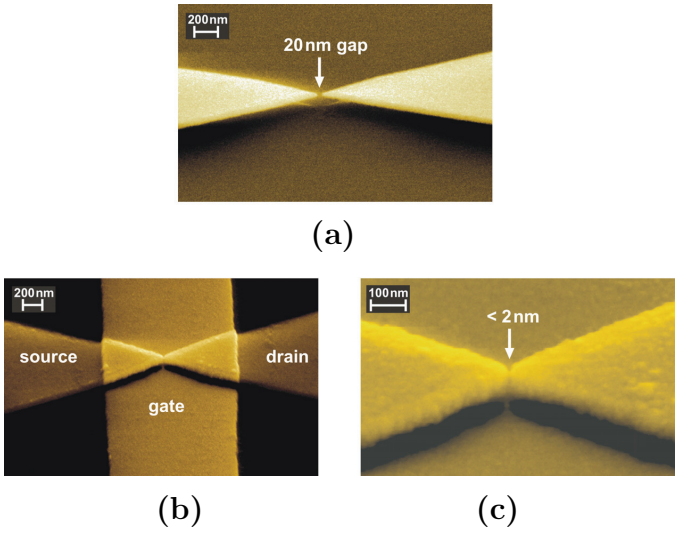

Figure 10.5: SEM images of suspended nanogap electrodes. (a) Electrodes with 20 nm separation after creating a undercut metal structure by an isotropic etch of the underlying SiO_2 substrate. (b) Electrode structure after the second evaporation step. The undercut of the source and drain electrodes ensures that no short-circuit is created between these electrodes and the self-aligned gate. (c) Zoom-in into the gap region of the electrode structure shown in (b). The gap size has been reduced considerably due to the metal build-up at the edges of the electrodes during the second evaporation step. The electrode separation is not anymore resolvable with SEM, but can be estimated to be below 2 nm.

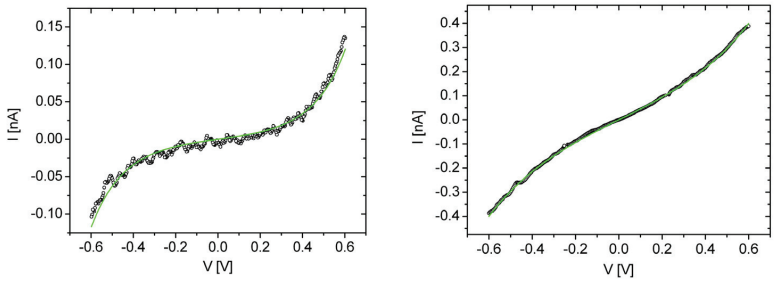

Figure 10.6: $I(V)$ characteristics of two suspended nanogap electrodes after completion of all lithographic steps. The green lines represent fits to the experimental data with Equation (2.3) of the Simmons model, yielding electrode separations of (a) $d = (1.8 \pm 0.2)$ nm and (b) $d = (1.2 \pm 0.1)$ nm. The curve (b) corresponds to the electrode depicted in Figure 10.5(c).

separation can be estimated. The least squares fit of the experimental data with Equation (2.3) yields a separation $d = (1.8 \pm 0.2)$ nm and $d = (1.2 \pm 0.1)$ nm for the $I(V)$ curves (a) and (b), respectively. This confirms that tunnel junctions have been formed with electrode separations ideal for charge transport investigations through single molecules. The yield of this procedure to fabricate nanogap electrodes with < 5 nm lies in the range of about 50% and one half of these small gaps shows tunneling characteristics. The other 50% are predominantely shorted. In a view cases the suspended electrodes break down in the course of the lithographic processes, so that these electrodes are finally electrically connected to the gate.

10.1.3 Electromigration of metallic nanowires

When a metal wire is subject to high current densities, momentum transfer from the electrons to the metal atoms leads to a movement of the atoms in the direction of the electron flow. Such current induced diffusion, called electromigration (EM), can lead to the growth of voids along the wire and finally to the formation of a gap. In the microelectronics industry, EM is a nuisance as it represents one failure mode of integrated circuit interconnects. On the other hand, the EM process was identified

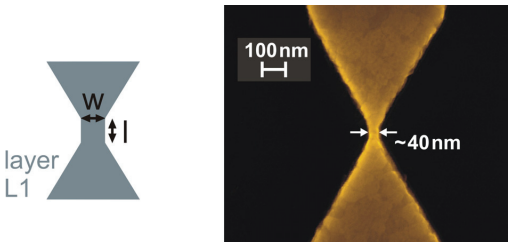

Figure 10.7: (a) Part of the CAD layout for the EM samples showing the region of the constriction in the layer L1 of the pattern file.The constriction is designed to have a length $l = 40\,\text{nm}$ and a width w between 10 nm and 100 nm. (b) Example of a processed nanowire device with $w \approx 40\,\text{nm}$. The metal film consists of 1 nm Ti/25 nm Au.

to be an advantageous process to create nanometer-spaced metal electrodes for single molecule devices [21, 174].

The preparation of nanogap electrodes by EM starts with the fabrication of a continuous metallic electrode having a narrow constriction in the middle. This constriction serves as a predefined site of fracture, since the highest current density will be located in this region. The investigated devices are fabricated by applying the EBL process steps described in section 10.1.1. The constriction is designed as a line with a length of $l = 40\,\text{nm}$ and a width w varying between about 10 nm to 100 nm. The deposited metal film consists of 1 nm Ti and an Au layer with a thickness h between 20 nm to 40 nm. Figure 10.7(a) shows the basic layout of the EBL pattern. An example of a processed sample is depicted in Figure 10.7(b).
The EM of metal atoms depends on two important quantities, namely the current density and the temperature. A phenomenological description is given by the Black equation [175, 176], describing the median time to failure (MTF) of metallic interconnects: $MTF = Aj^{-n}exp(E_a/k_BT)$. Here, A is a sample dependent constant that varies according to the geometry and microstructure of the wire, j is the current density, n is is an empirically found exponent with values between 1 and 7 [177], and E_a is the activation energy for the EM process. However, in the case of the EM process in very short and narrow nanowires, the current density and the local temperature can change very rapidly. As the cross section of the wire decreases during EM, the current density and hence the local Joule heating might increase substantially and lead to a thermal

runaway. In order to obtain electrode gaps smaller than 2 nm, it is important to prevent a divergence of the local temperature, resulting in a melting of the metal wire.

To control the speed of the EM process, an active feedback system is used in this thesis, similar to the scheme developed in Ref. [22]. The feedback is controlled by a measurement program written in the TestPoint^{TM} language. A Keithley 6430 Sub-Femtoamp Remote SourceMeter is used for sourcing voltage and measuring current. In detail, the computer controlled feedback scheme consists of the following steps: First, an initial measurement of a reference conductance G is performed at a bias voltage of $V = 100\,\mathrm{mV}$. The voltage is then ramped up at a speed of typically $3\,\mathrm{mV/s}$. After each voltage step (0.1 mV to 1 mV), the conductance is compared to the reference value. When G has dropped by a certain fraction (typically 3%) of the reference value, the voltage is ramped down from its present value V to the new value V/p, where p is normally set to 1.7. At this voltage a new reference conductance is measured. This procedure is repeated until a predefined value of the conductance is reached.

Figure 10.8 shows the typical progress of the feedback controlled EM for the example of a wire with a quite large initial cross section $A = w \times h = 100\,\mathrm{nm} \times 40\,\mathrm{nm}$. A considerable EM activity starts when a certain combination of current density and an associated local temperature due to Joule heating is reached. In the shown case, the breakage begins at a current of approximately 16 mA and thus at a critical current density $j_{EM} \approx 4 \times 10^{12}\,\mathrm{A/m^2}$, which is in the range of the values reported earlier for gold wires [178, 179]. Trouwborst *et al.* [179] have shown that the local temperature at the critical current density is typically 400 K. After reaching this critical point, the feedback control allows to prevent a thermal runaway in the junction [180]. The resistance R_c of the constriction increases during EM, since its cross section decreases. The total resistance R of the circuit can be modeled as the sum of the lead resistance R_l and the constriction resistance R_c. R_l can be determined from a measurement of the total resistance before starting the EM process, as $R_l \gg R_c$ at this initial stage. Figure 10.9 shows the resistance R_c as a function of the voltage V_c across the constriction. The green solid line indicates that R_c is approximately proportional to V_c^2, at least as long as the cross section of constriction does not fall below a critical value. Thus, the power dissipated in the constriction has roughly a constant value during the initial stage of the EM process. This critical power can be expressed as $P_{EM} = R_c \cdot I_{EM}^2$. Likewise, a

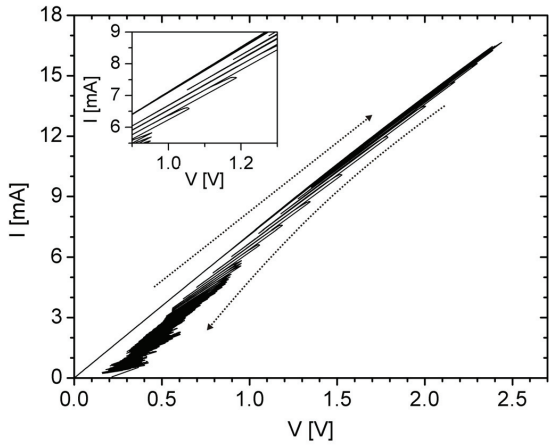

Figure 10.8: Current I versus applied voltage V during the feedback controlled EM process of a Au nonowire with an initial cross section $A = 100\,\text{nm} \times 40\,\text{nm}$. The arrow pointed upwards indicates the $I(V)$ trace for which EM has not yet started. The feedback begins to operate after the current has reached a critical value of approximately 16 mA. The inset shows one part of the EM process in more detail.

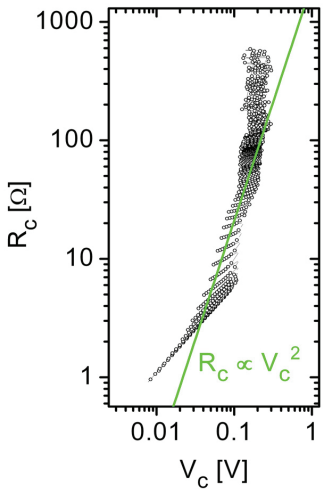

Figure 10.9: Plot of the constriction resistance R_c versus the voltage drop across the constriction during the EM process. The green solid line illustrates the proportionality of R_c to V_c^2, indicating a section of nearly constant power dissipation in the constriction during the feedback controlled EM.

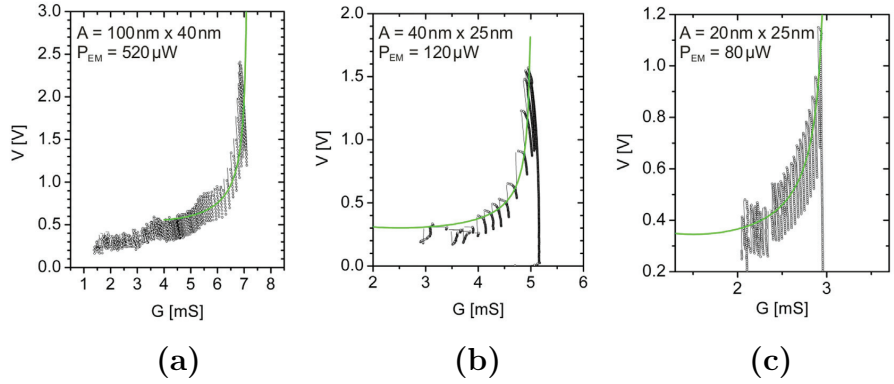

Figure 10.10: Applied voltage V versus the conductance G for samples with different cross sections $A = w \times h$ of the constriction. The green curves correspond to the model of Equation (10.2), from which the power dissipation P_{EM} in the constriction during the feedback controlled EM process is estimated. The experimental data provide evidence that the feedback loop adjusts the supplied power in order to keep a constant local temperature of the constriction.

critical voltage can be defined as

$$V_{EM} = I_{EM}(R_l + R_c) = \sqrt{P_{EM}/\left[(1 - GR_l)\,G\right]}. \tag{10.2}$$

In Figure 10.10, the applied voltage V during the feedback controlled EM is plotted versus the conductance G for device with different cross sections A of the constriction. The green solid lines represent a fit to the measured data with Equation (10.2). It is observed that the power dissipated in the constriction is roughly proportional to the cross section of the wire. Therefore, the role of the feedback is to keep a constant local temperature of the wire.

From Figure 10.9 one can see that the critical power $P_{EM} = V_C^2/R_c$ decreases when the constriction gets narrower. This is clearly seen for resistances $R_c > 100\,\Omega$. Whereas the beginning of the EM process is characterized by a smooth evolution, the late stages at high R_c values are accompanied by abrupt jumps of the conductance both up and downwards. This is due to the fact that the dimensions of the constriction approaches atomic dimensions, for which the quantized nature of the conductance becomes observable. Figure 10.11 shows the time evolution of the wire conductance G_c. Here, the

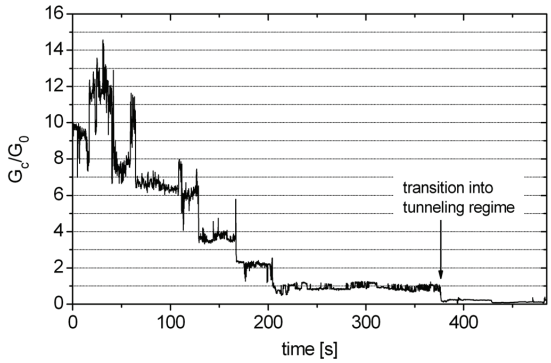

Figure 10.11: As the size of the constriction approaches the dimensions of only a few atoms, the conductance shows jumps to plateaus with values approximately equal to integer multiples of the conductance quantum G_0. The conductance was measured at a constant voltage $V = 100\,\mathrm{mV}$, subsequent to switching off the feedback controlled EM at a detected conductance below $800\,\mu\mathrm{S}$. After roughly 375 s, the ballistic atomic contact breaks and thus a tunnel junction is formed.

feedback loop had been switched off after the conductance was detected to fall below $800\,\mu\mathrm{S}$ and subsequently the conductance was measured at a fixed voltage $V = 100\,\mathrm{mV}$. The conductance shows plateaus approximately equal to integer multiples of the conductance quantum $G_0 = 2e^2/h = 77.5\,\mu\mathrm{S}$. This implies that the constriction has approached the size of only a few atoms. The number of atoms decreases to a single atom contact and finally an atomic sized gap is formed. At this point a transition from the ballistic quantum point contact regime to the tunneling regime is observed.

Figure 10.12 shows examples of $I(V)$ curves obtained for different samples after breaking the wires with the EM procedure. The curve of Figure 10.12(a) was recorded directly after the breakage. The fit with the Simmons model for voltages between $-0.25\,\mathrm{V}$ and $-0.25\,\mathrm{V}$ yields a electrode separation of only $\sim 0.5\,\mathrm{nm}$. However, a couple of experiments showed that such small gaps are quite unstable at room temperature, particularly when voltages above $\sim 0.5\,\mathrm{V}$ are applied to the device. One example is shown in Figure 10.12(b). Rearrangements of the atoms at the apex of the electrodes due to diffusion and electric field activated motions leads to substantial instabilities in the $I(V)$ characteristics. In the depicted case, the current decreases during the progress of subsequent voltage sweeps and thus the electrode separation gets probably larger. The

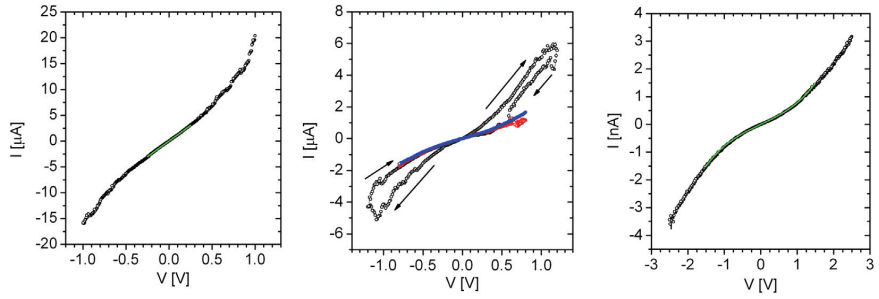

Figure 10.12: Examples of $I(V)$ curves for different nanogap junctions, recorded after the EM induced breaking process of the nanowire devices. (a) Very small gap ($\sim 0.5\,\mathrm{nm}$ according to the Simmons model). (b) Unstable tunneling characteristics (black curve) due to atomic rearrangements at the tips of the electrodes. The electrodes become more stable (blue and red curve) after some first substantial reorganizations. (c) Nanogap device with $\sim 1.5\,\mathrm{nm}$ electrode separation showing a stable tunneling characteristic up to $\pm 2.5\,\mathrm{V}$.

contrary process that a small gap evolves back into a atomic contact was also frequently observed. A stabilization of the electrode configuration in the nanogap devices could sometimes be achieved by applying a couple of voltage sweeps with a larger amplitude in the range of 1.0 V to 2.5 V, allowing to finally obtain robust tunneling characteristics for some hours. The device corresponding to the curve of Figure 10.12(c) is an example of a nanogap electrode with a separation of $\sim 1.5\,\mathrm{nm}$, being stable up to voltages of $\pm 2.5\,\mathrm{V}$.

Examples of tunneling junctions fabricated by the EM procedure are shown in the scanning electron micrographs of Figure 10.13. The nanogap in (a) corresponds to the device with the $I(V)$ characteristic of Figure 10.12(a). The SEM images confirm that very small and well defined gaps can be prepared by the EM method. Typically, the electrode biased negative during the EM process is tapered more sharply (upper electrode in the shown images). This can be explained with the fact that the current induced atomic diffusion during the EM process occurs along the direction of the electron flow. Therefore, atoms of the most narrow part of the wire are transported downwards, resulting in an accumulation of atoms at the lower part of the constriction

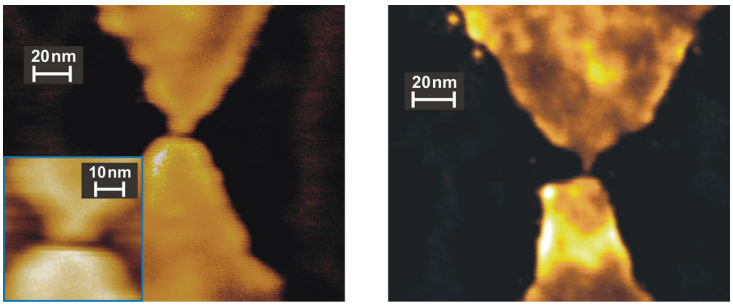

Figure 10.13: SEM images of nanogap electrodes prepared by the controlled EM technique.

and a narrowing at the upper part.

10.2 Electrical transport through Cor-OMe between nanogap electrodes

Nanogap junctions fabricated by the EM technique provide an electrode separation ideal for embedding single molecules. However, the stability of the Au electrodes at room temperature is only rarely sufficient enough to study electron transport through single or a few molecules. Cooling down the samples to liquid helium temperatures allows to reduce the mobility of the gold atoms. Low temperature measurements of electron transport through molecules between EM fabricated nanogap electrodes were so far typically performed by first depositing molecules on the nanowires, then cooling down, performing EM at low temperature, and finally characterizing molecules which occasionally might have bridged the electrode pair [181–183]. This approach is quite precarious since (i) the local temperature during EM might be high enough for the decomposition of some molecular species and (ii) nanometer-sized gold grains may be formed during the EM process within the nanogap junction, thus hampering an unambiguous distinction between transport through molecules and such metal islands [184–187]. Therefore, a more suitable way for studying charge transport through molecules is probably the procedure of first fabricating nanogap electrodes under ambient conditions, then char-

acterizing the bare tunnel junctions, and finally depositing molecules. Thereafter, the samples may also be cooled down to perform low temperature measurements.

Within this thesis, some first "trial-and-error" room-temperature measurements were performed to proof the usability of the fabricated electrode structures for charge transport studies through molecules. Cor-OMe was considered as a suitable test molecule for these studies. The molecules have been investigated in detail by STM/STS measurements before (see section 9.1). These investigations showed that Cor-OMe does not form molecular aggregates, thus providing the possibility that charge transport characteristics specific for single molecules might be observable.

Measurements were performed in the following way. Five nanowires were broken with the feedback controlled EM technique. Thereafter, the gaps were characterized by electrical measurements. The sizes of two gaps were beyond the measurable resistance range, the other three showed tunneling characteristics indicating electrode separations of $< 2\,\mathrm{nm}$. Two of the latter could not be stabilized sufficiently by voltage sweeps. Thus, effectively only one well suited tunneling junction remained. The corresponding $I(V)$ curve, already shown in Figure 10.12(c), was stable up to at least $\pm 2.5\,\mathrm{V}$. The Simmons model yielded an electrode separation of $\sim 1.5\,\mathrm{nm}$. Cor-OMe was subsequently deposited by applying a $10\,\mu\mathrm{l}$ droplet of a solution in toluene ($c \approx 5{\cdot}10^{-6}\,\mathrm{mol/l}$) onto the samples. After solvent evaporation, the electrical characterization was performed. Clear evidence for deposited molecules could be observed only in the case of the previously stable bare junction with $\sim 1.5\,\mathrm{nm}$ electrode separation.

Figure 10.14(a) displays the $I(V)$ curves of the nanogap junction after depositing Cor-OMe. In contrast to the bare tunnel junction, pronounced rises of the current, beginning at roughly $\pm 1\,\mathrm{V}$, are observed. The corresponding differential conductance dI/dV versus voltage curves, depicted in Figure 10.14(b), shows maxima located at $-1.6\,\mathrm{V}$ and $+1.5\,\mathrm{V}$, respectively. It is reasonable that these features are due to a resonant transport through the frontier molecular states of the Cor-OMe molecules. In the STS measurements of Cor-OMe (section 9.1.3), the transport via subsequent charge states of molecules could be resolved. In the nanogap junction measurements, this is not the case. In contrast, quite broad features are seen in these measurements. However, the absolute distance $\Delta E_{exp}/e \approx 3.1\,\mathrm{V}$ between the peaks agrees well with the STS measurements, considering that the molecule might be more equally coupled to the electrodes than it is the case in the STM configuration. The experimental STS results were consistent with

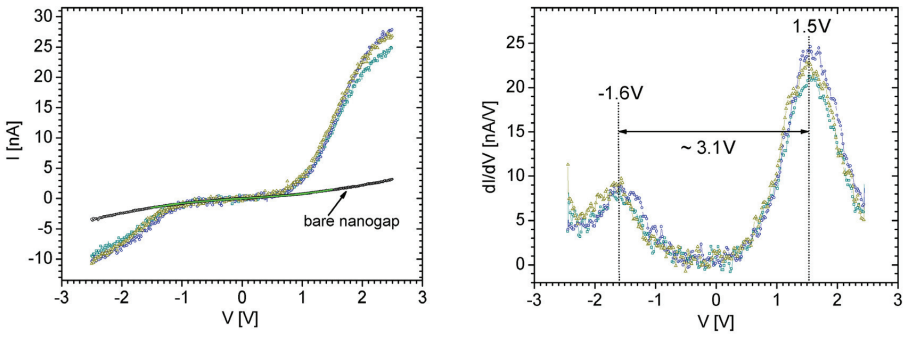

Figure 10.14: (a) $I(V)$ characteristics of a nanogap junction after depositing Cor-OMe molecules. The charge transport through the junction has changed significantly, when compared to the $I(V)$ curve of the bare nanogap. (b) Differential conductance versus voltage curve, obtained numerically from the corresponding $I(V)$ curves in (a). The broad DOS features are very probable due to a resonant charge transport through the frontier molecular states of Cor-OMe.

the DFT derived energetic gap $\Delta E_{theo} = IP - EA = 2.16\,\text{eV}$ of Cor-OMe in its most stable *up-down* conformation. The measured gap ΔE_{STS} was seen to become larger when the tip is brought closer to the molecule. Values $\Delta E_{STS} = [1/(1-\eta)] \cdot \Delta E_{theo}$ of $\sim 2.7\,\text{eV}$ ($\eta = 0.2$) for $V_{sp} = 1.3\,\text{V}/I_{sp} = 0.08\,\text{nA}$ and $\sim 2.9\,\text{eV}$ ($\eta = 0.26$) for $V_{sp} = 1.3\,\text{V}/I_{sp} = 0.65\,\text{nA}$ were derived. In the nanogap junction measurements, a higher value of η is very reasonable, since the electrode separation ($\sim 1.5\,\text{nm}$) is similar to the dimensions of the molecule, as illustrated in Figure 10.15. It can be expected that the second electrode (corresponding to the tip in the STS measurements) has a quite similar distance to the molecule as the other electrode (corresponding to the Au(111) substrate in the STS measurements). This is also supported by comparing the range of meausred currents. In the nanogap junction a current $I \approx 8\,\text{nA}$ is flowing at a voltage of 1.3 V, a factor of 100 ($\eta = 0.2$) and a factor of 10 ($\eta = 0.26$) higher than in the STS experiments. From

$$\Delta E_{exp} = \frac{1}{1-\eta} \cdot \Delta E_{theo} \approx 3.1\,\text{eV} \tag{10.3}$$

the value $\eta = 0.3$ is obtained. Therefore, a roughly linear increase of η with every order of magnitude increase in current is observed. This finding is plausible due to the

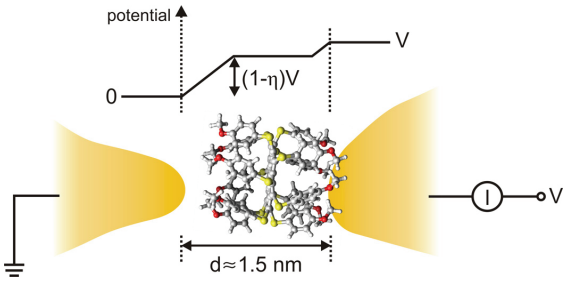

Figure 10.15: Illustration of the nanogap junction consisting of an electrode pair with 1.5 nm separation and an embedded Cor-OMe molecule in *up-down* conformation.

exponential dependence of the overall current from the the electrode-molecule separation of the larger (current limiting) barrier.
The fact that subsequent charge states of the molecules can not be resolved in the measurements may have different origins. Variations of the molecule-electrode couplings during the measurements or fluctuations of the ambient environment can lead to a broadening. It is also possible that more than one molecule is attached to the electrodes. The clear resonances of the single molecules might be smeared out in this way, resulting in a broader effective DOS in the measurement. Additional measurements are necessary to gain a more detailed understanding of the charge transport processes in this set-up. In particular, gate dependent measurements in an inert atmosphere and low temperature measurements would be very useful for further investigations. By this means, also a stepwise charging of the molecules should be observable.

10.3 Summary

This chapter described different fabrication techniques for nanometer-spaced metal electrodes and their usability for contacting molecules for charge transport measurements. Electrodes down to 10 nm can be fabricated directly with electron-beam lithography (EBL) in a reproducible fashion. A further reduction of the gap size is accompanied by a decreasing yield.
Another approach consists of first fabricating nanogaps of $\sim$ 20 nm by EBL and subsequently reducing the gap size by additional process steps. The predefined electrodes

are undercut by an isotropic etch and a second evaporation step results in a reduction of the gap size due to a metal build-up at the edges of the electrodes. Nanogaps with $\leq 2\,\mathrm{nm}$ size are achieved. Furthermore, a self-aligned gate electrode underneath the nanogap is fabricated in this way.
Electromigration (EM) is employed to break predefined constrictions of a continuous metallic wire. A feedback mechanism is applied to control the EM process and to prevent a thermal runway and therewith a melting of the nanowire during the EM process. The procedure makes it possible to reproducibly prepare tunnel junctions with gaps in the range of 1 nm.
Nanogap electrodes fabricated by the EM technique are used to study the charge transport through embedded Cor-OMe molecules. A resonant transport through the frontier molecular states of Cor-OMe is observed. The electrode separation derived in advance and the position of the HOMO and LUMO features give evidence that the current is mainly carried by a single molecule attached asymmetrically to the electrodes. Furthermore, the measured quantities agree well with the findings of the combined DFT and STS investigations performed for Cor-OMe on Au(111).

11 Conclusion

11.1 Summary

This thesis explored the self-assembly and the electronic properties of a unique conjugated molecular system, namely dodecakis(arylthio)coronenes (DATCs). It consists of a polycyclic aromatic core (coronene) with twelve peripheral arylthio substituents. In particular, combined STM and STS investigations were applied to characterize the structure of molecular monolayers on conducting substrates and the charge transport through the molecules. Spectroelectrochemisty studies of these compounds suggested that such molecular systems can be seen as nanomolecules with a three-dimensional electronic network, in which an effective delocalization of charges throughout the molecules exists. However, no investigations concerning the self-assembly and the electronic characteristics in the case of thin films or monolayers have beed carried out so far. The properties of conjugated materials on conducting substrates is of special importance for molecular electronic applications. Derivatives of DATC molecules are expected to be very suitable for such surface studies using STM and STS because, on the one hand, the charge stabilization effects of these compounds should allow to probe frontier molecular states within the typical energetic window accessible in STS measurements and, on the other hand, the large conjugated system makes them to interesting compounds for applications as novel organic semiconducting materials.
The molecular system is quite complex regarding its conformational degrees of freedom. The understanding of possible conformations and the resulting geometry was essential for the interpretation of the observed monolayer structures. In this context, DFT calculations were of enormous importance. The combination of topographical characterization and tunneling spectroscopy measurements additionally allowed to correlate electronic and structural properties of the monolayer films. Subsequent to a thorough analysis of the self-assembled structures formed by the basic molecular building block

dodecakis(phenylthio)coronene (Cor-H), the influence of additional functional groups on the self-assembly process and the charge transport properties was investigated. Finally, different fabrication routes for nanoscale electrode structures were examined. Besides the STM/STS technique, these electrode structures provided a further tool for charge transport investigations through single molecules.

Self-assembly of Cor-H

The self-assembly of Cor-H was studied in dependence of the used supporting substrate. On the graphite surface, the molecules did not aggregate into ordered supramolecular phases. Residual molecular motions prevented an imaging of the molecules with STM down to 80 K. Thus, only weak molecule-substrate and molecule-molecule interactions exist in the case of the Cor-H/graphite system. In contrast, Cor-H self-assembles on the Au(111) surface into a highly ordered columnar structure, in which the molecules have an *edge-on* orientation. The rows of this structure grow in a commensurable fashion along the $[11\bar{2}]$ direction of the gold surface. Thus, the STM studies showed that the occurrence of supramolecular self-assembly of Cor-H molecules has to be promoted by the substrate. The molecules themselves have no well-defined recognition properties, which are necessary for the formation of a distinct supramolecular order. The Au(111) substrate provides an opportune surface corrugation and mediates a directed molecular recognition into columns of densly stacked molecules.

Charge transport through Cor-H in dependence on molecular order

Tunneling spectroscopy measurements were performed for Cor-H monolayers on graphite and on Au(111). It was shown that the electronic properties of Cor-H molecules within the monolayer on graphite basically resemble the characteristics of single molecules. Weak interactions with the substrate and adjacent molecules, as already indicated by the STM topographical observations, lead to spectroscopic characteristics which can be ascribed to a resonant charge transport through mainly undisturbed frontier molecular states. The orbital mediated tunneling process was analyzed by empirical simulations of the STS measurements. Experimentally observed variations in the onset for resonant transport were properly described by considering changes of the specific position of Cor-H molecules within the tip-graphite junction, in line with the residual molecular

mobility on graphite.
The STS measurements in the case of the self-assembled columnar Cor-H structure on Au(111) revealed that the molecular stacking has a great impact on the electronic characteristics. The spectroscopy data showed that a band of electronic states has formed in the columnar structure. This was explained by the existence of substantial π-π interactions between adjacent molecules of the columns, leading to a splitting of the molecular energy levels. In this way, charge transport channels with a mainly one-dimensional electronic dispersion are built up.

Analysis of self-assembly and charge transport based on DFT calculations

The peripheral phenyl groups of Cor-H are forced to adopt a position above (*up* position) or below (*down* position) the plane of the core due to steric requirements and the sp^3 hybridization of the sulfur atoms. The possibility of different sequences and rotational angles for the substituents results in conformational degrees of freedom. Therefore, it was very important to figure out the stability of different Cor-H conformers. This was carried out on the basis of vdW-DFT simulations. It was found that the most stable conformation is an *up-down* alternation of the phenyl groups above and below the plane of the coronene unit. The conformation with all phenyl arms located on the same side with respect to the coronene plane (*up-up* conformer) is 0.67 eV less stable. Electronic structure calculations for the Cor-H conformers were compared to the tunneling spectroscopy measurements. The theoretically obtained energetic gap $\Delta E_{theo} = IP - EA$ of the *up-down* conformer is in very good agreement with the measured spectra of Cor-H molecules on graphite. Thus, the molecules are considered to be adsorbed on graphite without remarkable geometrical and electronic distortions compared to their stable gas phase conformation.
On the basis of the derived geometries of Cor-H conformers, the arrangement of the molecules within the self-assembled columnar *edge-on* structure on Au(111) could be examined in more detail. The combined STM and DFT results strongly suggested that the molecules maintain an *up-down* conformation within the columns. The stacking motif is observed to be very different to that of other discotic polycyclic aromatic hydrocarbons published in a couple of recent reports. Not the aromatic core is responsible for the intermolecular electronic overlap, but the peripheral phenyl groups of Cor-H. The DFT calculations revealed furthermore that the HOMO and the LUMO of isolated

Cor-H molecules are delocalized throughout the whole molecular system. Therefore, the π-π overlap interactions between the peripheral groups will enable charge delocalization throughout the columnar stacks. This supports the formation of band-like electronic states which were observed in STS measurements.

Substituent effects: Cor-OMe and Cor-CF3

The self-assembly of the basic building block Cor-H was observed to be strongly affected by modifying the outer aryl groups. Cor-OMe molecules, which possess additional OCH_3 groups in para-position at the peripheral phenyl groups, do not form columnar stacks, but adsorb on Au(111) in a *face-on* configuration and assemble into structures with a short range hexagonal order. The influence of the electron-donating ability and therewith the increased repulsive interactions between the aromatic π-systems of neighboring molecules is considered as the main origin for the observed totally different self-assembly properties of Cor-OMe and Cor-H. In addition, steric effects in the case of Cor-OMe might be another reason that a columnar stacking is unfavourable for theses molecules. The occupied and unoccupied orbitals of Cor-OMe molecules could be imaged with submolecular resolution with STM. Comparisons to DFT derived geometries of different Cor-OMe conformers and to simulated STM images indicated that the *up-down* conformer is also in this case the most stable one and that this conformation is maintained after adsorption on Au(111).
Subsequent charge states of the Cor-OMe molecules were resolved in STS measurements. The electron transport characteristics demonstrated that the methoxy groups adjacent to the substrate surface act as additional spacers and give rise to a thin insulating tunneling barrier between the substrate and the aromatic system of the molecules. The tunneling spectra could properly be explained with a double-barrier tunnel junction model and were furthermore strongly supported by DFT electronic structure calculations. The experimentally derived transport gap between tunneling via LUMO and HOMO states was shown to be consistent with the theoretical results for the stable *up-down* conformer, considering the specific potential profile within the junction and the charging contribution to the energies.
Cor-CF3 molecules, on the other hand, assemble again into a highly ordered columnar *edge-on* structure on Au(111). STS measurements showed that the dense stacking results in a modified electronic structure when compared to non-aggregated molecules.

Like for Cor-H, this is assigned to π-π interactions between adjacent molecules in the columnar stacks.
STM topographic features of adsorbed single molecules and tunneling spectroscopy data suggested that different conformers are possible after adsorption on the surface. This could be confirmed by DFT calculations which agreed well with the geometrical dimensions and the spectroscopic characteristics of the experimentally seen different conformers. The measurements indicated furthermore that the predominant part is adsorbed in *up-down* conformation. To a much less amount a *2up-d2own* conformation is observed.
Preliminary geometry optimizations for a Cor-CF3 dimer indicated that the stacking motif within the columnar structure is similar to that of Cor-H. However, additional C-F$\cdots\pi$ interactions might lead to an even greater stability of the columnar Cor-CF3 structure.
The observed substituent effects exemplified that a delicate balance of non-covalent interactions dictates the self-assembly process, which in turn can be used to create specific electronic properties. The structure formation and the electronic properties of DATCs can be tuned by substituents with tailored functionalities added to the basic molecular building block. Electronic functions ranging from semiconducting organic nanowires to molecular quantum dots can be realized in this way.

Nanometer-spaced metal electrodes for single molecule charge transport measurements

Contacting single molecules with nanoscale electrodes, fabricated by elaborate structuring techniques, is certainly closer to the application of molecular building blocks in working devices than the STM method. In this thesis, procedures have been worked out to provide nanometer-spaced metal electrodes, which are capable to "wire up" single molecules.
EBL was used as an appropriate tool to reproducibly fabricate electrodes with $\sim 10\,\text{nm}$ separation. The nanogap size could be decreased further, but with low yield.
Another approach consisted in first fabricating nanogaps with a quite large size ($\sim$ 20 nm) by EBL and subsequently reducing the gap dimensions by additional lithography and metalization steps. Suspended nanoelectrodes with $\leq 2\,\text{nm}$ separation were achieved in this way. Furthermore, this technique yields a self-aligned gate electrode

underneath the nanogap.
Finally, the electromigration process was employed to break predefined constrictions of a continuous metallic wire. A computer-controlled feedback scheme was applied and gap sizes in the range of 1 nm could be obtained.
First measurements showed that the fabricated electrode structures can be used for electron transport investigations through single molecules. This was proved by electrical characterizations after depositing Cor-OMe molecules between the nanogap electrodes. A resonant charge transport through the frontier molecular states of Cor-OMe could be measured. Strong indications were given that the current is carried mainly by a single molecule attached asymmetrically to the electrodes. Furthermore, the measured characteristics could be explained consistently with the findings of the combined DFT and STS investigations performed for Cor-OMe on Au(111).

11.2 Possible future directions

The investigations demonstrated that the self-assembly and the charge transport through DATC molecules can be varied specifically by using appropriate arylthio groups surrounding the conjugated core. Besides the studied derivatives, even more tailored substituents can be utilized in order to achieve a desired electronic function. The intermolecular electronic coupling and the directionality of the charge transport may be tuned further to create organic semiconductors with enhanced one-, two-, or three-dimensional charge delocalization. Interesting is furthermore the investigation of two-component systems. Sequences of stacks with electron-donors and electron-acceptors are interesting regarding applications as photovoltaic cells or light-emitting diodes. The other direction, as exemplified with Cor-OMe, lies in creating molecular quantum dots with addressable stable charge states. Specially designed modifications of the substituents should allow to achieve intact redox-activity of the molecules on metal surfaces. Memory elements or building blocks for logic circuits would be possible applications of these molecules.
Though applications will rely on the properties of the single molecules or the molecular layer at room temperature, investigations around liquid helium temperatures would be necessary to explore the fundamental self-assembly and charge transport processes in greater detail. For instance, it would be interesting to know if ordered self-assembled

structures of Cor-H are observable on graphite after sufficiently freezing out molecular motions. The tunneling through Cor-OMe on Au(111) at low temperatures could allow to observe stable ion formations and therewith multistabilities and memory effects. Furthermore, an improved imaging of the frontier orbitals of the adsorbed molecules would be possible.

The fabrication procedures for nanoscale electrode structures have been worked out thoroughly in this thesis, so that future works can focus on the integration of single molecules and the investigations of the charge transport through molecular junctions. Measurements in a controlled gas atmosphere and under different thermal conditions will give a deeper insight into the electronic properties of embedded molecules. For example, derivatives of Cor-OMe with longer insulating side groups could be used to tune the coupling to the electrodes and the usability for memory applications. Furthermore, gate dependent measurements will allow to study details of different charge states of the molecules like vibrational and electronic excitations.

Bibliography

[1] J. Bardeen, W. H. Brattain, The Transistor, A Semi-Conductor Triode. *Physical Review* **74**, 230–231 (1948).

[2] J. S. Kilby, Invention of the Integrated-Circuit. *IEEE Transactions On Electron Devices* **23**, 648–654 (1976).

[3] The International Technology Roadmap for Semiconductors, 2007 Edition. http://www.itrs.net/reports.html (2007).

[4] G. E. Moore, Cramming more components onto integrated circuits. *Electronics* **38** (1965).

[5] G. E. Moore, Progress in digital integrated electronics. *International Electron Devices Meeting* **21**, 11–13 (1975).

[6] S. E. Thompson, S. Parthasarathy, Moore's law: the future of Si microelectronics. *Materials Today* **9**, 20–25 (2006).

[7] A. Aviram, M. A. Ratner, Molecular Rectifiers. *Chemical Physics Letters* **29**, 277–283 (1974).

[8] G. Binnig, H. Rohrer, Scanning Tunneling Microscopy. *Helvetica Physica Acta* **55**, 726–735 (1982).

[9] G. Binnig, H. Rohrer, E. Weibel, 7x7 Reconstruction on Si(111) Resolved in Real Space. *Physical Review Letters* **50**, 120–123 (1983).

[10] L. A. Bumm, J. J. Arnold, M. T. Cygan, T. D. Dunbar, T. P. Burgin, L. Jones II, D. L. Allara, J. M. Tour, P. S. Weiss, Are Single Molecular Wires Conducting? *Science* **271**, 1705–1707 (1996).

[11] S. Datta, Weidong Tian, Seunghun Hong, R. Reifenberger, J. I. Henderson, C. P. Kubiak, Current-voltage characteristics of self-assembled monolayers by scanning tunneling microscopy. *Physical Review Letters* **79**, 2530–3 (1997).

[12] G. Leatherman, E. N. Durantini, D. Gust, T. A. Moore, A. L. Moore, S. Stone, Z. Zhou, P. Rez, Y. Z. Liu, S. M. Lindsay, Carotene as a molecular wire: Conducting atomic force microscopy. *Journal of Physical Chemistry B* **103**, 4006–4010 (1999).

[13] X. D. Cui, A. Primak, X. Zarate, J. Tomfohr, O. F. Sankey, A. L. Moore, T. A. Moore, D. Gust, G. Harris, S. M. Lindsay, Reproducible Measurement of Single-Molecule Conductivity. *Science* **294**, 571–574 (2001).

[14] C. Zhou, C. J. Muller, M. R. Deshpande, J. W. Sleight, M. A. Reed, Microfabrication of a Mechanically Controllable Break Junction in Silicon. *Applied Physics Letters* **67**, 1160–1162 (1995).

[15] M. A. Reed, C. Zhou, C. J. Muller, T. P. Burgin, J. M. Tour, Conductance of a Molecular Junction. *Science* **278**, 252–254 (1997).

[16] J. Reichert, R. Ochs, D. Beckmann, H. B. Weber, M. Mayor, H. v. Loehneysen, Driving Current through Single Organic Molecules. *Physical Review Letters* **88**, 176804 (2002).

[17] C. Zhou, M. R. Deshpande, M. A. Reed, L. Jones II, J. M. Tour, Nanoscale Metal/Self-Assembled Monolayer/Metal Heterostructures. *Applied Physics Letters* **71**, 611–613 (1997).

[18] A. F. Morpurgo, C. M. Marcus, D. B. Robinson, Controlled fabrication of metallic electrodes with atomic separation. *Applied Physics Letters* **74**, 2084–2086 (1999).

[19] C. Z. Li, H. X. He, N. J. Tao, Quantized tunneling current in the metallic nanogaps formed by electrodeposition and etching. *Applied Physics Letters* **77**, 3995–7 (2000).

[20] G. Mészáros, S. Kronholz, S. Karthäuser, D. Mayor, T. Wandlowski, Electrochemical fabrication and characterization of nanocontacts and nm-sized gaps. *Applied Physics A: Materials Science & Processing* **87**, 569–575 (2007).

[21] H. Park, A. K. L. Lim, A. P. Alivisatos, J. Park, P. L. McEuen, Fabrication of Metallic Electrodes with Nanometer Separation by Electromigration. *Applied Physics Letters* **75**, 301–303 (1999).

[22] D. R. Strachan, D. E. Smith, D. E. Johnston, T.-H. Park, J. Therien, D. A. Bonnell, A. T. Johnson, Controlled fabrication of nanogaps in ambient envieronment for molecular electronics. *Applied Physics Letters* **86**, 043109 (2005).

[23] G. Witte, C. Woll, Growth of aromatic molecules on solid substrates for applications in organic electronics. *Journal of Materials Research* **19**, 1889–1916 (2004).

[24] J. H. Burroughes, D. D. C. Bradley, A. R. Brown, R. N. Marks, K. Mackay, R. H. Friend, P. L. Burns, A. B. Holmes, Light-emitting-diodes based on conjugated polymers. *Nature* **347**, 539–541 (1990).

[25] J. R. Sheats, H. Antoniadis, M. Hueschen, W. Leonard, J. Miller, R. Moon, D. Roitman, A. Stocking, Organic electroluminescent devices. *Science* **273**, 884–888 (1996).

[26] N. S. Sariciftci, L. Smilowitz, A. J. Heeger, F. Wudl, Photoinduced Electron-Transfer from a conducting polymer to buckminsterfullerene. *Science* **258**, 1474–1476 (1992).

[27] C. J. Brabec, N. S. Sariciftci, J. C. Hummelen, Plastic solar cells. *Advanced Functional Materials* **11**, 15–26 (2001).

[28] G. Horowitz, Organic field-effect transistors. *Advanced Materials* **10**, 365–377 (1998).

[29] H. E. Katz, A. J. Lovinger, J. Johnson, C. Kloc, T. Siegrist, W. Li, Y. Y. Lin, A. Dodabalapur, A soluble and air-stable organic semiconductor with high electron mobility. *Nature* **404**, 478–481 (2000).

[30] J. L. Brédas, J. P. Calbert, D. A. da Silva, J. Cornil, Organic semiconductors: A theoretical characterization of the basic parameters governing charge transport. *Proceedings of the National Academy of Sciences of the United States of America* **99**, 5804–5809 (2002).

[31] C. D. Dimitrakopoulos, P. R. L. Malenfant, Organic thin film transistors for large area electronics. *Advanced Materials* **14**, 99–117 (2002).

[32] S. R. Forrest, The path to ubiquitous and low-cost organic electronic appliances on plastic. *Nature* **428**, 911–918 (2004).

[33] E. W. Meijer, A. P. H. J. Schenning, Chemistry - Material marriage in electronics. *Nature* **419**, 353–354 (2002).

[34] A. P. H. J. Schenning, E. W. Meijer, Supramolecular electronics; nanowires from self-assembled pi-conjugated systems. *Chemical Communications* 3245–3258 (2005).

[35] Y. Q. Xue, M. A. Ratner, Theoretical principles of single-molecule electronics: A chemical and mesoscopic view. *International Journal of Quantum Chemistry* **102**, 911–924 (2005).

[36] R. Waser, *Nanoelectronics and Information Technology – Advanced Electronic Materials and Novel Devices*. Second, Corrected Edition. WILEY-VCH Verlag GmbH & Co. KGaA, Weinheim, 2005.

[37] K. W. Hipps, *Handbook of Applied Solid State Spectroscopy*, Chapter Scanning Tunneling Spectroscopy, S. 305–350, Springer US (2006).

[38] J. G. Simmons, Generalized Formula for the Electric Tunnel Effect between Similar Electrodes Separated by a Thin Insulating Film. *Journal of Applied Physics* **34**, 1793–1803 (1963).

[39] J. G. Simmons, Low-Voltage Current-Voltage Relationship of Tunnel Junctions. *Journal of Applied Physics* **34**, 238–239 (1963).

[40] W. Wang, T. Lee, M. A. Reed, Mechanism of Electron Conduction in Self-Assembled Alkanethiol Monolayer Devices. *Physical Review B* **68**, 035416 (2003).

[41] W. Wang, T. Lee, M. A. Reed, *Nano and Molecular Electronics Handbook*, Chapter Electrical Characterization of Self-Assembled Monolayers, S. **1**–1–**1**–41, CRC Press, Boca Raton (2007).

[42] A. Vilan, Analyzing molecular current-voltage characteristics with the simmons tunneling model: Scaling and linearization. *Journal of Physical Chemistry C* **111**, 4431–4444 (2007).

[43] R. E. Holmlin, R. Haag, M. L. Chabinyc, R. F. Ismagilov, A. E. Cohen, A. Terfort, M. A. Rampi, G. M. Whitesides, Electron transport through thin organic films in metal-insulator-metal junctions based on self-assembled monolayers. *Journal of American Chemical Society* **123**, 5075–5085 (2001).

[44] X. D. Cui, X. Zarate, J. Tomfohr, O. F. Sankey, A. Primak, A. L. Moore, T. A. Moore, D. Gust, G. Harris, S. M. Lindsay, Making Electrical Contacts to Molecular Monolayers. *Nanotechnology* **13**, 5–14 (2002).

[45] H. B. Akkerman, B. de Boer, Electrical conduction through single molecules and self-assembled monolayers. *Journal of Physics: Condensed Matter* **20**, 013001 (2008).

[46] F. Zahid, M. Paulsson, S. Datta, *Advanced Semiconductor and Organic Nanotechniques, Part III – Physics and Technology of Molecular and Biotechnology Systems*, Chapter Electrical Conduction through Molecules, S. 1–41, Academic Press, London and San Diego (2003).

[47] S. Datta, *Quantum Transport: Atom to Transistor*. Cambridge University Press, Cambridge, 2005.

[48] L. P. Kouwenhoven, C. M. Markus, P. L. McEuen, S. Tarucha, R. M. Westervelt, N. S. Wingreen, *Mesoscopic Electron Transport*, Chapter Electron transport in quantum dots, S. 105–214, Plenum, New York and London (1997).

[49] L. P. Kouwenhoven, D. G. Austing, S. Tarucha, Few-electron quantum dots. *Reports on Progress in Physics* **64**, 701–736 (2001).

[50] J. Cornil, D. Beljonne, J. P. Calbert, J. L. Brédas, Interchain interactions in organic pi-conjugated materials: Impact on electronic structure, optical response, and charge transport. *Advanced Materials* **13**, 1053–1067 (2001).

[51] K. Kopitzki, *Einführung in die Festkörperphysik*. 3., durchges Auflage. Teubner, Stuttgart, 1993.

[52] Y. C. Cheng, R. J. Silbey, D. A. da Silva, J. P. Calbert, J. Cornil, J. L. Bredas, Three-dimensional band structure and bandlike mobility in oligoacene single crystals: A theoretical investigation. *Journal of Chemical Physics* **118**, 3764–3774 (2003).

[53] J. S. Huang, M. Kertesz, Intermolecular transfer integrals for organic molecular materials: can basis set convergence be achieved? *Chemical Physics Letters* **390**, 110–115 (2004).

[54] J. S. Huang, M. Kertesz, Validation of intermolecular transfer integral and bandwidth calculations for organic molecular materials. *Journal of Chemical Physics* **122**, 234707 (2005).

[55] N. Ueno, S. Kera, Electron spectroscopy of functional organic thin films: Deep insights into valence electronic structure in relation to charge transport property. *Progress in Surface Science* **83**, 490–557 (2008).

[56] V. Lemaur, D. A. Da Silva Filho, V. Coropceanu, M. Lehmann, Y. Geerts, J. Piris, M. G. Debije, A. M. Van de Craats, K. Senthilkumar, L. D. A. Siebbeles, J. M. Warman, J. L. Bredas, J. Cornil, Charge transport properties in discotic liquid crystals: A quantum-chemical insight into structure-property relationships. *Journal of American Chemical Society* **126**, 3271–3279 (2004).

[57] M. Pope, C. E. Swenberg, *Electronic Processes in Organic Crystals and Polymers*. 2nd edition. Oxford University Press, Oxford, 1999.

[58] G. M. Whitesides, J. P. Mathias, C. T. Seto, Molecular Self-Assembly and Nanochemistry: A Chemical Strategy for the Synthesis of Nanostructures. *Science* **254**, 1312–1319 (1991).

[59] A. Kühnle, Self-assembly of organic molecules at metal surfaces. *Current Opinion in Colloid & Interface Science* **14**, 157–168 (2009).

[60] J. V. Barth, Molecular Architectonic on Metal Surfaces. *Annual Review of Physical Chemistry* **58**, 375–407 (2007).

[61] H. Lüth, *Solid Surfaces, Interfaces and Thin Films*. Springer Verlag, Heidelberg, 2001.

[62] P. Maksymovych, D. C. Sorescu, J. T. Yates, Gold-adatom-mediated bonding in self-assembled short-chain alkanethiolate species on the Au(111) surface. *Physical Review Letters* **97**, 146103 (2006).

[63] D.B. Dougherty, P. Maksymovych, J.T. Yates Jr., Direct STM evidence for Cu-benzoate surface complexes on Cu(110). *Surface Science* **600**, 4484–4491 (2006).

[64] M.C. Lennartz, N. Atodiresei, L. Mueller-Meskamp, S. Karthaeuser, R. Waser, S. Bluegel, Cu-Adatom-Mediated Bonding in Close-Packed Benzoate/ Cu(110)-Systems. *Langmuir* **25**, 856–864 (2009).

[65] F. Schreiber, Structure and Growth of Self-Assembling Monolayers. *Progress in Surface Science* **65**, 151–256 (2000).

[66] R. Mazzarello, A. Cossaro, A. Verdini, R. Rousseau, L. Casalis, M. F. Danisman, L. Floreano, S. Scandolo, A. Morgante, G. Scoles, Structure of a CH3S monolayer on Au(111) solved by the interplay between molecular dynamics calculations and diffraction measurements. *Physical Review Letters* **98**, 16102/1– (2007).

[67] A. Cossaro, R. Mazzarello, R. Rousseau, L. Casalis, A. Verdini, A. Kohlmeyer, L. Floreano, S. Scandolo, A. Morgante, M. L. Klein, G. Scoles, X-ray diffraction and computation yield the structure of alkanethiols on gold(111). *Science* **321**, 943–946 (2008).

[68] D. E. Hooks, T. Fritz, M. D. Ward, Epitaxy and Molecular Organization on Solid Substrates. *Advanced Materials* **13**, 227–241 (2001).

[69] G. Binnig, H. Rohrer, Scanning tunneling microscopy - from birth to adolescence. *Review of Modern Physics* **59**, 615–625 (1987).

[70] J. Bardeen, Tunneling from a many-particle point of view. *Physical Review Letters* **6**, 57–59 (1961).

[71] J. Tersoff, D.R. Hamann, Theory and Application of the Scanning Tunneling Microscope. *Physical Review Letters* **50**, 1998–2001 (1983).

[72] J. Tersoff, D.R. Hamann, Theory of the Scanning Tunneling Microscope. *Physical Review B* **31**, 805–813 (1985).

[73] A. Selloni, P. Carnevali, E. Tosatti, C. D. Chen, Voltage-dependent scanning-tunneling microscopy of a crystal surface: Graphite. *Physical Review B* **31**, 2602–2605 (1985).

[74] N. D. Lang, Spectroscopy of single atoms in the scanning tunneling microscope. *Physical Review B* **34**, 5947–5950 (1986).

[75] J. A. Stroscio, R. M. Feenstra, A. P. Fein, Electronic Structure of the Si(111)2×1Surface by Scanning-Tunneling Microscopy. *Physical Review Letters* **57**, 2579–2582 (1986).

[76] R. M. Feenstra, J. A. Stroscio, A. P. Fein, Tunneling spectroscopy of the Si(111)2×1 surface. *Surface Science* **181**, 295–306 (1987).

[77] H. J. W. Zandvliet, A. van Houselt, Scanning Tunneling Spectroscopy. *Annual Review of Analytical Chemistry* **2**, 3.1–3.19 (2009).

[78] M. Toerker, T. Fritz, H. Proehl, Electronic transport through occupied and unoccupied states of an organic molecule on Au: Experiment and theory. *Physical Review B* **65**, 245422 (2002).

[79] P. G. Collins, J. C. Grossman, M. Côté, M. Ishigami, C. Piskoti, S. G. Louie, M. L. Cohen, A. Zettl, Scanning Tunneling Spectroscopy of C_{36}. *Physical Review Letters* **82**, 165–168 (1999).

[80] C. Wagner, R. Franke, T. Fritz, Evaluation of $I(V)$ curves in scanning tunneling spectroscopy of organic monolayers. *Physical Review B* **75**, 235432 (2007).

[81] M. C. Lennartz, *Selbstorganisation von Alkanthiolen und Carboxylaten auf Au(111)- and Cu(110)-Oberflächen.* Diploma thesis, RWTH Aachen, 2007.

[82] L. Müller-Meskamp, *Ferrocenes as Potential Building Blocks for Molecular Electronics – Self-Assembly and Tunneling Spectroscopy.* PhD Thesis, RWTH Aachen, 2007.

[83] L. Müller-Meskamp, *Charakterisierung von in einer SAM Hostmatrix immobilisierten funktionalen Moleckülen mittels Restersondenmethoden.* Diploma thesis, RWTH Aachen, 2004.

[84] M. Prietsch, A. Samsavar, R. Ludeke, Structural and electronic properties of the Bi/GaP(110) interface. *Physical Review B* **43**, 11850–11856 (1991).

[85] M. Gingras, J. M. Raimundo, Y. M. Chabre, Persulfurated aromatic compounds. *Angewandte Chemie - International Edition* **45**, 1686–1712 (2006).

[86] M. Gingras, A. Pinchart, C. Dallaire, T. Mallah, E. Levillain, Star-shaped nanomolecules based on p-phenylene sulfide asterisks with a persulfurated coronene core. *Chemistry - a European Journal* **10**, 2895–2904 (2004).

[87] J. H. R. Tucker, M. Gingras, H. Brand, J. M. Lehn, Redox properties of polythiaarene derivatives. A novel class of electron acceptors. *Journal of the Chemical Society - Perkin Transactions 2* 1303–1307 (1997).

[88] L. Pang, F. Brisse, E. A. C. Lucken, Order-disorder effects in clathrates. A crystallographic and Cl-35 NQR spectroscopic study of CCl(3)X guest molecules (X=Cl, Br, CH3, CN,NO2, H) in hexakis(phenylthio)benzene. *Canadian Journal of Chemistry* **73**, 351–361 (1995).

[89] P. Samori, M. Keil, R. Friedlein, J. Birgerson, M. Watson, M. Mullen, W. R. Salaneck, J. P. Rabe, Growth of ordered hexakis-dodecyl-hexabenzoeoronene layers from solution: A SFM and ARUPS study. *Journal of Physical Chemistry B* **105**, 11114–11119 (2001).

[90] B. A. Hermann, L. J. Scherer, C. E. Housecroft, E. C. Constable, Self-organized monolayers: A route to conformational switching and read-out of functional supramolecular assemblies by scanning probe methods. *Advanced Functional Materials* **16**, 221–235 (2006).

[91] E. Gomar-Nadal, J. Puigmarti-Luis, D. B. Amabilino, Assembly of functional molecular nanostructures on surfaces. *Chemical Society Reviews* **37**, 490–504 (2008).

[92] B. Lüssem, L. Müller-Meskamp, S. Karthäuser, R. Waser, A New Phase of the c(4x2) Superstructure of Alkanethiols Grown by Vapor Phase Deposition on Gold. *Langmuir* **21**, 5256–5258 (2005).

[93] L. Müller-Meskamp, B.Lüssem, S. Karthäuser, R. Waser, Rectangular $(3 \times 2\sqrt{3})$ Superlattice of a Dodecanethiol Self-Assembled Monolayer on Au(111) Observed by Ultra-High-Vacuum Scanning Tunneling Microscopy. *Journal of Physical Chemistry B* **109**, 11424–11426 (2005).

[94] B. Lüssem, L. Müller-Meskamp, S. Karthäuser, M. Homberger, U. Simon, R. Waser, Electrical and structural characterization of biphenylethanethiol SAMs. *Journal of Physical Chemistry C* **111**, 6392–7 (2007).

[95] L. Müller-Meskamp, S. Karthäuser, R. Waser, M. Homberger, U. Simon, Striped phase of mercaptoalkylferrocenes on Au(111) with a potential for nanoscale surface patterning. *Langmuir* **24**, 4577–4580 (2008).

[96] M.C. Lennartz, L. Müller-Meskamp, S. Karthäuser, R. Waser, Translational transitions at domain boundaries in octanethiol monolayers on Au(111). *Surface Science* **603**, 1156–1159 (2009).

[97] D. D. Dunlap, C. Bustamante, Images of single-stranded nucleic-acids by scanning tunneling micorscopy. *Nature* **342**, 204–206 (1989).

[98] P. Samori, J. P. Rabe, Scanning probe microscopy explorations on conjugated (macro)molecular architectures for molecular electronics. *Journal of Physics: Condensed Matter* **14**, 9955–9973 (2002).

[99] S. De Feyter, F. De Schryver, Two-Dimensional Dye Assemblies on Surfaces Studied by Scanning Tunneling Microscopy. *Topics in Current Chemistry* **258**, 205–255 (2005).

[100] H. P. Chang, A. J. Bard, Observation and characterization by scanning tunneling microscopy of structures generated by cleaving highly oriented pyrolytic graphite. *Langmuir* **7**, 1143–1153 (1991).

[101] W. T. Pong, C. Durkan, A review and outlook for an anomaly of scanning tunnelling microscopy (STM): Superlattices on graphite. *Journal of Physics D: Applied Physics* **38**, R329–R355 (2005).

[102] Y. Kobayashi, K. Takai, K. Fukui, T. Enoki, K. Harigaya, Y. Kaburagi, Y. Hishiyama, STM observation of electronic wave interference effect in finite-sized graphite with dislocation-network structures. *Physical Review B* **69**, 35418 (2004).

[103] S. K. Choudhary, A. K. Gupta, Spatially varying super-lattice structures and linear fringes on graphite surface. *Journal of Physics: Condensed Matter* **20**, 225008 (2008).

[104] J. Cervenka, C. F. J. Flipse, Structural and electronic properties of grain boundaries in graphite: Planes of periodically distributed point defects. *Physical Review B* **79**, 195429 (2009).

[105] C. Chidsey, D. Loiacono, T. Selator, S. Nakahara, STM Study of the Surface Morphology of Gold on Mica. *Surface Science* **200**, 45–66 (1988).

[106] U. Höpfner, H. Hehl, L. Brehmer, Preparation of Ordered Thin Gold Films. *Applied Surface Science* **152**, 259 (1999).

[107] B. Lüssem, *Molecular Electronic Building Blocks Based on Self-Assembled Monolayers*. PhD Thesis, RWTH Aachen, 2006.

[108] B. Luessem, S. Karthaeuser, H. Haselier, R. Waser, The origin of faceting of ultraflat gold films epitaxially grown on mica. *Applied Surface Science* **249**, 197–202 (2005).

[109] J. V. Barth, H. Brune, G. Ertl, R. J. Behm, Scanning Tunneling Microscopy Observations on the Reconstructed Au(111) Surface: Atomic Structure, Long-Range Superstructure, Rotational Domains, and Surface Defects. *Physical Review B* **42**, 9307–9318 (1990).

[110] R. J. Needs, M. J. Godfrey, M. Mansfield, Theory of Surface Stress and Surface Reconstruction. *Surface Science* **242**, 215–221 (1991).

[111] F. Besenbacher, Scanning tunnelling microscopy studies of metal surfaces. *Reports on Progress in Physics* **59**, 1737–1802 (1996).

[112] D. D. Chambliss, R. J. Wilson, S. Chiang, Nucleation of ordered Ni island arrays on Au(111) by surface-lattice dislocations. *Physical Review Letters* **66**, 1721 (1991).

[113] D. Fujita, T. Yakabe, H. Nejoh, T. Sato, M. Iwatsuki, Scanning tunneling microscopy study on the initial adsorption behavior of C_{60} molecules on a reconstructed Au(111)-$(23 \times \sqrt{3})$ surface at various temperatures. *Surface Science* **366**, 93 (1996).

[114] M. Böhringer, K. Morgenstern, W. D. Schneider, R. Berndt, F. Mauri, A. De Vita, R. Car, Two-dimensional self-assembly of supramolecular clusters and chains. *Physical Review Letters* **83**, 324 (1999).

[115] T. Yokoyama, S. Yokoyama, T. Kamikado, Y. Okuno, S. Mashiko, Selective assembly on a surface of supramolecular aggregates with controlled size and shape. *Nature* **413**, 619 (2001).

[116] A. Kirakosian, M. J. Comstock, J. W. Cho, M. F. Crommie, Molecular commensurability with a surface reconstruction:STM study of azobenzene on Au(111). *Physical Review B* **71**, 113409 (2005).

[117] S. D. Kevan, R. H. Gaylord, High-resoluton photoemission-study of the electronic-structure of the noble-metal (111) surfaces. *Physical Review B* **36**, 5809–5818 (1987).

[118] M. P. Everson, L. C. Davis, R. C. Jaklevic, W. Shen, Effects of surface states features upon the Au(111) surface state local density of states studied with scanning tunneling spectroscopy. *Journal of Vacuum Science & Technology B* **9**, 891–896 (1991).

[119] F. Reinert, G. Nicolay, S. Schmidt, D. Ehm, S. Hufner, Direct measurements of the L-gap surface states on the (111) face of noble metals by photoelectron spectroscopy. *Physical Review B* **63**, 115415 (2001).

[120] A. K. Dutta, Electrical Conductivity of Single Crystals of Graphite. *Physical Review* **90**, 187–192 (1953).

[121] M. Ohler, J. Baruchel, A. W. Moore, P. Galez, A. Freund, Direct observation of mosaic blocks in highly oriented pyrolytic graphite. *Nuclear Instruments and Methods in Physics Research Section B* **129**, 257–260 (1997).

[122] J. P. Rabe, S. Buchholz, Commensurability and Mobility in Two-Dimensional Molecular Patterns on Graphite. *Science* **253**, 424–427 (1991).

[123] K. Müllen, J. P. Rabe, Nanographenes as active components of single-molecule electronics and how a scanning tunneling microscope puts them to work. *Accounts of Chemical Research* **41**, 511–520 (2008).

[124] B. Feuerbacher, B. Fitton, Splitting of the π Bands in Graphite. *Physical Review Letters* **26**, 840 (1971).

[125] R. F. Willis, B. Feuerbacher, B. Fitton, Experimental investigation of the band structure of graphite. *Physical Review B* **4**, 2441 (1971).

[126] Z. Klusek, Investigations of splitting of the π bands in graphite by scanning tunneling spectroscopy. *Applied Surface Science* **151**, 251–261 (1999).

[127] M. Kuwabara, D. R. Ciarke, D. A. Smith, Anomalous superperiodicity in scanning tunneling microscope images of graphite. *Applied Physics Letters* **56**, 2396 (1990).

[128] V. J. Cee, D. L. Patrick, T. P. Beebe Jr., Unusual aspects of superperiodic features on highly oriented pyrolytic graphite. *Surface Science* **329**, 141–148 (1995).

[129] J. Xhie, K. Sattler, M. Ge, N. Venkateswaran, Giant and supergiant lattices on graphite. *Physical Review B* **47**, 15835–15841 (1993).

[130] H. Beyer, M. Müller, Th. Schimmel, Monolayers of graphite rotated by a defined angle: hexagonal superlstructures by STM. *Applied Physics A* **68**, 163–166 (1999).

[131] H.-L. Sun, Q.-T. Shen, J.-F. Jia, Q.-Z. Zhang, Q.-K. Xue, Scanning tunneling microscopy study of superlattice domain boundaries on graphite surface. *Surface Science* **542**, 94–100 (2003).

[132] J. M. Campanera, G. Savini, I. Suarez-Martinez, M. I. Heggie, Density functional calculations on the intricacies of Moiré patterns on graphite. *Physical Review B* **75**, 235449 (2007).

[133] G. M. Florio, T. L. Werblowsky, T. Müller, B. J. Berne, G. W. Flynn, Self-assembly of small polycyclic aromatic hydrocarbons on graphite: A combined scanning tunneling microscopy and theoretical approach. *Journal of Physical Chemistry B* **109**, 4520–4532 (2005).

[134] K. Walzer, M. Sternberg, M. Hietschold, Formation and characterization of coronene monolayers on HOPG(0001) and MoS_2(0001): a combined STM/STS and tight-binding study. *Surface Science* **415**, 376–384 (1998).

[135] M. Lackinger, S. Griessl, W. M. Heckl, M. Hietschold, STM and STS of coronene on HOPG(0001) in UHV – adsorption of the smallest possible graphite flakes on graphite. *Analytical and Bioanalytical Chemistry* **374**, 685–687 (2002).

[136] T. Schmitz-Hübsch, F. Sellam, R. Staub, M. Törker, T. Fritz, Ch. Kübel, K. Müllen, K. Leo, Direct observation of organic-organic heteroepitaxy: perylene-tetracarboxylic-dianhydride on hexa-peri-benzocoronene on highly ordered pyrolytic graphite. *Surface Science* **445**, 358–367 (2000).

[137] P. Samori, N. Severin, C. D. Simpson, K. Müllen, J. P. Rabe, Epitaxial Composite Layers of Electron Donors and Acceptors from Very Large Polycyclic Aromatic Hydrocarbons. *Journal of the American Chemical Society* **124**, 9454–9457 (2002).

[138] E. B. Throughton, C. D. Bain, G. M. Whitesides, R. G. Nuzzo, D. L. Allara, M. D. Porter, Monolayer films prepared by the spontaneous self-assembly of symmetrical and unsymmetrical dialkyl sulfides from solution onto gold substrates. *Langmuir* **4**, 365–385 (1988).

[139] H. Schönherr, F. J. B. Kremer, S. Kumar, J. A. Rego, H. Wolf, H. Ringsdorf, M. Jaschke, H. J. Butt, E. Bamberg, Self-assembled monolayers of discotic liquid crystalline thioethers, discoid disulfides, and thiols on gold: Molecular engineering of ordered surfaces. *Journal of the American Chemical Society* **118**, 13051–13057 (1996).

[140] T. Ishida, N. Choi, W. Mizutani, H. Tokumoto, I. Kojima, H. Azehara, H. Hokari, U. Akiba, M. Fujihira, High-resolution X-ray photoelectron spectra of organosulfur monolayers on Au(111): S(2p) spectral dependence on molecular species. *Langmuir* **15**, 6799–806 (1999).

[141] S. C. Jensen, A. E. Baber, H. L. Tierney, E. C. H. Sykes, Adsorption, interaction, and manipulation of dibutyl sulfide on Cu111. *ACS Nano* **1**, 22–29 (2007).

[142] O. Krichevsky, G. Bonnet, Fluorescence correlation spectroscopy: the technique and its applications. *Reports on Progress in Physics* **65**, 251–297 (2002).

[143] S. Rathgeber, H. J. Beauvisage, H. Chevreau, N. Willenbacher, C. Oelschlaeger, Microrheology with Fluorescence Correlation Spectroscopy. *Langmuir* **25**, 6368–6376 (2009).

[144] M. Knupfer, J. Fink, E. Zojer, G. Leising, D. Fichou, Universal exciton size scaling in π conjugated systems. *Chemical Physics Letters* **318**, 585–589 (2000).

[145] H. Proehl, M. Toerker, F. Sellam, T. Fritz, K. Leo, C. Simpson, K. Müllen, Comparison of ultraviolet photoelectron spectroscopy and scanning tunneling spectroscopymeasurements on highly ordered ultrathin films of hexa-perihexabenzocoronene on Au(111). *Physical Review B* **63**, 205409 (2001).

[146] D. Cahen, A. Kahn, E. Umbach, Energetics of molecular interfaces. *Materials Today* **8**, 32–41 (2005).

[147] R. O. Loutfy, C. K. Hsiao, B. S. Ong, B. Keoshkerian, Electrochemical evaluation of electron acceptor materials. *Canadian Journal of Chemistry* **62**, 1877–1885 (1984).

[148] W. H. Han, E. N. Durantini, T. A. Moore, A. L. Moore, D. Gust, P. Rez, G. Leatherman, G. R. Seely, N. J. Tao, S. M. Lindsay, STM contrast, electron-transfer chemistry, and conduction in molecules. *Journal of Physical Chemistry B* **101**, 10719–10725 (1997).

[149] X. W. Tu, G. Mikaelian, W. Ho, Controlling single-molecule negative differential resistance in a double-barrier tunnel junction. *Physical Review Letters* **100**, 126807 (2008).

[150] W. L. Deng, K. W. Hipps, Tip-sample distance dependence in the STM-based orbital-mediated tunneling spectrum of nickel(II) tetraphenylporphyrin deposited on Au(111). *Journal of Physical Chemistry B* **107**, 10736–10740 (2003).

[151] J. Cornil, V. Lemaur, J.-P. Calbert, J.-L. Brédas, Charge Transport in Discotic Liquid Crystals: A Molecular Scale Description. *Advanced Materials* **14**, 726–729 (2002).

[152] X. Feng, V. Marcon, W. Pisula, M.R. Hansen, J. Kirkpatrick, F. Grozema, D. Andrienko, K. Kremer, K. Müllen, Towards high charge-carrier mobilities by rational design of the shape and periphery of discotics. *Nature Materials* **8**, 421–426 (2009).

[153] D. Adam, P. Schuhmacher, J. Simmerer, L. Häussling, K. Siemensmeyer, K. H. Etzbach, H. Ringsdorf, D. Haarer, Fast photoconduction in the highly ordered columnar phase of a discotic liquid crystal. *Nature* **371**, 141–143 (1994).

[154] A. Fechtenkötter, K. Saalwächter, M. A. Harbison, K. Müllen, H. W. Spiess, Highly Ordered Columnar Structures from Hexa-peri-hexabenzocoronenes - Synthesis, X-ray Diffraction, and Solid-State Heteronuclear Multiple-Quantum NMR Investigations. *Angewandte Chemie - International Edition* **38**, 3039–3042 (1999).

[155] I. D. Mackie, G. A. DiLabio, Interactions in Large, Polyaromatic Hydrocarbon Dimers: Application of Density Functional Theory with Dispersion Corrections. *Journal of Physical Chemistry A* **112**, 10968–10976 (2008).

[156] Y. Zhao, D. G. Truhlar, A prototype for graphene material simulation: Structures and interaction potentials of coronene dimers. *Journal of Physical Chemistry C* **112**, 4061–4067 (2008).

[157] D. Käfer, A. Bashir, X. Dou, G. Witte, K. Müllen, C. Wöll, Evidence for Band-Like Transport in Graphene-Based Organic Monolayers. *Advanced Materials* **21**, 1–5 (2009).

[158] R. Temirov, S. Soubatch, A. Luican, F. S. Tautz, Free-electron-like dispersion in an organic monolayer film on a metal substrate. *Nature* **444**, 350–353 (2006).

[159] N. Gonzalez-Lakunza, I. Fernandez-Torrente, K. J. Franke, N. Lorente, A. Arnau, J. I. Pascual, Formation of dispersive hybrid bands at an organic-metal interface. *Physical Review Letters* **100**, 156805 (2008).

[160] R. Zacharia, H. Ulbricht, T. Hertel, Interlayer cohesive energy of graphite from thermal desorption of polyaromatic hydrocarbons. *Physical Review B* **69**, 155406 (2004).

[161] A. G. Donchev, *Ab initio* quantum force field for simulations of nanostructures. *Physical Review B* **74**, 235401 (2006).

[162] S. D. Chakarova-Käck, E. Schröder, B. I. Lundqvist, D. C. Langreth, Application of van der Waals Density Functional to an Extended System: Adsorption of Benzene and Naphthalene on Graphite. *Physical Review Letters* **96**, 146107 (2006).

[163] D. C. Langreth, B. I. Lundqvist, S. D. Chakarova-Käck, V. R. Cooper, M. Dion, P. Hyldgaard, A. Kelkkanen, J. Kleis, L. Kong, S. Li, P. G. Moses, E. Murray, A. Puzder, H. Rydberg, E. Schröder, T. Thonhauser, A density functional for sparse matter. *Journal of Physics: Condensed Matter* **21**, 084203 (2009).

[164] M. O. Sinnokrot, E. F. Valeev, C. D. Sherrill, Estimates of the Ab Initio Limit for $\pi - \pi$ Interactions: The Benzene Dimer. *Journal of the American Chemical Society* **124**, 10887–10893 (2002).

[165] H. L. Tierney, A. E. Baber, E. C. H. Sykes, A. Akimov, A. B. Kolomeisky, Dynamics of Thioether Molecular Rotors: Effects of Surface Interactions and Chain Flexibility. *Journal of Physical Chemistry C* **113**, 10913–10920 (2009).

[166] S. Sergeyev, W. Pisula, Y. H. Geerts, Discotic liquid crystals: a new generation of organic semiconductors. *Chemical Society Reviews* **36**, 1902–1929 (2007).

[167] E. J. Foster, R. B. Jones, C. Lavigueur, V. E. Williams, Structural Factors Controlling the Self-Assembly of Columnar Liquid Crystals. *Journal of the American Chemical Society* **128**, 8569–8574 (2006).

[168] F. Cozzi, M. Cinquini, R. Annunziata, T. Dwyer, J. S. Siegel, Polar/π Interactions between Stacked Aryls in 1,8-Diarylnaphthalenes. *Journal of the American Chemical Society* **114**, 5729–5733 (1992).

[169] F. Cozzi, M. Cinquini, R. Annunziata, J. S. Siegel, Dominance of Polar/π over Charge-Transfer Effects in Stacked Phenyl Interactions. *Journal of the American Chemical Society* **115**, 5330–5331 (1993).

[170] F. Emmerling, I. Orgzall, B. Dietzel, B. W. Schulz, G. Reck, B. Schulz, Structural studies on trifluoromethyl substituted 2,5-diphenyl-1,3,4-oxadiazoles. *Journal of Molecular Structure* **832**, 124–131 (2007).

[171] S. Kronholz, *Integration von Nanostrukturen durch alternative Methoden: Mizellen-Deposition, Template-Wachstum und Nanogaps*. PhD Thesis, RWTH Aachen, 2007.

[172] A. Bezryadin, C. Dekker, G. Schmid, Electrostatic trapping of single conducting nanoparticles between nanoelectrodes. *Applied Physics Letters* **71**, 1273–1275 (1997).

[173] P. Steinmann, J. M. R. Weaver, Fabrication of sub-5 nm gaps between metallic electrodes using conventional lithographic techniques. *Journal of Vacuum Science & Technology B* **22**, 3178–3181 (2004).

[174] H. Park, J. Park, A. K. L. Lim, E. H. Anderson, A. P. Alivisatos, P. L. McEuen, Nanomechanical Oscillations in a Single-C-60 Transistor. *Nature* **407**, 57–60 (2000).

[175] J. R. Black, Electromigration failure modes in aluminium metallitation for semiconductor devices. *Proceedings of the IEEE* **57**, 1587 (1969).

[176] J. R. Black, Electromigration - A brief survey and some results. *IEEE Transactions On Electron Devices* **ED16**, 338 (1969).

[177] D. Young, A. Christou, Failure-mechanism models for electromigration. *IEEE Transactions On Reliability* **43**, 186–192 (1994).

[178] C. Durkan, M. E. Welland, Analysis of failure mechanisms in electrically stressed gold nanowires. *Ultramicroscopy* **82**, 125–133 (2000).

[179] M. L. Trouwborst, S. J. van der Molen, B. J. van Wees, The Role of Joule Heating in the Formation of Nanogaps by Electromigration. *Journal of Applied Physics* **99**, 114316 (2006).

[180] G. Esen, M. S. Fuhrer, Temperature control of electromigration to form gold nanogap junctions. *Applied Physics Letters* **87**, 263101 (2005).

[181] J. Park, A. N. Pasupathy, J. I. Goldsmith, C. Chang, Y. Yaish, J. R. Petta, M. Rinkoski, J. P. Sethna, H. D. Abruna, P. L. McEuen, D. C. Ralph, Coulomb blockade and the Kondo effect in single-atom transistors. *Nature* **417**, 722–725 (2002).

[182] Y. Selzer, M. A. Cabassi, T. S. Mayer, D. L. Allara, Temperature effects on conduction through a molecular junction. *Nanotechnology* **15**, S483–S488 (2004).

[183] L. H. Yu, D. Natelson, The Kondo Effect in C60 Single-Molecule Transistors. *Nano Letters* **4**, 79–83 (2004).

[184] A. A. Houck, J. Labaziewicz, E. K. Chan, J. A. Folk, I. L. Chuang, Kondo Effect in Electromigrated Gold Break Junctions. *Nano Letters* **5**, 1685–1688 (2005).

[185] R. Sordan, K. Balasubramanian, M. Burghard, K. Kern, Coulomb blockade phenomena in electromigration break junctions. *Applied Physics Letters* **87**, 13106 (2005).

[186] M. Poot, E. Osorio, K. O'Neill, J. M. Thijssen, D. Vanmaekelbergh, C. A. van Walree, L. W. Jenneskens, H. S. J. van der Zant, Temperature dependence of three-terminal molecular junctions with sulfur end-functionalized tercyclohexylidenes. *Nano Letters* **6**, 1031–1035 (2006).

[187] H. S. J. van der Zant, E. A. Osorio, M. Poot, K. O'Neill, Electromigrated molecular junctions. *Physica Status Solidi B - Basic Solid State Physics* **243**, 3408–3412 (2006).

1. **Ferrocenes as Potential Building Blocks for Molecular Electronics**
   Self-Assembly and Tunneling Spectroscopy
   by L. Müller-Meskamp (2008), 153 pages
   ISBN: 978-3-89336-509-8

2. **Magnetic Proximity Effects in Highly-ordered Transition Metal Oxide Heterosystems studied by Soft x-Ray Photoemission Electron Microscopy**
   by I. P. Krug (2008), XX, 180 pages
   ISBN: 978-3-89336-521-0

3. **Seltenerd-basierte ternäre Oxide als alternative Gatedielektrika**
   von J. M. Roeckerath (2008), 148 Seiten
   ISBN: 978-3-89336-543-2

4. **Strominduzierte Magnetisierungsdynamik in einkristallinen Nanosäulen**
   von R. Lehndorff (2009), I, 86 Seiten
   ISBN: 978-3-89336-564-7

5. **Magnetization Dynamics in Magnetically Coupled Heterostructures**
   von A. Kaiser (2009), X, 121 pages
   ISBN: 978-3-89336-577-7

6. **Resistive switching in Pt/TiO_2/PT**
   by D. S. Jeong (2009), vii, 133 pages
   ISBN: 978-3-89336-579-1

7. **Electromechanical Force Microscopy and Tip-Enhanced Raman Spectroscopy for Polar Oxide Nanoparticles**
   by S. Röhrig (2009), vi, 114 pages
   ISBN: 978-3-89336-600-2

8. **Investigation of resistive switching in barium strontium titanate thin films for memory applications**
   by W. Shen (2010), 114 pages
   ISBN: 978-3-89336-608-8

9. **Nanostrukturierte Metallelektroden zur funktionalen Kopplung an neuronale Zellen**
   von D. Brüggemann (2010), vii, 160 Seiten
   ISBN: 978-3-89336-627-9

10. **Integration of resistive switching devices in crossbar structures**
    by Chr. Nauenheim (2010), XII, 142 pages
    ISBN: 978-3-89336-636-1

11. **Correlation between Raman spectroscopy and electron microscopy on individual carbon nanotubes and peapods**
by C. Spudat (2010). xiv, 125 pages
ISBN: 978-3-89336-648-4

12. **DC and RF Characterization of NiSi Schottky Barrier MOSFETs with Dopant Segregation**
by C. J. Urban (2010), iv, 151 pages
ISBN: 978-3-89336-644-6

13. **Alternative Systems for Molecular Electronics: Functionalized Carboxylic Acids on Structured Surfaces**
by M. C. Lennartz (2010), 183 pages
ISBN: 978-3-89336-667-5

14. **Highly conductive electrodes as diffusion barrier for high temperature applications**
by B. Mešić (2010), VII, 138 pages
ISBN: 978-3-89336-670-5

15. **Modeling, Fabrication and Characterization of Silicon Tunnel Field-Effect Transistors**
by C. P. Sandow (2010), XIII, 112 pages
ISBN: 978-3-89336-675-0

16. **Substituted Coronenes for Molecular Electronics: From Supramolecular Structures to Single Molecules**
by P. Kowalzik (2010), ix, 149 pages
ISBN: 978-3-89336-679-8

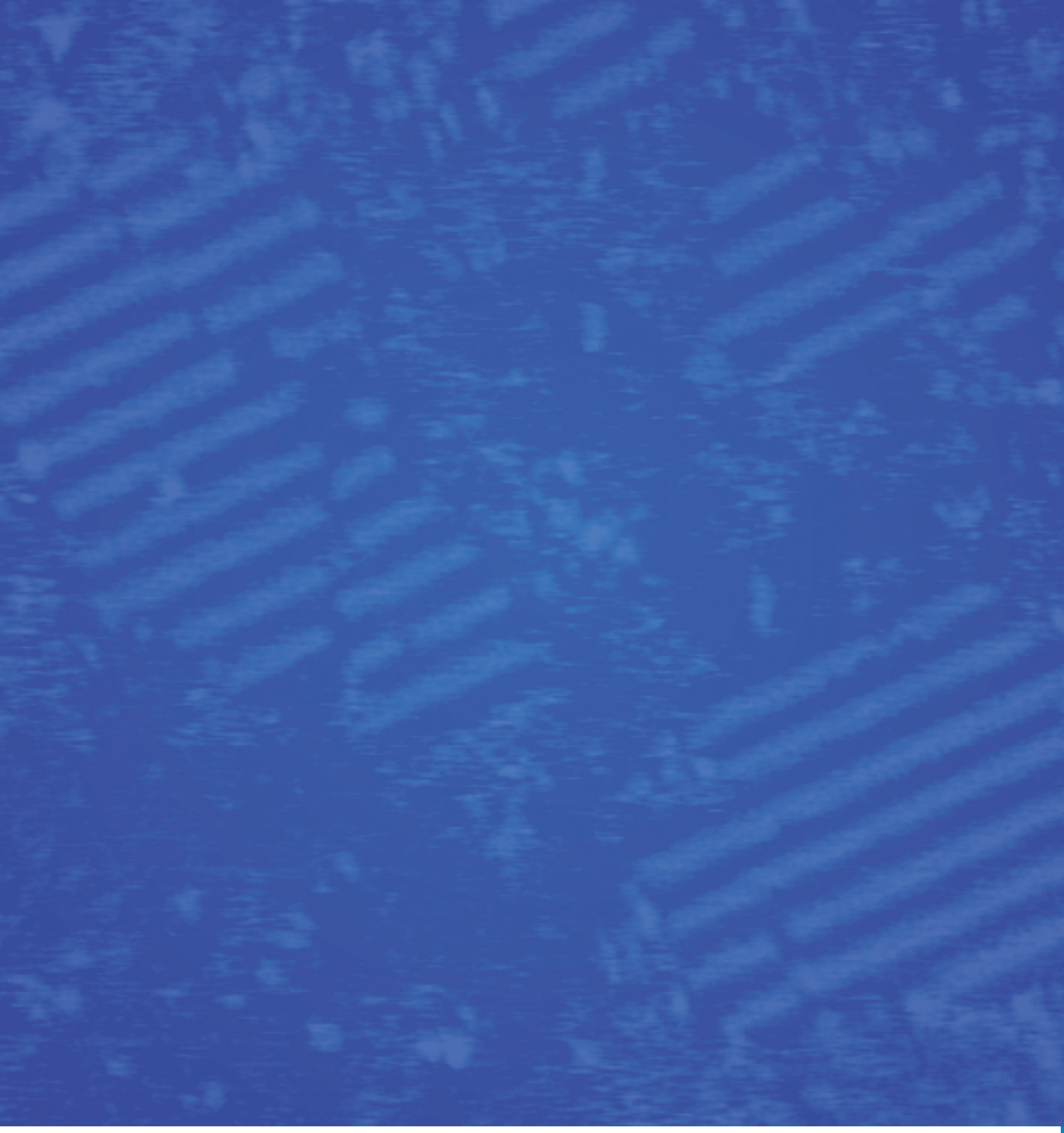

Information / Information
Band / Volume 16
ISBN 978-3-89336-679-8

JÜLICH
FORSCHUNGSZENTRUM